Nanometer-Precision Electron-Beam Lithography with Applications in Integrated Optics

by

Jeffrey Todd Hastings

B.S. Physics, Centre College (1996)
M.S. Electrical Engineering, Purdue University (1998)

Submitted to the Department of Electrical Engineering and Computer Science
in partial fulfillment of the requirements for the degree of

Doctor of Philosophy

at the

MASSACHUSETTS INSTITUTE OF TECHNOLOGY

June 2003

© Massachusetts Institute of Technology 2003. All rights reserved.

Author ....
Department of Electrical Engineering and Computer Science
May 2, 2003

Certified by ....
Henry I. Smith
Joseph F. and Nancy P. Keithley Professor of Electrical Engineering
Thesis Supervisor

Accepted by ....
Arthur C. Smith
Chairman, Department Committee on Graduate Students

ARCHIVES

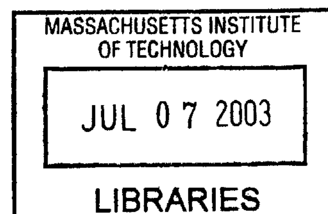

Nanometer-Precision Electron-Beam Lithography with Applications in Integrated Optics

by

Jeffrey Todd Hastings

Submitted to the Department of Electrical Engineering and Computer Science
on May 2, 2003, in partial fulfillment of the
requirements for the degree of
Doctor of Philosophy

Abstract

Scanning electron-beam lithography (SEBL) provides sub-10-nm resolution and arbitrary-pattern generation; however, SEBL's pattern-placement accuracy remains inadequate for future integrated-circuits and integrated-optical devices. Environmental disturbances, system imperfections, charging, and a variety of other factors contribute to pattern-placement inaccuracy. To overcome these limitations, spatial-phase locked electron-beam lithography (SPLEBL) monitors the beam location with respect to a reference grid on the substrate. Phase detection of the periodic grid signal provides feedback control of the beam position to within a fraction of the period. Using this technique we exposed patterns globally locked to a fiducial grid and reduced local field-stitching errors to $\sigma \leq 1.3$ nm.

Spatial-phase locking is particularly important for integrated-optical devices that require pattern-placement accuracy within a fraction of the wavelength of light. As an example, Bragg-grating based optical filters were fabricated in silicon-on-insulator waveguides using SPLEBL. The filters were designed to reflect a narrow-range of wavelengths within the communications band near 1550-nm. We patterned the devices in a single lithography step by placing the gratings in the waveguide sidewalls. This design allows apodization of the filter response by lithographically varying the grating depth. Measured transmission spectra show greatly reduced sidelobe levels for apodized devices compared to devices with uniform gratings.

Thesis Supervisor: Henry I. Smith
Title: Joseph F. and Nancy P. Keithley Professor of Electrical Engineering

Acknowledgments

This thesis would not have been possible without the creative ideas, endless enthusiasm, and excellent guidance of Professor Henry Smith. Professor Smith's direction proved invaluable with regard to technical matters, research approaches, career considerations, and the presentation of our work. Professor Smith always helped me focus on the problem at hand while providing freedom to find creative solutions and pursue interesting ideas. I am also grateful to that he introduced me to the wonders of the Canadian arctic.

A number of people further enhanced my experience at MIT. I thank Professor Erich Ippen and Professor Leslie Kolodziejski for serving on my thesis committee and for their interesting questions and helpful comments about my work. I greatly appreciate the time and effort of Professor Dennis Freeman and Professor Terry Orlando in serving on other examination committees. Professor Orlando also provided continuing encouragement and advice far beyond his initial role in introducing me to the department. Professor Martin Schmidt served as an excellent academic advisor throughout my time at MIT. His direction concerning course selection, the doctoral-degree requirements, and career options paved a smooth path through MIT's graduate program.

Working with the members of MIT's NanoStructures laboratory has been a great pleasure. A number of talented people have helped develop spatial-phase locked electron-beam lithography, including Professor Smith, Dr. Mark Schattenburg, and Dr. Erik Anderson who provided the original idea. In addition, Dr. Schattenburg and the members of the Space NanoTechnology Laboratory have been instrumental in developing the accurate gratings and grids used in this work. Dr. Juan Ferrera, in collaboration with the members of IBM's electron-beam lithography group, conducted many of the early experiments with spatial-phase locking and provided invaluable instruction when I was beginning work on the project. I have worked closely with Dr. James Goodberlet, Feng Zhang, and Mark Finlayson over the course of my graduate study, and their work was essential to this thesis. I am excited to see Sander Smits and Cynthia Caramana tackling the many remaining challenges in spatial-phase locked EBL, and I wish them the best of luck.

Members of the NanoStructures Laboratory focusing on integrated-optical devices also contributed to the research described here. Dr. Thomas Murphy taught me many of the concepts of integrated optics, and introduced me to silicon-on-insulator as a potential materials system. His efforts in modeling and testing planar waveguides helped me to rapidly address these issues in my own research. Dr. Michael Lim helped extensively by teaching me the intricacies of x-ray lithography and reactive-ion etching, and Dr. Jalal Khan provided many insights concerning the theory, design, and analysis of integrated-waveguide devices. Tymon Barwicz, who is continuing integrated-optics research in the NSL, has also been the source of many fruitful discussions. Finally, I would like to thank Dr. Takao Yonehara at Canon for graciously providing the silicon-on-insulator substrates used here.

It has been a pleasure to work side-by-side with my office mates Dario Gil and

Michael Walsh. Our discussions, whether scientific or otherwise, have always been enjoyable and their ideas have certainly found their way into this research. I would also like to thank Mark Mondol for his commitment to the members of the Nano-Structures Laboratory, a commitment that frequently stretches beyond the confines of MIT. James Carter and James Daley repeatedly went beyond the call of duty when helping with technical aspects of this research. Cindy Lewis also deserves thanks for managing the administrative details of the laboratory.

I would like to thank the National Science Foundation for supporting my early graduate studies and the Defense Advanced Research Projects Agency for supporting our research in spatial-phase locked e-beam lithography. Beyond the laboratory, my friendships formed within MIT's Graduate Christian Fellowship have made my time at MIT particularly enjoyable and meaningful. Jessica Coleman has lovingly shared every frustration and celebration throughout my graduate work, and I am forever grateful for her confidence, patience, and support. Finally, I would like to thank my parents, Curtis and Sarah Hastings, for their unconditional support at every stage of my education and their invaluable contributions to every aspect of my life.

Contents

1 Introduction **13**

1.1 Electron Beam Lithography Overview 16

1.1.1 EBL System Components 17

1.1.2 Exposure Strategies 20

1.2 Pattern Placement in SEBL 22

1.3 Spatial-Phase-Locked Electron-Beam Lithography 26

1.4 Bragg-grating optical filters via SPLEBL 27

2 The Fiducial Grid **31**

2.1 Patterning the Grid 33

2.1.1 The Master Grid 33

2.1.2 Replicating the Grid 36

2.2 Backscattered Electron Grids 37

2.2.1 The Backscattered Electron Signal 38

2.2.2 Implemented Backscattered Electron Grids 39

2.3 Secondary Electron Grids 40

2.3.1 Secondary Electron Signals 40

2.3.2 Implemented Secondary-Electron Grids 41

2.4 Scintillating Fiducial Grids 44

2.4.1 Scintillation Signals 44

2.4.2 Implemented Scintillating Grids 46

2.4.3 Scintillation Signal Analysis 51

2.5 Phase Estimation of the Fiducial Grid Signal 54

3 Segmented Fiducial Grid Spatial-Phase Locking **59**

3.1 SEBL Field Calibration 61

3.2 Implementation on the Raith 150 SEBL System 63

3.2.1 The Raith 150 SEBL System 63

3.2.2 Implementation Strategy 64

3.3 Raith 150 Performance with Segmented-Grid SPL 65

4 SPLEBL via Sparse Sampling **75**

4.1 Sparse Sampling Strategy 75

4.2 Determination of Deflection Errors from Moiré Patterns 76

4.3 Sparse-sampling Algorithm 81

4.4 Sparse-sample spatial-phase locking with VS2A 83
4.4.1 Algorithm Implementation 83
4.4.2 Field-stitching Experiments 85

5 SPLEBL with Continuous Feedback **91**
5.1 Raster-Scan Pattern Generation 91
5.2 Real-time Spatial-Phase-Locking 96
5.2.1 Beam-Shift Extraction from the Grid Signal 96
5.2.2 Feedback Control Loop 100
5.2.3 Implementation on the Raith 150 System 103
5.3 Higher-order Distortion Correction 107
5.4 Field-Stitching Experiments 110

6 Silicon-on-insulator Integrated Optical Devices **121**
6.1 Integrated-Bragg Grating Theory 122
6.1.1 Integrated Waveguides with Gratings 123
6.1.2 Uniform Waveguide Analysis 125
6.1.3 Contra-directional Coupled-Mode Theory 128
6.1.4 Uniform Grating Analysis 133
6.1.5 Non-uniform Grating Analysis 135
6.2 Silicon-on-insulator WDM Filter Design 137
6.2.1 Silicon Based Optical Devices 137
6.2.2 Filter Specifications 138
6.2.3 Waveguide and Grating Design 142
6.2.4 Grating-Phase Tolerances 149
6.3 SOI WDM Filter Fabrication 153
6.3.1 Fiducial Grid Patterning 154
6.3.2 SPLEBL Exposure 154
6.3.3 Silicon Etching 157
6.3.4 Dicing and Polishing 158
6.4 SOI Filter Performance 158
6.4.1 Measurement Apparatus 158
6.4.2 Uniform Grating Results 161
6.4.3 Apodized Grating Results 165

7 Conclusion **169**

A Hydrogen Silsesquioxane: a Negative EBL Resist **173**

List of Figures

1.1 Laser interferometer configuration for EBL. 19
1.2 Vector-scan electron-beam lithography. 21
1.3 Raster-scan electron-beam lithography. 22
1.4 Sources of pattern-placement error in SEBL. 23
1.5 SEBL stitching errors. 24
1.6 Schematic of spatial-phase locked e-beam lithography. 26

2.1 Interference lithography. 34
2.2 MIT's standard interference lithography system. 35
2.3 Lloyd's mirror interference lithography. 36
2.4 Schematic of scanning-beam interference lithography. 37
2.5 Phase-mask replication of master gratings. 38
2.6 Secondary electron detector configuration for Raith 150 EBL system. 42
2.7 Fiducial grids designed for secondary-electron contrast. 43
2.8 Scintillation detector installed in VS2A SEBL system. 46
2.9 Scintillation detector in the Raith 150 system. 47
2.10 E-beam exposed pattern using PS-based scintillator and PMMA resist. 48
2.11 Moiré images of quenched 1-μm -period gratings in PVT- and PS-based scintillators. 50
2.12 Quenching response for PMMA, PS, and PVT based scintillators. . . 52
2.13 Modulation versus beam energy for 1-μm period UV-quenched gratings in the PVT-based scintillator. 53
2.14 Measured modulation of gratings quenched and imaged with EBL. . . 55
2.15 Standard deviation of phase estimates versus signal to noise ratio. . . 57

3.1 Segmented grid mode of spatial-phase locked electron-beam lithography. 60
3.2 Basic field calibration errors. 62
3.3 PMMA fiducial gratings for segmented grid test exposures. 67
3.4 SPLEBL written grating aligned to fiducial grating in PMMA. 68
3.5 Mean alignment error versus x-position in scan field for fast beam deflection. 69
3.6 Mean alignment error versus x-position in scan field for slow beam deflection. 70

3.7 Field scaling error versus beam velocity. 71
3.8 Segmented grid SPLEBL placement error histograms. 73

4.1 Moiré pattern formed by a 512 × 512 sample array of a 1-μm -period grid over a 528 μm field. 77
4.2 Field distortions observed in moiré patterns. 79
4.3 Field division for phase and frequency estimation. 82
4.4 Standard deviation of the field-correction parameters versus signal-to-noise ratio for sparse sampling. 86
4.5 Moiré patterns from scintillating grid.s 87
4.6 Stitched gratings patterned with sparse-sample SPLEBL. 87
4.7 Histograms of stitching error for sparse-sample SPLEBL. 88

5.1 Raster-scan strategies implemented on the Raith 150. 92
5.2 Raster-scan pattern generation subsystem for the Raith 150. 93
5.3 "Nested Ls" exposed by raster-scanning on the Raith 150. 95
5.4 Rotated fiducial grid and spatial-frequency spectrum for real-time spatial-phase locking. 98
5.5 Block diagrams of SPLEBL system with control loop. 102
5.6 Real-time spatial-phase locking system. 104
5.7 Standard deviation of shift error versus SNR. 106
5.8 Field distortion maps with first- and third- order corrections. 109
5.9 Resist and fiducial grid cross-section for real-time SPLEBL exposures. 111
5.10 Field-stitching test pattern for real-time spatial-phase locking. 113
5.11 Full pattern layout for field-stitching experiments. 116
5.12 Calculated phase-locking system response for physical disturbances. . 117
5.13 Stitched gratings exposed with real-time spatial-phase locking. 117
5.14 Stitching error histograms from real-time SPLEBL exposures. 119

6.1 Common waveguide geometries. 124
6.2 Various waveguide and grating geometries. 125
6.3 Integrated Mach-Zehender interferometer. 126
6.4 Refractive-index profile and finite-difference mesh points for a ridge waveguide. 129
6.5 TE-mode profile of a ridge waveguide with 50% duty-cycle grating region. 134
6.6 Canon ELTRAN SOI process. 139
6.7 WDM filter specifications and calculated response for 40Gbit/s data-rate and 100 GHz channel spacing. 141
6.8 SOI ridge waveguide refractive-index profile. 144
6.9 Single-mode condition for a SOI ridge waveguide. 146
6.10 Dispersion relation for the first four TE slab modes of a 1.4 μm SiO_2-Si-Air waveguide. 148
6.11 Contours of constant κ and n_{eff} for a range of waveguide geometries. . 150

6.12 SOI waveguide-grating structure for apodized filter 100 GHz filter. . . 151
6.13 Deterministic and stochastic errors in integrated gratings. 152
6.14 Secondary electron signal from W-fiducial grating under 125nm of HSQ resist. 155
6.15 Secondary electron contrast mechanism for buried W layer under HSQ. 156
6.16 Stitching measurements for sidewall grating pattern. 157
6.17 SEM images of apodized-sidewall gratings. 159
6.18 SEM image of polished SOI waveguide facet. 160
6.19 Waveguide transmission measurement apparatus. 161
6.20 Measured c-band TE- and TM-transmission spectra of a waveguide with a 1.5-mm long uniform grating. 162
6.21 Detailed TE- and TM-transmission spectra of a waveguide with a uniform 1.5-mm long grating. 164
6.22 Measured c-band TE- and TM- transmission spectra of a waveguide with a 3.0-mm long apodized grating. 166
6.23 Detailed TE- and TM-transmission spectrum of a waveguide with apodized, 3.0-mm long sidewall gratings. 167

A.1 Molecular structure of HSQ. 174
A.2 Development rate versus dose for HSQ exposed at 30kV. 176
A.3 Normalized thickness versus dose for HSQ exposed at 30kV. 176
A.4 Isolated lines patterned in HSQ at 30 keV. 177
A.5 100-nm period grating patterned in HSQ. 177

Chapter 1

Introduction

The planar fabrication process, combining lithography with additive and subtractive materials processing, revolutionized electronics manufacturing. By abandoning three-dimensional fabrication processes in favor a two-dimensional layered approach, the semiconductor industry gained large-scale integration, high product yield, and miniaturization. As a result, a variety of fields now embrace planar-fabrication technology. Chemists are moving from the reactor to the chip, and biologists from the petri-dish to the chip. Even the entertainment industry uses lithographic techniques to master digital versatile disks (DVDs).[1] Finally, large-scale integration of optical-communications components on a single chip remains a tantalizing, if illusive, goal for the communications industry.

Miniaturization is one of the primary benefits of planar fabrication, and the production of ever smaller electronic components continues to drive the development of lithography. Nevertheless, semiconductor manufacturing hardly represents the limit of lithographic resolution. Over twenty years ago 1.5-nm lines were patterned at a 4.5-nm pitch in inorganic resists with a scanning transmission electron microscope (STEM).[2]. Although not strictly lithography, the manipulation of atoms on a planar substrate with a scanning tunneling-microscope reached a natural patterning resolution limit.[3] Such techniques are orders of magnitude too slow for mass production,

so manufacturers must choose approaches that improve resolution while maintaining production rates.

While lithography systems continue to increase resolution and throughput, pattern-placement accuracy is often neglected. Pattern-placement is now a primary concern for the semiconductor industry because each lithographic step must overlay the previous one within a fraction of the minimum line width. To achieve this placement-precision on the wafer, features on the original masks must be accurately positioned. By 2013, the industry extrapolates, the minimum line-width on the wafer will be 18nm and the maximum pattern-placement error on a mask must be below 8 nm over a $\approx$100 cm^2 area. Making such a mask is equivalent in scale to positioning every building and street on Manhattan island to within 1 mm of its intended location. The industry acknowledges that currently there is no known technique that achieves this accuracy.[4]

Although important, the semiconductor industry is not the sole driver of lithographic technology. The planar-fabrication process also holds promise for miniaturizing and integrating optical-communications components. Many optical devices depend on interference effects, and interference in turn depends on coherence, not only of the light source, but of the physical structures used to manipulate light. This leads to stringent pattern-placement requirements for these structures; for example, diffraction grating teeth must lie at a precisely defined pitch, and any deviation, either local or long range, limits performance.

In contrast, semiconductor devices do not depend the on coherent interaction of electrons. If one transistor lies 10nm further than desired from a neighboring transistor, there will be little change in circuit function. However, a 10-nm placement-error in a diffraction grating represents a significant fraction of the wavelength of light, and will degrade performance. In addition, pattern-placement in optical devices is referenced to the wavelength of light, not to other devices. Thus, these devices demand both pattern-placement precision *and* accuracy, while electronic devices can

function with precision alone.

While optical lithography is used for mass production of electronic and optical devices, electron beam lithography (EBL) produces the masks for the critical optical-lithography steps. For some low-volume devices, particularly communications-wavelength semiconductor lasers, EBL is also used for production.[5] Scanning e-beam lithography (SEBL) systems write patterns by scanning a focused beam over the target substrate. Such systems allow arbitrary pattern generation and exceptional resolution, but they exhibit notoriously poor pattern-placement.

Pattern-placement errors arise from the fundamentally open-loop nature of EBL. To expose a feature in a desired location two things must happen. The substrate must be placed under the electron beam, and the beam must be positioned precisely on the sample. The relative position of the sample stage can be monitored to less than 1 nm by a laser interferometer, but a number of factors increase the beam position uncertainty. Examples include vibration, electro-magnetic interference, and thermal changes of sample, stage, or electron-optical components. Other factors are highlighted in section 1.1.

Spatial-phase-locked electron-beam lithography (SPLEBL) is a revolutionary approach to accurate pattern-placement that provides closed-loop feedback for beam positioning. Instead of relying on a stage position measurement, SPLEBL integrates a reference grid onto each substrate to be exposed. The reference grid produces a detectable signal which can be processed to determine the beam position and to feedback corrections. Because the grid is periodic, we use Fourier techniques to determine the signal's phase and calculate the beam position to within a fraction of one grid period. This thesis describes three implementations of spatial-phase locking on two different SEBL systems. The most sophisticated of these provides nanometer-level pattern placement with respect the fiducial grid.

Beyond IC mask production, Bragg-grating-based integrated-optical devices provide strong motivation for developing SPLEBL. This thesis addresses the design,

fabrication, and testing of silicon-on-insulator optical filters that rely on Bragg gratings patterned in the sidewalls of ridge waveguides. Sidewall gratings are created in the same lithographic step as the waveguide and offer a powerful way to vary the grating strength along the waveguide's length. These devices require the long range spatial-coherence of interferometrically generated gratings, but they also require complex pattern geometries unsuitable for interference lithography. As a result, SPLEBL provides the perfect solution by providing arbitrary patterning with long-range coherence.

1.1 Electron Beam Lithography Overview

E-beam lithography systems expose patterns in one of three ways: the system scans a focused e-beam over the target substrate, the system projects simple shapes formed by an aperture, or the system projects an entire pattern formed by a mask. These approaches are referred to as scanning beam, shaped beam, and electron projection respectively. Electron-projection lithography requires a mask made by one of the other two techniques, and will not be addressed in this thesis. Scanning-beam systems are most appropriate for spatial-phase locking and form a large segment of the mask-making and direct-write markets. The work presented here will exclusively concern scanning-beam systems; however, a spatial-phase-locking technique has also been proposed for shaped beam systems.[6]

Electron-beam lithography has four core components: the electron-optical column, the substrate positioning stage, the pattern generator, and the electron-sensitive resist. The column consists of the electron source, beam deflection system, and electron lenses. The substrate positioning system consists of a precision stage and a laser-interferometer measurement system. The pattern-generator converts a computerized design to a series of beam deflections according to a desired exposure strategy. To record the exposed pattern, the target substrate must be coated with an electron-

sensitive material often referred to as an e-beam resist.

1.1.1 EBL System Components

Electron sources for e-beam lithography must exhibit good current stability for dose uniformity and sufficient brightness (amps/cm^2/steradian) for high-current-density beams. Candidate sources include thermionic emitters, field emitters, and photo-emitters. Thermionic emission occurs when the thermal energy of electrons exceeds the potential barrier at the emitter surface. In field emission, a strong electric field creates a finite-width barrier between the emitter and vacuum, and electrons escape by quantum-mechanical tunneling.

Thermionic emitters exhibit excellent current stability but low brightness, while field emitters exhibit poor stability and high brightness. Hybrid thermal-field emitters combine the two emission mechanisms in a source that makes surprisingly minimal sacrifices in stability and brightness when operated under optimal conditions. Photo-emitters produce electrons through the photo-electric effect. Although attractive for multi-beam electron sources, where they are easily fabricated in planar arrays, questions remain about the stability and longevity of photo-emitters for lithographic applications.[7]

Once electrons have been generated they are accelerated away from the tip by an applied electric field. Electrons used for lithography usually have energies between 1 keV and 100 keV. To put this in context, non-transmission scanning electron microscopes use electrons with energies between 100 eV to 30 keV. For transmission electron microscopy (and a few isolated lithography techniques) beam energies increase to 100keV up to 1.5MeV. Electron beam systems for localized cancer treatment stretch the beam energy to 20MeV, and electron accelerators perform high-energy physics experiments at giga-electron volt energies. As a point of reference, 100 keV electrons travel at 0.55 times the speed of light.

The electron-optical column consists of a series of lenses and deflectors which

image the electron-source onto the desired point on the substrate. Electron lenses employ electric or magnetic fields, and with few exceptions create converging optics. Electron deflectors may be formed from capacitor-like plates, or from magnetic coils. Typically, one set of deflectors is designed to entirely remove the beam from the optical path. This process, referred to as beam blanking, prevents the beam from reaching the substrate. Intervening apertures in the column reduce beam current and control the numerical aperture of the electron-optical system. Later chapters present details of the two electron-beam-lithography systems used for spatial-phase locking.

Because electron beams can only be deflected over small areas, a precision stage is required to build up patterns from fields or stripes. Because EBL systems operate in vacuum, stages typically use roller bearings; however, at least one system uses an air-bearing stage with differential vacuum pumping.[8] Mirrors along each stage axis allow the use of a laser-interferometer for precise positioning. The interferometer compares the stage mirror position to the position of a reference mirror. Currently, commercial laser interferometers can measure changes in position to $\lambda/2048$ or ≈ 0.3 nm.[9] An additional beam can measure the yaw of the stage, and a another, redundant, beam can be used to compensate for mirror non-flatness. Figure 1.1 shows a simple laser interferometer configuration.

The pattern generator translates a computer aided design (CAD) pattern into a series of beam deflections and beam-blanker signals. The user's design usually consists of polygons and perhaps single-pass lines. A vector-scan pattern generator will break the pattern down into shapes, often trapezoids, than can be easily filled. The dose provided to any given feature is controlled by the beam dwell-time at each pixel. A raster-scan pattern generator simply sweeps the beam across the field and signals the beam blanker when to turn on and off to expose a pixel. Multiple-passes at different sweep rates may be used to provide different doses to different areas. More detail about vector- and raster-scan systems is given in section 1.1.2.

Electron-beam lithography would not be possible were it not for electron-sensitive

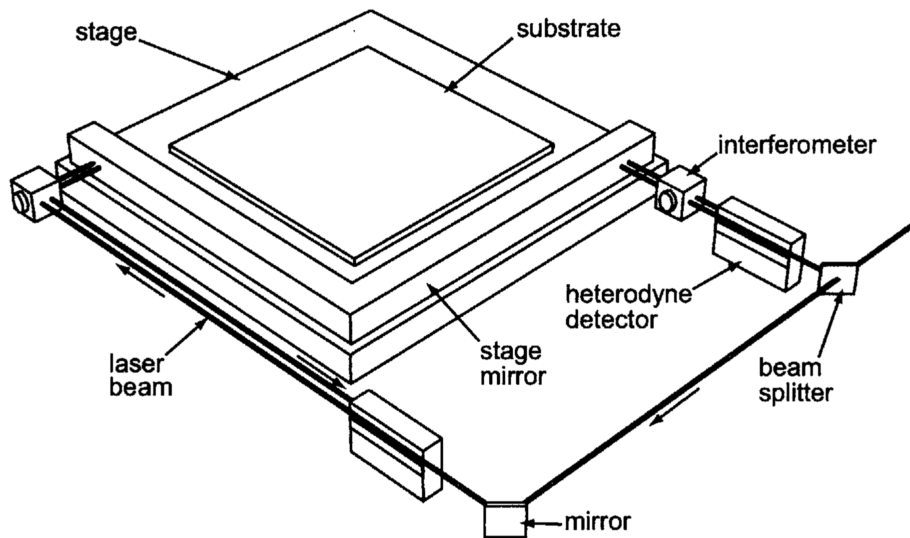

Figure 1.1: A laser interferometer allows precise (< 1 nm) measurements of stage position with respect to a reference frame. Heterodyne detectors measures the phase of optical signal in the electronic domain. Multiple beam passes (2 are shown) allow even more precise position measurement.

materials in which one can form an image. Like photoresists used in optical lithography, electron-beam resists are typically thin (hundreds of nanometers) polymer films. These resists can be either negative or positive tone depending on whether they undergo cross-linking or chain-scission when exposed to electron beams. E-beam resists may also be chemically amplified, that is, a single electron energy-loss event initiates multiple cross-linking or chain-scission events through a chemical catalyst. In almost all cases, resists are developed in a solution which selectively dissolves the lower molecular-weight regions. In some ultra-high resolution (sub-5-nm) experiments the electron beam directly sublimates an inorganic material such as AlF_3[10] or NaCl[2], but this process has proven too slow for most applications.

1.1.2 Exposure Strategies

SEBL systems divide the target substrate into addressable elements, roughly equivalent to pixels in a cathode-ray tube display. The size of these pixels is usually some fraction of the beam diameter so that exposed spots overlap and feature edges can be positioned precisely. SEBL systems are classified as raster or vector scan depending on whether the deflection system addresses every element or only those to be exposed.

In a vector-scan system, shown schematically in figure 1.2 **(a)**, the substrate remains in a fixed position while the e-beam is deflected over areas to be exposed. These areas can be filled via one of the ways shown in figure 1.2 **(b)**.[1] Because the beam cannot be reliably deflected more than about 1 mm, the total pattern is built up from small fields that are stitched together by precisely moving the stage. Vector-scan systems are particularly appropriate for sparse patterns where addressing each location on the substrate would increase exposure times. However, for dense patterns with many small features, the overhead required for the deflection system to

[1]The boustrophedonic mode, alternately scanning left-to-right and right-to-left, derives its name from the Greek for "ox-turning," referring to the course of a plough through a field. The term usually refers to ancient inscriptions of various languages written in this manner.[11]

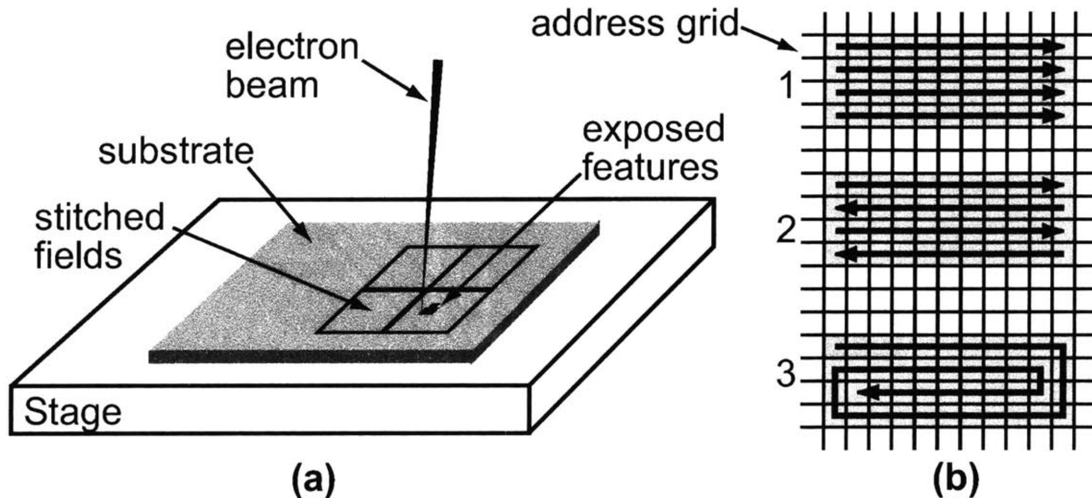

Figure 1.2: **(a)** A vector-scan EBL system keeps the substrate stationary while the e-beam is deflected over the areas to be exposed. **(b)** Features can be filled in one of three ways: 1. left-to-right only, 2. boustrophedonic, or 3. spiral.

stabilize between features can become significant. Vector-scan systems are typically used for research and prototyping, and occasionally for high resolution, low-volume production.

Raster-scan systems, first developed at Bell Laboratories[12], address every location on the substrate by rapidly scanning the beam in one direction while moving the stage in the orthogonal direction. The pattern is formed by turning the beam on only over exposed areas. The deflection range is still limited, but now instead of building the pattern from square fields, a raster-scan system builds it from long stripes. This simplified scanning strategy, illustrated in figure 1.3, allows raster-scan systems to deflect the beam more rapidly, and the continuously moving stage eliminates overhead time required for stage positioning. As a result, raster-scan systems tend to have greater throughput than vector-scan systems, and are often used for integrated-circuit mask production.

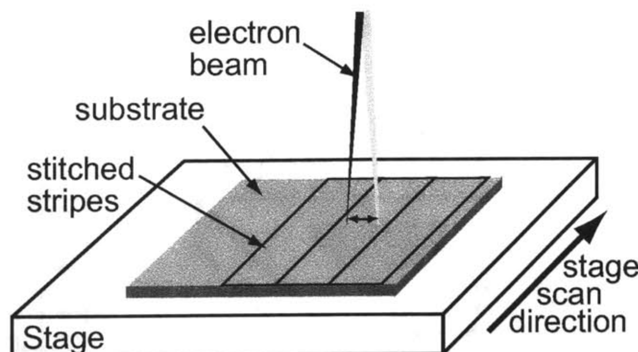

Figure 1.3: A raster-scan EBL system rapidly scans the beam along one axis, while the stage moves continuously along the orthogonal axis. The beam is turned on over areas of the substrate to be exposed.

1.2 Pattern Placement in SEBL

Pattern placement is a general term that encompasses the accuracy, precision, and repeatability with which one can position a pattern element on a substrate. Pattern-placement accuracy is simply defined as the positional deviation of a pattern element relative to an ideal, mathematically defined, coordinate system. Pattern-placement precision is defined by the positional deviation from an accepted standard. Finally, pattern-placement repeatability is defined as the positional deviation observed from exposure-to-exposure on the same patterning system.

In SEBL pattern-placement precision is achieved by measuring the stage position with a laser interferometer. If the stage is not located in the correct position, one can deflect the beam, or use an additional, shorter travel, stage to make fine corrections. This technique yields a precise measurement of the stage-mirror position with respect to a reference mirror, but there is no way to determine the position at which the beam strikes the sample. This must be inferred from intermittent calibrations, but such calibrations only correct for long-term drift, not for the many other errors which influence pattern placement.

The time scale of a particular error determines how it will influence pattern place-

Time Scale (seconds)

10^{-6}	10^{-2}	10^{1}	10^{4}	
Pixel to Pixel	Feature to Feature	Field to Field	Exposure to Exposure	Quasi-static
DAC quantization	charging			deflection non-linearity
	vibration	sympathetic beam/stage motion	field calibration	electron-optics distortions
	stray EM fields			
	interferometer quantization	thermal gradiants and variations	substrate mounting distortion	interferometer mirror errors
	deflection hysteresis			stage calibration

Figure 1.4: SEBL pattern-placement errors arise from a number of sources which affect the pattern differently depending on their time-scale. The slowest time scales (right) impact global placement accuracy, while shorter time scales (left) adversely affect placement from feature to feature.

ment. An error occuring on the time scale of the pixel-to-pixel beam motion (10 ns to 1 μs), for example instability in the least-significant bit (LSB) of a digital-to-analog converter (DAC), may not shift the centroid of a feature, but may appear as line edge roughness. Errors with longer characteristic times, such as mechanical vibration, may influence pattern placement between subsequently exposed features. Errors with very long time scales, such as thermal expansion or contraction, may introduce gradual errors spanning large areas of the substrate. Finally, some errors, like substrate distortion from mounting, are quasi-static. These errors may only change from exposure-to-exposure. Figure 1.4 assigns various sources of error to the most appropriate time scale.

SEBL builds up a pattern from a set of stitched fields or stripes, and errors occuring at the field or stripe boundaries are termed stitching errors. These errors are highly visible because features exhibit discrete offsets or breaks at the boundary. Figure 1.5 illustrates typical stitching errors. When examining stitching errors one

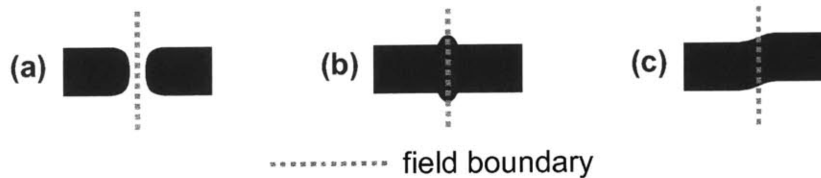

Figure 1.5: Stitching errors occur at field and stripe boundaries. The resulting pattern can exhibit **(a)** breaks from incomplete exposure, **(b)** bulges from overlapped exposures, and/or **(c)** discrete offsets.

usually observes a deterministic and stochastic component. The deterministic part, or mean stitching error, arises from factors including miscalibration of the deflection system, uncorrected distortion in the deflection field, or drift of the beam or stage. The stochastic component usually arises from inaccuracy in stage-positioning, system or substrate charging, vibrations, or interferometer quantization.

To quantify the impact of placement errors let us examine mask specifications on the semiconductor industry road map and specifications for recent-generation EBL systems. The International Technology Road map for Semiconductors (ITRS) specifies the maximum placement error allowable on an IC mask for each generation of chips. These generations, or nodes, are classified by the minimum half-pitch printed in a dynamic random access memory (DRAM) structure. The minimum MOSFET gate width for a microprocessor at a given node can be substantially smaller than the minimum half-pitch. Table 1.1 lists the maximum image placement (IP) error permitted for 4× reduction masks through the 22-nm node (2016). As shown, no known manufacturable solutions exist beyond 2010 for placement at the 8-nm level.[4] The 1× mask used in proximity x-ray lithography places even more stringent requirements on pattern-placement.[13]

Pattern-placement specifications provided by EBL tool manufactures are informative, but one must always consider the exposure strategies and measurement techniques behind these claims. ETEC MEBES (Manufacturing Electron-Beam Exposure System, Applied Materials, Santa Clara, CA) raster-scan tools are widely used for IC

mask writing. ETEC's latest generation tool, the eXara, targets the 100 nm node for production mask making and the 70 nm node for research and development.[14] Although image placement results are not yet published, presumably the system targets 21-nm accuracy to meet road map specifications. The previous-generation tool, the MEBES 5500, specified 30 nm maximum placement errors.[15] JEOL (Japanese Electronic Optical Laboratory) specifies 30 nm placement accuracy for it's JBX-9000MV mask writer as well.[16] NuFlare Technology (formerly a division of Toshiba Machine Co., Ltd.) claims 12 nm 3σ positioning accuracy for its new EBM-4000 shaped-beam tool.[17]

The most well-documented pattern-placement effort to date is NTT's EB-X3 x-ray mask writing tool. NTT has published detailed data showing sub-15nm placement accuracy over repeated mask exposures, and 7 nm accuracy as a best result.[18] All of these tools use multiple exposures of each pattern element to "average" placement errors, and they frequently correct for relative drift between the beam and the stage. The NTT system also applies pattern-specific corrections by writing the mask, measuring placement errors, and correcting these errors in a subsequent exposures. Spatial-phase locked e-beam lithography, described in the next section, seeks to improve pattern placement further, and eliminate these time consuming steps.

Year	2001	2002	2003	2004	2005	2006	2007	2010	2013	2016
node (nm)	130	115	100	90	80	70	65	45	32	22
Max. IP Error (nm)	27	24	21	19	17	15	14	11	8	6

under investigation no known solution

Table 1.1: International Technology Roadmap for Semiconductors mask image placement specifications adapted from reference [4]. The roadmap projects specifications for optical projection lithography through at least 2006, and extreme ultra-violet (13-nm wavelength) for 2007 and beyond.

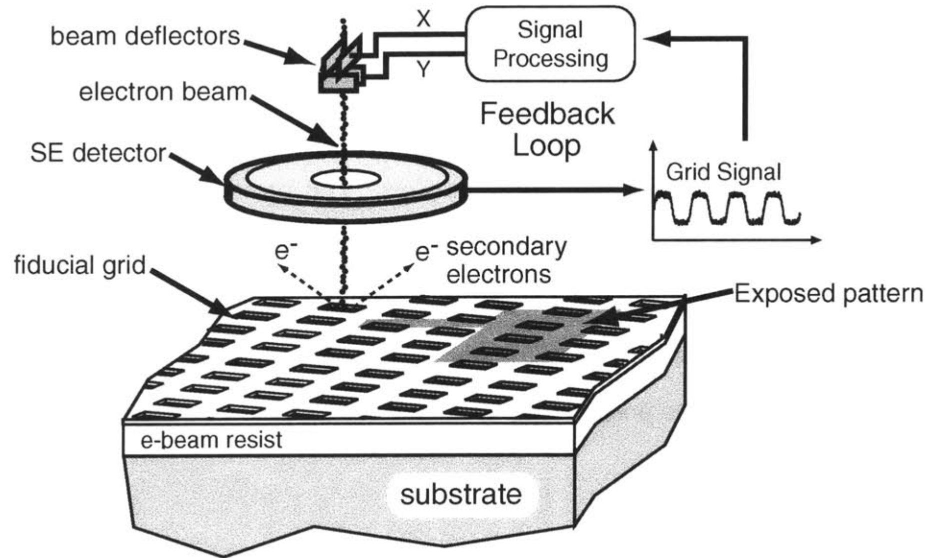

Figure 1.6: Spatial-phase locked e-beam lithography provides feedback control for accurate pattern placement by monitoring the signal produced by a fiducial grid on the substrate. Because the grid signal is periodic one can use phase detection to locate the beam within a small fraction of one period.

1.3 Spatial-Phase-Locked Electron-Beam Lithography

Spatial-phase locked electron-beam lithography, shown schematically in figure 1.6, provides feedback control for precise beam positioning. By monitoring the phase of the periodic signal produced by the fiducial grid, one can ascertain the position of the e-beam on the substrate. As a result, SPLEBL provides inherent pattern placement precision and repeatability, but the absolute pattern-placement accuracy depends on the accuracy of the grid itself. The second chapter of this thesis addresses the fiducial grid requirements, the processes involved in transferring the grid to the substrate, and metallic and fluorescent grid materials.

Several approaches to spatial-phase locking have been implemented and are categorized by whether they provide continuous or discontinuous feedback. Discontinuous feedback modes, often described as "look-then-write" modes, scan the beam over the grid before exposing each field. After correcting the beam deflection, the pattern

is written normally. Chapter 3 describes the earliest implementation of SPLEBL in which the fiducial grid is segmented to small, unused portions of each field. This technique sacrifices substrate area for the grid, but one can use strongly scattering materials (i.e. heavy metals) and one can examine the grid at high doses. These advantages yield high signal-to-noise ratios (SNR), and, as a result, precise phase locking. The integrated optical devices described in chapter 6 were patterned using segmented-grid spatial-phase locking.

Another discontinuous feedback approach, addressed in chapter 4, relies on sparsely sampling the fiducial grid using an array of points. These samples cover the entire field, but they are taken at sub-exposure threshold doses. Typically the sample spacing is larger than the grid period, and one detects an aliased signal, or moiré pattern. In the sparse-sampling mode of SPLEBL, the grid covers the entire substrate and must not perturb the electron beam. As a result, it is difficult to obtain high SNRs using this technique, but no substrate area is sacrificed.

Chapter 5 describes the implementation of a continuous feedback mode of SPLEBL. The system constantly monitors the signal from a global grid as the beam scans across the substrate. This technique is most naturally implemented with raster-scan exposure strategies. Ideally, when the system addresses areas of the pattern that are not to be exposed, a reduced-current beam would allow the grid signal to be monitored without exposing the resist. In exposed areas the beam would remain at full current. While the discontinuous feedback modes correct for stage errors and slow beam drift, continuous feedback corrects for more rapid variations. No substrate area is required, and continuous sampling makes low SNRs more tolerable.

1.4 Bragg-grating optical filters via SPLEBL

Although optical fibers carry almost all high-bandwidth, long-distance communication signals, traditionally these signals were not manipulated optically. If a signal

needed to be rerouted, it was detected electronically and retransmitted with another laser. Likewise, amplification was usually synonymous with regeneration: the signal is detected and retransmitted to boost it's power and reduce the effects of dispersion.

In recent years, many of these electronic functions have moved to the optical domain. Optical amplification can now be accomplished using Erbium-doped optical fiber or Raman fiber amplifiers. Fiber Bragg-gratings and thin-film filters selectively reflect a single channel from a multi-channel spectrum for rerouting. Specialty fibers and chirped fiber gratings now compensate for dispersion. Many see the next evolution in optical communications in the miniaturization and integration of optical components on a single chip. It is hoped that planar processing will provide new functionality while reducing size and cost compared to large optical systems or long fiber-based devices.

Semiconductor processes and tools can be used to build integrated-optical devices, but materials, fabrication concerns, and tolerances differ. Integrated-optical devices often require accurate pattern placement within a fraction of the wavelength of light. These tight tolerances arise when interference or other coherence based effects are used to control light on the chip. For example, Bragg-grating devices require deep sub-micron features to be patterned with nanometer scale placement accuracy over long distances. Chapter 6 describes the fabrication of 225 nm period gratings in silicon-on-insulator rib waveguides with placement errors of 2.6 nm (1-σ).

These gratings were patterned in the sidewalls of the waveguides using SPLEBL and reactive-ion etching. The sidewall-grating approach allows the waveguide and the grating to be patterned in a single lithographic step. Because the grating depth is defined lithographically, sidewall gratings are particularly attractive when one wishes to change the grating strength along the waveguide. If the grating-strength is varied appropriately, the reflection and transmission spectra are "apodized", that is the side-lobes in the spectra are reduced. Bragg gratings for narrow-band filters must remain coherent over several millimeters, but the sidewall grating geometries cannot

be patterned with interference techniques. SPLEBL provides a patterning solution by combining the long-range spatial coherence of interference lithography with the arbitrary patterning capabilities of SEBL.

Chapter 2

The Fiducial Grid

> ... we need some fiducial point or standard of reference, by which we may ascertain the direction in which we are drifting. *James Clerk Maxwell*[19]

Although Maxwell was addressing human philosophy, a phenomenon only slightly more chaotic than e-beam lithography, his statement applies to all systems. In e-beam lithography, it is impossible to know where the beam drifts without a reference. As a result, a high quality fiducial grid forms the foundation of spatial-phase-locked e-beam lithography. This chapter addresses the requirements placed on the fiducial grid and efforts made to meet those requirements.

First and foremost, the grid's spatial-phase must be predicatable over the exposure area. Some applications only require a repeatable grid, while other applications, especially those in optics, require spatially-coherent grids. A spatially-coherent grid exhibits a predicatable phase-progression as one changes grid location. Although a linear-phase progression is ideal, one could potentially correct for non-linearities if the phase-progression is predicatable and a starting location is known.

In addition to spatial-coherence, resolution plays a key role in determining spatial-phase-locking accuracy. Finer-period grids allow more precise spatial-phase locking. If the beam shifts a given distance, a finer-period grid exhibits a larger phase shift than a coarser grid. MIT's Space Nanotechnology Laboratory recently developed

technology to pattern linear grids over areas up to 900 cm^2 with periods as small as 200 nm.[20] MIT's NanoStructures Laboratory has the capability to make grids with reduced spatial coherence and areal coverage with a period of 100 nm.[21]

Even if a grid is perfectly accurate, its usefulness hinges on the e-beam system's ability to detect its presence. The grid's signal-to-noise ratio (SNR) directly determines the phase-locking precision one can achieve. Here one must strike a difficult balance. The grid must interact sufficiently with the electron beam to produce a detectable signal, but the grid must not interfere with the exposure of the resist.

The interaction of an electron beam with a given material generally produces photons, electrons, or both. These photons and electrons can be categorized by their energies. For example, when a high-energy electron beam strikes a material a fraction of the electrons backscatter out of the material while retaining a large fraction of the incident electron's energy. At the same time, outer-orbital electrons are ejected from the material as low-energy secondary electrons. An electron beam can also generate scintillation (low energy photons) or x-rays (high energy photons). Backscattered and secondary electrons along with low energy photons all provide useful signals for spatial-phase locking.

Aside from exhibiting a predicatable phase-progression and producing a detectable signal, the fiducial grid must be compatible with the entire e-beam lithography process. If the grid is placed on top of the e-beam resist, it must be chemically compatible in both application and removal. Spin coated grid materials must use casting solvents that do not attack the e-beam resist. If the grid material is deposited or etched, these process steps cannot adversely affect the resist performance. In addition, the technique used to pattern the grid, often an optical exposure, must not expose the e-beam resist. Finally, the grid must be easily removed between exposure and development steps.

2.1 Patterning the Grid

The fiducial grid's resolution and spatial-phase coherence are largely determined by the patterning technique. Grids and gratings requiring long-range spatial coherence are typically produced by one of two methods. The first is to position a substrate with a precision stage and form the grating line by line. This is the approach of the traditional grating ruling engine where each line is inscribed by a stylus. The accuracy of the grating is limited by the mechanical accuracy of stage and stylus positioning.

Alternatively, one can produce all the lines in a grating pattern by interfering two coherent beams of light. This technique is referred to as interference lithography, and the accuracy of the grating is limited by the quality of the interfering wavefronts. The most advanced methods of grating production combine precision stage motion with interference-lithography techniques to produce coherent gratings over lengths up to a meter in photo-sensitive optical fiber [22] or over areas up to 900 cm^2.[20]

2.1.1 The Master Grid

For wide-spread use of spatial-phase locked e-beam lithography it is advantageous to produce a master grid and replicate it onto each substrate to be written. In this way, the extensive effort required to produce error-free grids need only be expended on the master. Interference lithography has been the standard for producing high-quality gratings for spectroscopy, filtering, dispersion compensation, and laser feedback. Now scanning-beam interference lithography promises to produce the most accurate gratings ever.

Interference-lithography (IL) uses the standing wave pattern formed between two interfering beams of light to expose a radiation sensitive material. Figure 2.1 illustrates this process in greatly simplified form. While it is difficult to produce large planar wavefronts, accurate spherical wavefronts are more accessible. However, spherical waves produce a non-linear phase progression of the grating.

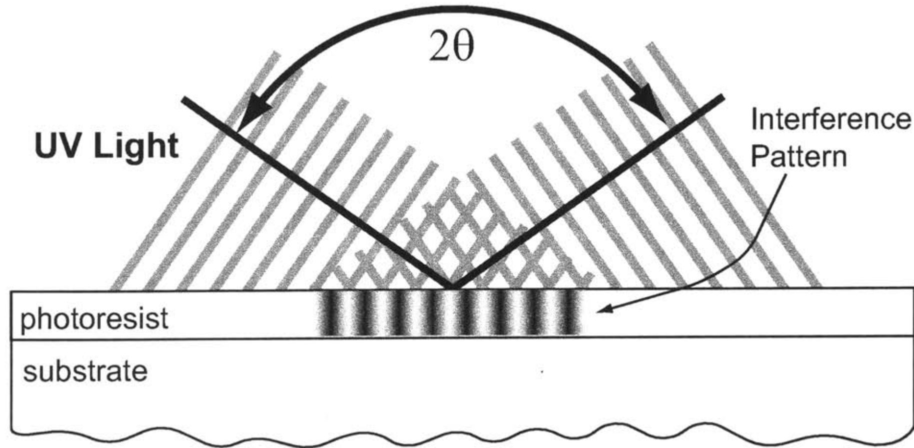

Figure 2.1: Interference lithography records the standing-wave pattern produced by two intersecting plane or spherical waves. The grating period is $\lambda/(2\sin\theta)$.

Figure 2.2 depicts the IL system used to expose many of the fiducial grids discussed here. Light from an Ar-ion laser (351 nm wavelength) is divided by a beam splitter and routed to each arm of the interferometer. Because vibration and air turbulence alter the beam path lengths, feedback control is necessary to lock the fringes in position.[23] An microscope objective lens and a spatial filter produce approximately spherical wavefronts. The spatial filter ensures high quality wavefronts, but the spherical wave interference pattern produces a family of hyperbolas, not a linear grating. Nevertheless, the central portion of this grating remains highly linear, and is useful for the development of spatial-phase locking.

Ferrera carefully analyzed the phase-progression resulting from interfering spherical wavefronts in MIT's IL system.[23, 24] When exposing 200-nm period gratings the phase error for a perfectly aligned interferometer is below 100 nm within a 1 cm^2 area. While this area is sufficient for many integrated optical devices and for testing SPLEBL, an area of $\approx 10\text{cm}^2$ is required for a single-die proximity x-ray mask, and an area of $\approx 100\text{cm}^2$ is required for a projection lithography mask. If a distortion-free grid cannot be produced over such an area, one must measure the distortion and

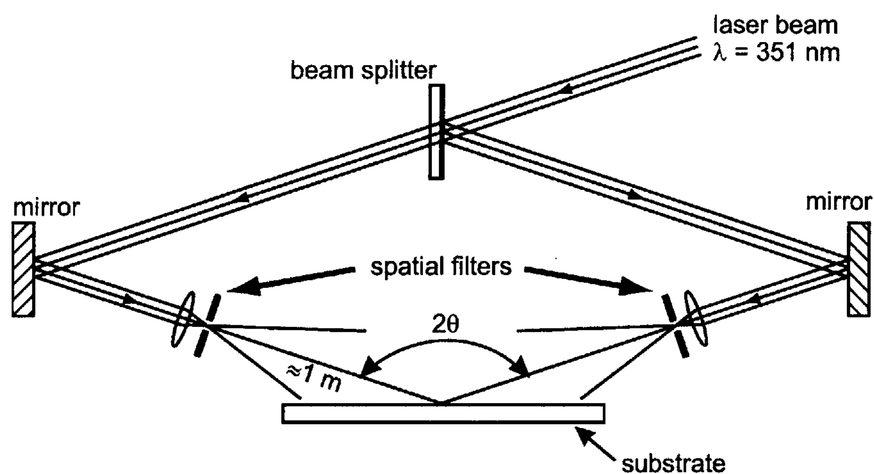

Figure 2.2: Detailed diagram of MIT's standard interference lithography system. A single laser beam is split and recombined in a two-arm interferometer. Objective lenses and spatial filters produce approximately spherical wavefronts.

correct for this during the SPLEBL exposure.

We also used a Lloyd's mirror interferometer to produce grids for spatial-phase locking. This variation of interference lithography, shown in figure 2.3, combines a wavefront directly from a spatial filter with a wavefront reflected from a fixed mirror placed at a right angle to the substrate. The angle of the interferometer assembly with respect to the incident beam determines the grating period. The Lloyd's mirror interferometer produces comparable period gratings to the more complex IL system described above, and the rigid sample and mirror mounting make fringe-locking electronics unnecessary. In addition, there is no need to separately align the two beam paths, or to balance the intensity in the two beams. The grating accuracy produced by the Lloyd's mirror is limited by mirror flatness and cleanliness. Mirror non-flatness produces distorted wavefronts, and particles on the mirror introduce additional interference patterns.

Scanning-beam interference lithography produces highly-linear gratings compared to traditional IL.[20] As shown in figure 2.4, a scanning-beam system interferes two

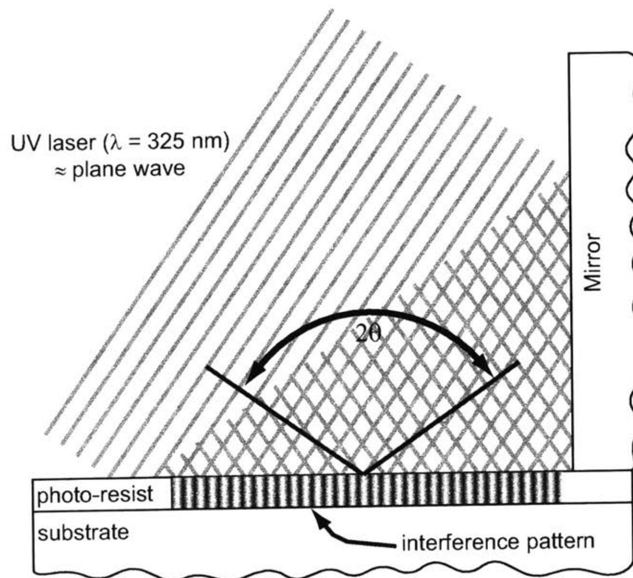

Figure 2.3: A Lloyd's mirror interferometer produces a grating pattern with a mirror rigidly fixed at a right angle to the substrate. The reflected wave from the mirror interferes with the direct wave from the source.

small beams ($\approx$ 1mm diameter) on the substrate at the beam-waist. The small beam size minimizes wavefront distortion from the focusing optics. The system scans a laser-interferometer-controlled stage under these two interfering beams to pattern an entire substrate. Precise control of stage position and environmental parameters allows these gratings to remain coherent over long distances.

2.1.2 Replicating the Grid

The scanning-beam IL system at MIT is intended to produce metrological standards, not to produce the grid for every substrate exposed with SPLEBL. We expect that these master gratings and grids will be replicated using phase-mask exposures. The phase mask is formed by etching the master grating into a transparent substrate. If the etch depth corresponds to a π phase shift for the illuminating wavelength, the zero-order transmission is suppressed. As shown in figure 2.5, the ± 1 diffracted orders interfere below the phase mask to produce a grating with half the original period. One

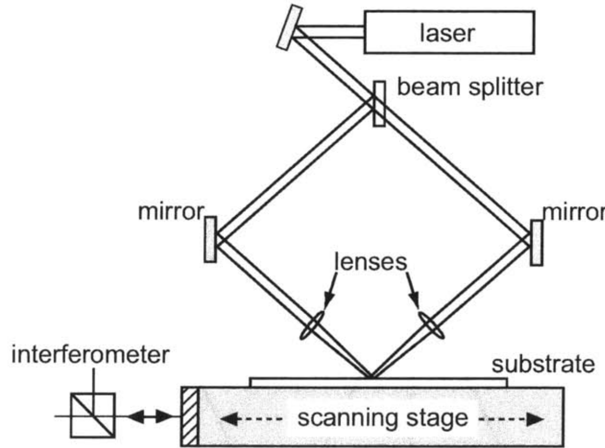

Figure 2.4: Schematic of scanning-beam interference lithography. A laser-interferometer-controlled stage scans the substrate under a small two-beam interference pattern.

can also obliquely illuminate a phase-mask and use the zero and -1 orders to produce a grating of identical period. However, it is more difficult to balance the intensities of the two orders in this approach. Grids can be produced by two orthogonal exposures, or perhaps by direct exposure of a grid phase mask.

2.2 Backscattered Electron Grids

When an electron beam impacts the target substrate, a fraction of the electrons backscatter out of the material. One can detect these backscattered electrons and form an image whose contrast is based on backscattering probability. Electron-beam lithography systems often use these images to calibrate the deflection system and to align multiple lithographic layers. This signal can be used for spatial-phase locking as well, particularly in the segmented grid mode.

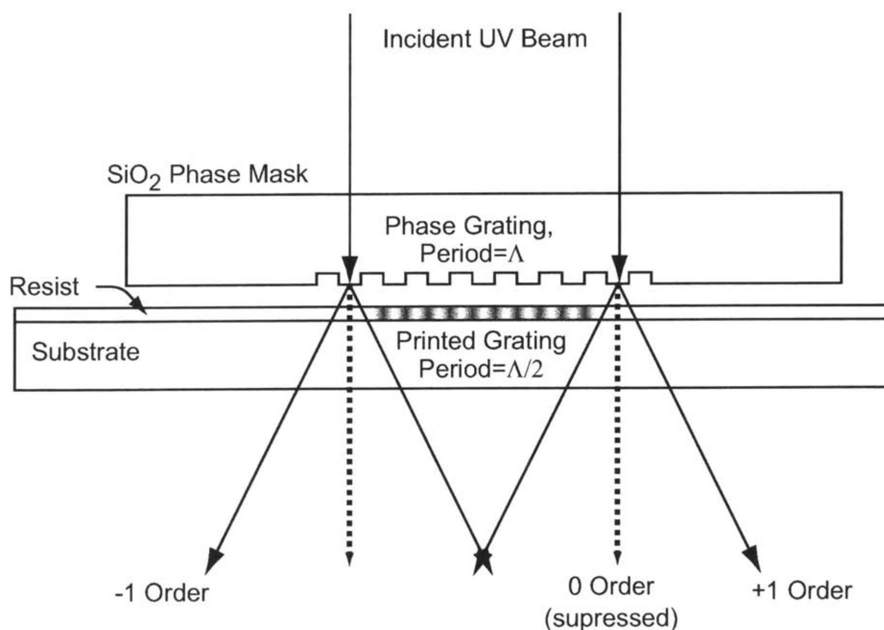

Figure 2.5: Master gratings can be replicated by bringing a binary phase mask in close proximity to the target substrate. The ± 1 orders interfere to produce a grating with half the periodicity of the original.

2.2.1 The Backscattered Electron Signal

Contrast in a back-scattered electron (BSE) images is due primarily to differences in atomic number and density. The more protons and electrons present in a given volume, the more likely the incident electron will scatter off an atom (or multiple atoms), and exit the substrate. The best BSE grids consist of heavy elements on light element substrates. For example bulk silicon yields ≈ 0.2 backscattered electrons for each 30 kV primary electron. In contrast, tungsten's backscatter electron yield is ≈ 0.5 at 30 kV.[25]

In planar processing the heavy-element layer is usually thin, and though it increases the probability of backscattering, one does not obtain the full contrast observed for bulk films. For the same reason light-element grids on a heavy-element substrates do not work well because the primary electrons pass through the lighter-element material and backscatter from the heavy-element material below. Fortu-

nately, most substrates used in e-beam lithography are composed of lighter-elements.

Backscattered electrons are detected with large area scintillation or solid-state detectors placed in close proximity to the substrate. Scintillation detectors convert the electron energy into light which is then detected by a photo-multiplier. Solid-state detectors are based on buried PN junction diodes in which the incident electron generates additional electron-hole pairs.

2.2.2 Implemented Backscattered Electron Grids

Because high atomic number materials strongly scatter electrons, it is inadvisable to place them on top of the resist film. Doing so would lead to large forward scattering below the grid lines, with little scattering in the open spaces. This scattering impacts line edge acuity and limits the ultimate resolution of the exposure. Instead grids intended to provide backscattered electron signals are only used in the segmented grid mode where the grid is isolated to unused portions of the substrate. Because the backscattered electrons are largely unaffected by the resist film, placing the grid beneath the resist presents no problems in detecting the signal.

Previous work using the segmented-grid mode of spatial-phase locking was performed with gold grids on a silicon nitride x-ray mask.[23, 26] In this case the grid signal can be acquired by detecting backscattered or transmitted electrons. Because the x-ray mask is a 1 μm thick membrane composed of light elements more electrons pass through the clear areas than areas where the grid resides.

The integrated-optical devices described in chapter 6 were fabricated using direct-write SPLEBL on a silicon-on-insulator substrate. The fiducial grating (only 1D phase-locking was used) consisted of 30 nm thick tungsten lines below 125 nm of hydrogen-silsesquioxane (HSQ) negative resist. In this configuration the increased backscattering from the tungsten lines yielded additional secondary electrons at the HSQ surface. These secondaries were detected using the Everhart-Thornley detector described in the next section. Section 6.3 describes the process in more detail.

2.3 Secondary Electron Grids

2.3.1 Secondary Electron Signals

A high-energy electron beam impinging on most materials will produce secondary electrons. These electrons tend to have low energies (<50 eV), which means that they can travel only short distances in a material before losing their energy in inelastic scattering. In practice, this leads to a secondary electron range from 2nm to 20 nm in metals and from 5 nm to 50 nm in dielectrics.[27] Variation in escape depth and differences in the probability of producing secondary electrons give rise to secondary-electron contrast among materials.

As one might expect, this phenomenon can be used to create a fiducial grid where the grid lines yield either a smaller or larger number of secondary electrons than the underlying resist. Unfortunately, the published literature concerning secondary yields provides a weak starting point for choosing grid materials. Yield measurements are strongly influenced by charging, contamination, and material quality. In addition, most well-controlled experiments are conducted with very short pulses of electrons, a situation far different from that found in an SEBL system. Nevertheless, the literature does reveal that most metals have secondary-electron yields from 0.1 to 0.3 for 10 kV primary electrons. Aluminum yields $\approx$0.25 secondaries for each 10kV primary [25].

The small escape depth of a secondary electron also gives rise to topographic contrast in the acquired signal. When a primary electron enters a material near an edge parallel to the primary beam, secondary electrons escape along this vertical surface. Thus, material edges often appear as bright regions in secondary-electron micrographs.

The material and topography of a sample largely determine its appearance in secondary-electron images, but differences in electric potential are also observed. These potential differences arise from an external bias or by charging of the sample with the electron beam itself. The electric fields created near the sample deflect

low-energy secondary electrons toward or away from the detector, creating a voltage-contrast image. Sufficiently strong fields can suppress secondary-electron emission entirely. Voltage-contrast mechanisms could potentially improve the signal-to-noise ratio of metallic fiducial grids.[28]

Regardless of the contrast mechanism, there are two standard types of secondary-electron detectors. The Everhart-Thornley (ET) detector consists of a metal grid placed in front of a scintillating material. The positively-biased grid steers and accelerates the secondary electrons toward the scintillator. Coating the scintillator with a thin metal layer prevents charging and reflects light into a light pipe which directs it to a photomultiplier tube.

In-lens secondary-electron detectors have become a popular alternative to ET style detectors. The in-lens detectors in LEO SEMs and Raith 150 EBL systems harness the final lens's electrostatic field to accelerate the secondary electrons back through the lens bore and into an annular scintillation detector. In-lens detectors only collect secondary electrons from the imaged area, so the background level and noise are reduced. In addition, secondary electrons are accelerated to energies equivalent to the bias on the final lens (8 kV for the LEO system), versus the grid bias (300V for the LEO ET detector). The higher energy electrons generate more photons when they impact the scintillator. Figure 2.6 shows the detector configuration in MIT's Raith 150 EBL system.

2.3.2 Implemented Secondary-Electron Grids

Several combinations of materials can form suitable secondary-electron-emitting grids. The most simple in concept, shown in figure 2.7 (**a**), consists of an electron sensitive resist with a thin (< 10 nm) low-atomic-number metal lattice on top. The metal will typically exhibit a higher secondary-electron yield than the polymer, giving rise to material contrast. Provided the atomic number is low enough, and the metal is thin enough, the grid's impact on patterning will be negligible. An array of metal dots, as

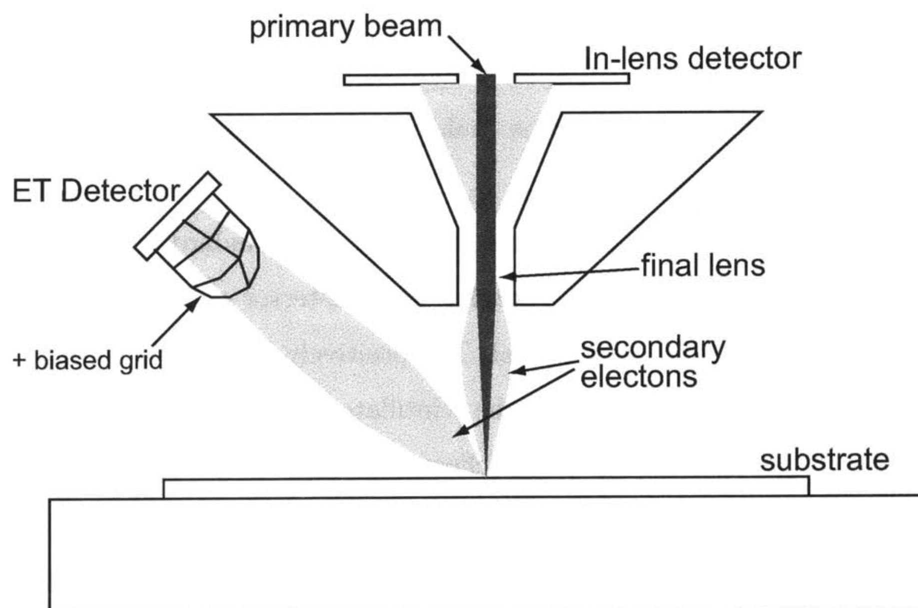

Figure 2.6: In the Raith-150 EBL system secondary electrons can be detected by an Everhart-Thornley style detector mounted to the side in the vacuum chamber, or by an in-lens secondary electron detector.

opposed to a lattice, also forms a grid, but dots leave no conductive path to bias the grid for voltage contrast experiments.

It can be difficult to pattern a metal grid on top of a polymer resist, but we have developed a process to form an aluminum lattice on poly-methyl-methacrylate resist. It is helpful to place a thin silicon dioxide interlayer on top of the PMMA and then pattern a positive resist (Sumitomo PFI-88) into an array of posts. After evaporating aluminum and removing the resist in iso-propyl alcohol, one is left with an aluminum lattice on the oxide layer above the PMMA. One can expose the resist through this multi-layer structure and then remove it with hydro-fluoric acid before developing the PMMA. This process has proven invaluable for testing the SPLEBL concept, but it may prove difficult to use with other resists. Zhang describes the process and alternatives in more detail. [28]

Figure 2.7(**b**) shows a fiducial grid formed by patterning an optical resist on top of a thin uniform metal layer. The metal layer must remain thin to minimize scat-

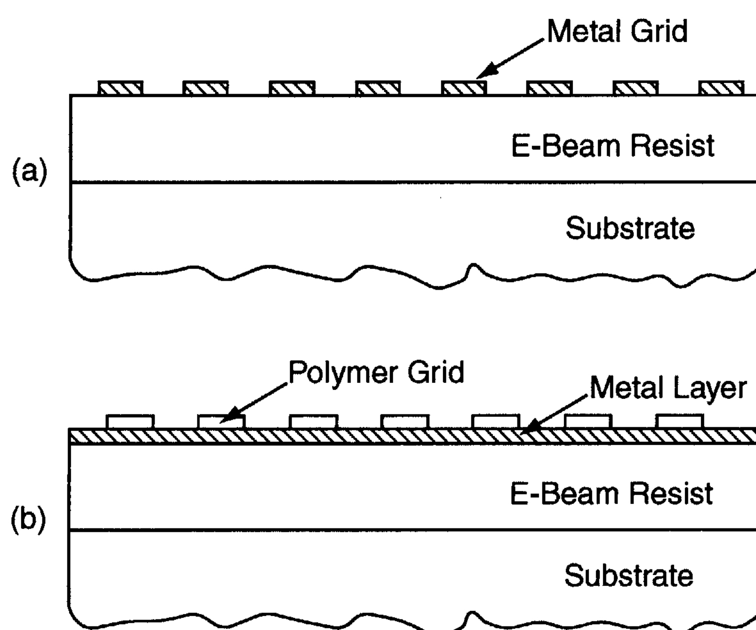

Figure 2.7: Fiducial grids based on secondary electron contrast. **(a)** A metal grid or lattice yields more secondary electrons than the underlying e-beam resist. **(b)** A polymer grid yields fewer secondary electrons than the underlying metal layer, and blocks secondaries emerging from the metal beneath the polymer.

Uniform Layer	Grating Layer	SE Yield Ratio (20kV)
Au	PMMA	1.14
Ni	PMMA	1.18
Cr	PMMA	1.07
Al	PMMA	1.56
PMMA	Au	2.28
PMMA	Cr	1.91

Table 2.1: Secondary electron yield ratios for metal on PMMA and PMMA on metal fiducial gratings. The data was acquired by James Goodberlet using the in-lens detector in a LEO SEM.[29]

tering, but the resist layer can be somewhat thicker because the light-element based polymers interact less with the primary electron beam. Material contrast between the higher-yield metal and the low-yield polymer allows the grid signal to be detected. Secondaries generated in the metal directly under the polymer are prevented from reaching the detector. This technique has the advantage that any scattering introduced by the metal is uniform over the entire substrate. In addition, the resist can be patterned by optical exposure and standard development with no need for deposition and lift-off steps.

James Goodberlet investigated both metal-on-polymer and polymer-on-metal gratings to determine the secondary-electron (SE) yield ratios.[29] Table 2.1 shows his results for several materials combinations imaged with a 20-kV electron beam.

2.4 Scintillating Fiducial Grids

2.4.1 Scintillation Signals

Scintillating materials, those that emit photons when struck by electrons, can also form fiducial grids. The ideal scintillator exhibits good efficiency, resistance to damage, a fast response time, and straightforward deposition and patterning. Crystalline inorganic scintillator, like NaI, offer high efficiency and damage resistance, but re-

spond too slowly for rapid sampling in an e-beam system. In addition, they can be difficult to deposit in thin films.

Alternatively, organic scintillators can be cast in polymer hosts and spin coated onto the sample. Host polymers are primarily hydro-carbon based and do not strongly scatter primary electrons. In general, organic scintillators also exhibit faster response between excitation and emission than inorganic systems. Finally, ultra-violet light permanently quenches certain organic scintillators; thus, the grid can be patterned without chemical development or topography. These advantages directed us toward organic scintillators for spatial-phase locked e-beam lithography.

Scintillation occurs when the electron beam excites bound electrons in the host polymer to higher energy states. This energy is transferred, sometimes through an intermediate molecule, to fluorescent molecules where the relaxation of the electron to a lower energy state produces a photon. The primary electron has the potential to produce several photons as it passes through the scintillating layer. However, electron beam induced damage to the host polymer or the scintillating molecules may prevent subsequent electrons from inducing scintillation.

After the scintillator produces a photon it must be detected. The detection system consists of a lens or mirror that collects the light, and a detector that converts the optical signal into an electrical signal. Two such systems were developed by James Goodberlet and Feng Zhang. The first, installed in MIT's VS2A system, consisted of a partial elliptical-mirror and a small photo-multiplier tube (Hamamatsu R7400U). The geometry of the vacuum chamber and stage dictated the design, shown schematically in figure 2.8. The photo-multiplier's current output was routed to a current pre-amplifier[1] and then to an image acquisition card [2] in VS2A's control computer.

The Raith 150 system's vacuum chamber and column facilitate light detection. The final lens slopes away from the sample allowing optics to be placed to the side. A

[1]Model SR570, Stanford Research Systems, Sunnyvale, Ca.
[2]Model DT2851, Data Translation, Marlboro, MA.

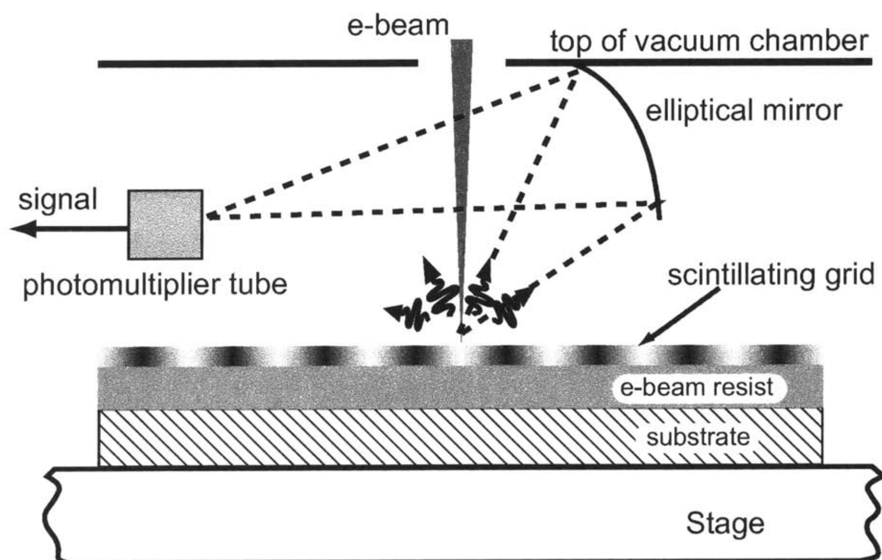

Figure 2.8: MIT's VS2A SEBL system required a thin elliptical mirror to capture light from the scintillator and redirect it to a photon multiplier tube.

lens collects the light and two mirrors focus it on a photomultiplier tube (Hamamatsu R6094) outside the chamber. The lens is coated with a 2 nm thick layer of chromium to prevent charging. An optical high-pass filter in front of the PMT allows transmission of the 420-nm wavelength scintillation, while blocking scattered light from the 632-nm wavelength HeNe laser used in the stage interferometer. Figure 2.9 illustrates this arrangement. Once again, the SR570 amplifies the PMT signal, converts it to a voltage input for the image acquisition and spatial-phase locking electronics.

2.4.2 Implemented Scintillating Grids

The organic scintillator systems evaluated for SPLEBL consist of a host polymer and at least one fluorescent molecule. Many scintillators emit in the near UV, so a secondary scintillator is often added to shift the wavelength into the visible region where photomultiplier efficiency peaks. Sometimes an additional molecule, often naphthalene, is added to assist in non-radiative energy transfer between the host polymer and the primary scintillator.

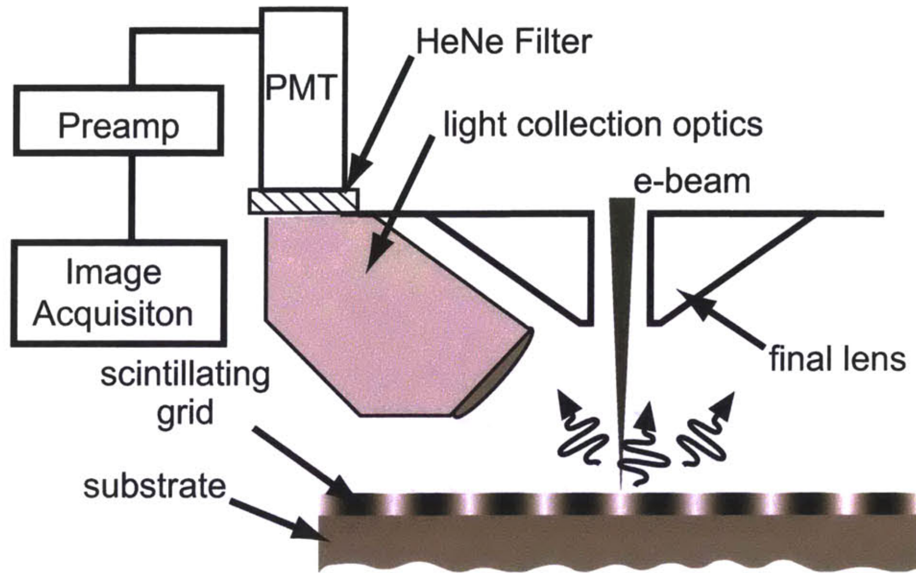

Figure 2.9: A refractive and reflective optical system collects light from the scintillating material in the Raith 150 SEBL system.

This basic scintillator composition has been used in particle detection for a number of years, but Goodberlet et al. developed and tested the first formulation suitable for e-beam lithography. Anthracene, POPOP, and naphthalene were selected for primary scintillator, secondary scintillator, and energy transfer molecules respectively. These components were combined with PMMA in a chlorobenzene solution. The PMMA served as both host polymer and e-beam resist, and the fluorescence could be partially quenched with UV (351 nm) radiation without exposing the PMMA.[30]

This system proved convienient from a processing standpoint, but suffered from several performance limitations. The scintillating components reduced the contrast and sensitivity of the PMMA as an e-beam resist. Secondly, the signal-to-noise ratio of the quenched grids remained insufficient for good spatial-phase locking. Finally, the scintillator was rapidly damaged by the electron beam and by back-scattered electrons. In fact, it is desirable to separate the grid and resist functions so that the best grid can be applied to any resist system. As a result, Finlayson studied several

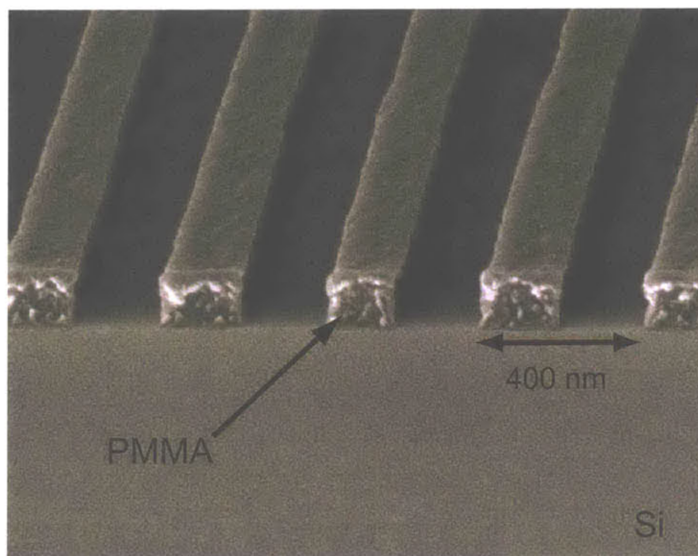

Figure 2.10: Edge view of 400 nm period gratings exposed in PMMA through a the poly-styrene-based scintillator. The scintillator composition and development procedure are detailed in section 2.4.2.

organic scintillators and polymer hosts that might provide better performance.[31]

An immediate improvement resulted from changing the polymer host from PMMA to poly-styrene (PS). This increased the efficiency of the scintillation by 2.3 times, improved the quenching contrast by 1.7 times, and increased the e-beam damage resistance by a factor of 2.3. It was also possible to spin cast the PS based scintillator directly onto pre-baked PMMA, albeit with almost certain mixing at the interface. The PS layer could be stripped and the PMMA developed in a single step with a 1:3 IPA:MiBK solution. Figure 2.10 shows e-beam patterned gratings in PMMA after exposure through the scintillating PS layer and development as above. This process served as a reasonable temporary solution, but the aggressive developer yields lower contrast than standard developers, and the PS-PMMA mixing is also undesirable.

Finlayson also developed an even brighter scintillator using a poly-vinyl toluene host polymer, a para-terphenyl primary scintillator, and POPOP secondary scintillator. This material provided an increase in efficiency of 3.6 and an improvement in e-beam damage resistance of 3.0 over the PMMA-based benchmark. The quenching

Host Polymer	Peak IL Dose (mJ/cm^2)	Modulation	SNR (a^2/σ^2)
PMMA	762	0.31	0.007
PS	254	0.19	0.034
PS	762	0.19	0.019
PVT	597	0.12	0.014
PVT	746	0.13	0.020
PVT	895	0.11	0.014

Table 2.2: Modulation, SNR, dose, and e-beam energy for 1 μm gratings quenched in PVT, PS, and PMMA based scintillating polymers.

contrast for this scintillator was slightly inferior to that of the PMMA- or PS-based materials at 351 nm. However, Finlayson's experiments with this scintillator showed excellent quenching contrast for 220-nm wavelength exposures of 5-μm period gratings. Unfortunately, this wavelength also exposes most e-beam resists, including PMMA, and the quenching resolution limits were not explored.

Finlayson detailed the properties of a number of scintillators when uniformly quenched (no gratings or grids)[31], but we also investigated the most promising materials with IL quenched gratings. We quenched 1-μm period gratings in three of the scintillators using 351-nm wavelength light. The scintillating layers were approximately 400-nm thick and a 10keV e-beam was used to sample the gratings. These measurements were taken as moiré images with sample spacing slightly larger than the period; the scintillator damaged too quickly when densely sampled. Figure 2.11 shows the moiré images and plots the intensities for the PS and PVT scintillators averaged along the x-axis.

To calculate the SNR, we take the Fourier transform of the averaged signal, and find the ratio between the power of the fundamental frequecy, a^2, and the integrated noise power, σ^2. To obtain the SNR for original signal we must divide the averaged signal's SNR by the number of averages per point. Table 2.2 lists the modulation and signal-to-noise ratio measured for PMMA-, PS-, and PVT-based scintillators.

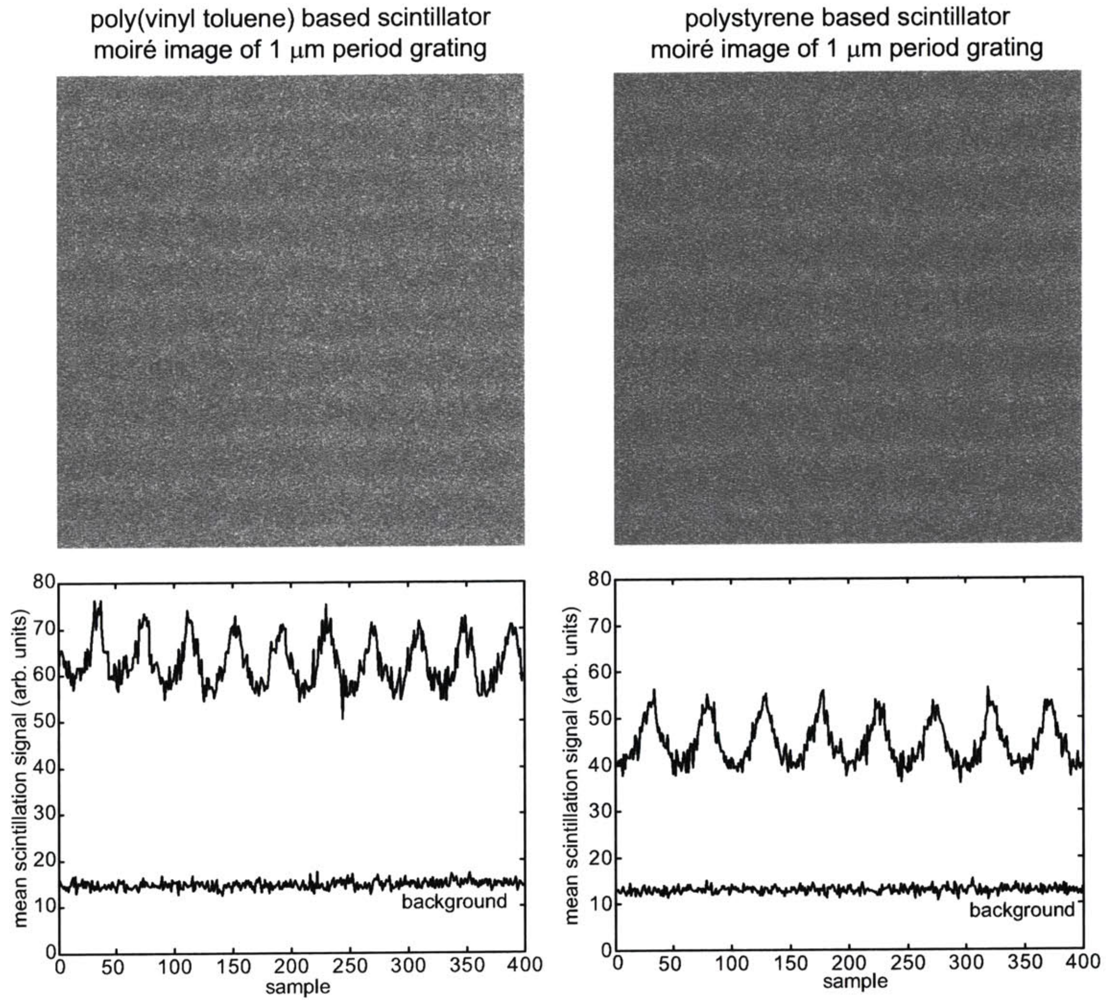

Figure 2.11: Moiré images of IL (351-nm wavelength) quenched 1-μm period gratings in PVT- and PS-based scintillators. There are 400 samples in each axis with an approximate sample spacing of 1.025 μm . The plots below show the row averaged signal from the image, along with the measured background level.

The number of electrons per sample for the data in table 2.2 yields a dose of 70 $\mu C/cm^2$ when using a 6-nm address grid. Even though this is a reasonable dose for PMMA exposed at 10 keV, the SNR will only decrease with denser sampling. In addition, quenching a grid, as opposed to a grating, reduces the SNR further. Thus, the results in table 2.2 represent a nearly best case scenario that is unlikely to be achieved during real-time spatial-phase locking. Even assuming the PS scintillator best case, metallic grids can provide comparable SNR, little e-beam induced damage, at least a factor of five finer period, and no dependence on sampling density; thus, the metallic grid was chosen for real-time spatial-phase locking.

2.4.3 Scintillation Signal Analysis

To fully understand the signal produced by the scintillating grid, and its inability to achieve high resolution, we must examine both the UV quenching and electron sampling processes. As an example, let us consider the brightest organic scintillation system observed in our work. A poly(vinyl toluene) (PVT) host polymer was mixed with a para-terphenyl primary scintillator and a POPOP (1,4-Bis(t-phenyl-2-oxazolyl)benzene) secondary scintillator. The p-terphenyl serves as the primary scintillator, converting the energy of the primary electron into a ≈320-nm wavelength photon. The POPOP serves as a wavelength shifter to convert the 320-nm wavelength photon into a 420-nm wavelength photon near the peak detectivity point of many photomultiplier tubes.

Interference lithography produces a sinusoidal intensity distribution in the exposure plane, and the nonlinear photoresist response transforms this exposure function into a rectangular resist profile. Unfortunately, the scintillator quenching response shows exponential decay with optical exposure dose. As a result, the sinusoidal intensity profile is transformed into a sharply peaked function. The sub-linear quenching response reduces the amplitude of the fundamental frequency component, and thus reduces the contrast and signal-to-noise ratio. The relationship between exposure

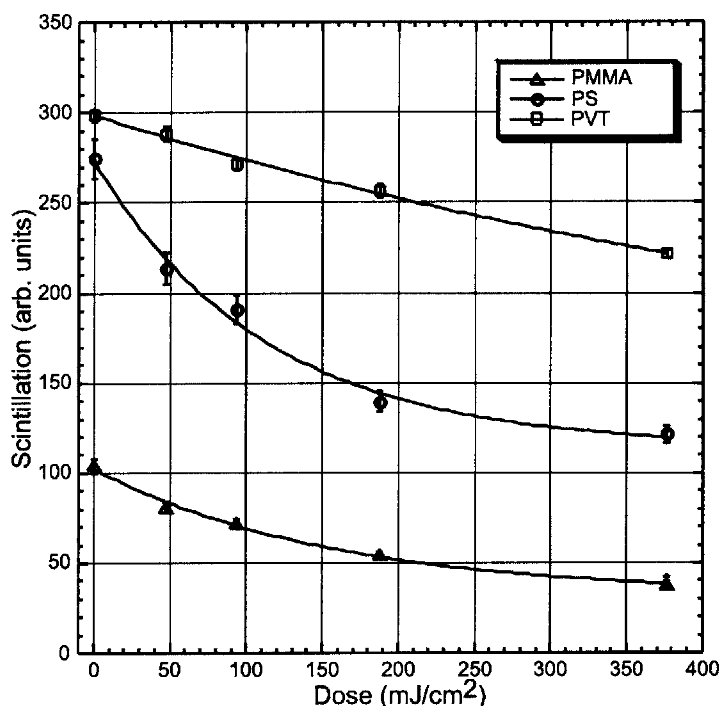

Figure 2.12: Uniform (unpatterned) quenching response for PMMA, PS, and PVT based scintillators when exposed to 351-nm wavelength light. Adapted from [31].

dose and fluorescence is shown in figure 2.12. Finlayson acquired this data with a uniform 351-nm wavelength exposure and 5kV electron beam sampling.

Once the residual fluorescence level is known, one must convolve it with the electron-beam sampling function to determine the observed signal. The electron beam itself is small with respect to the period of the grid, and forward scatting of electrons in the host polymer should not significantly broaden it. On the other hand, the backscatter range of electrons from a silicon substrate is larger than the typical grid period. Approximate backscatter ranges ($1/e$ radius of a Gaussian energy deposition distribution) are 0.65 μm [32], 8.8 μm [33], and 26 μm [34] for 10-kV, 50-kV, and 100-kV electron beams incident on silicon. Because the backscattered electrons deposit approximately the same amount of energy as the primary electrons, the background level will be about one-third of the peak emission intensity, even in the best

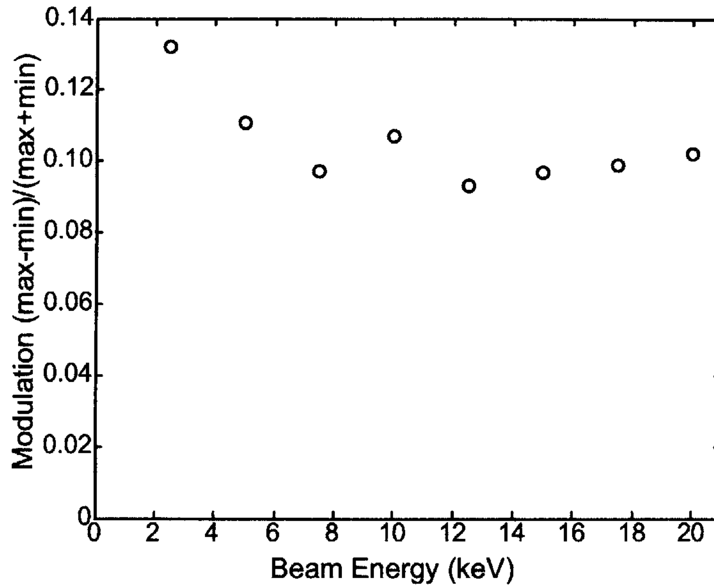

Figure 2.13: Modulation versus beam energy for 1-μm period UV-quenched gratings in the PVT-based scintillator. Although the modulation improves slightly at low energies, there is little variation overall.

case.

Because the backscatter range varies with accelerating voltage one would expect a variation in grating modulation as well. To investigate this effect, we sampled the quenched 1-μm period grating in the PVT-based scintillator with beam energies from 2.5 to 20 keV. Figure 2.13 plots the observed modulation versus beam energy. Although there seems to be some improvement at low voltages where the back scatter range is small; overall, the dependence of modulation on electron energy is weak.

Scintillators using a wavelength shifting molecule also inhibit high-resolution imaging. Finlayson showed that UV light near 351 nm, the wavelength of the IL system, only quenches the secondary scintillator, POPOP. The primary scintillator remains active and is excited by the electron beam. As a result, the optical emission from the primary scintillator, $\lambda \approx 320nm$, can couple to a volume at least as large as the wavelength in the material, and to a potentially much larger area because the polymer film acts as a waveguiding layer between the silicon below and vacuum above.

A series of quenching experiments were carried out with the electron beam to test the resolution of the scintillator. A $\approx$ 400-nm thick layer of the PVT-based scintillator was spin coated on a silicon substrate. A 10 kV electron beam was used to quench gratings of various periods in the scintillator. The electron beam can be expected to quench both the primary and secondary scintillators, so this is nearly the ideal case from this perspective. What is less than ideal is that backscattered electrons, and perhaps high-energy secondaries, also quench the scintillator. As a result a larger area than desired is quenched and sampled at each point. As shown in figure 2.14, the detected modulation of the quenched gratings decreases with increasing spatial-frequency. E-beam quenching represents a compromise between completely quenching both components and undesirable quenching due to backscattered and secondary electrons. While not establishing a lower bound on quenching resolution, these results emphasize the difficulty of using scintillating grids with periods below 1 μm . Once again, scintillators must compete with metallic grids where periods of 200 nm are readily obtainable.

2.5 Phase Estimation of the Fiducial Grid Signal

All implementations of spatial-phase locking naturally depend on detecting the phase of a periodic signal. This is a standard estimation problem that arises in a variety of fields, and phase-estimation methods and their accuracy limits have been well established. The periodic grid signal contains at least a fundamental frequency component and perhaps additional harmonics. The additional harmonics arise because a metallic grid typically approximates a square wave rather than a sinusoidal signal. The displacement of the electron beam can be calculated from the phase of the fundamental component from the expression

$$\Delta x = \Lambda \frac{\phi_x}{2\pi} \tag{2.1}$$

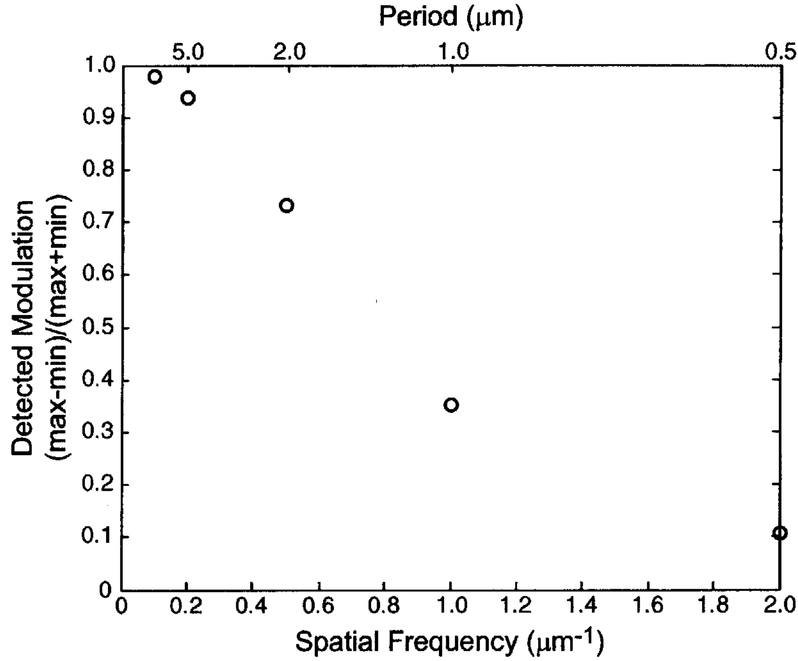

Figure 2.14: Measured modulation of grating quenched and imaged with a 10-keV electron beam.

where Δx is the beam shift along the x-axis, Λ is the grid period, and ϕ_x is the phase shift along the x-axis. The shift along the y-axis is calculated in the same manner. In the continuous feedback mode of spatial-phase locking, described in chapter 5, we rotate the grid with respect to the beam scan direction and the relationship is somewhat more complicated.

Estimating the amplitude, frequency, and phase of a sinusoid in noise is a classic problem treated in several texts. See, for example, references [35, 36]. In this section we pose the problem and provide the key results needed for spatial-phase locking. Consider a sinusoidal signal, s, with amplitude a, angular frequency k, and phase ϕ. To this sinusoid add a normally distributed noise component, ν, with zero mean and σ^2 variance.

$$s(x) = a\cos(kx + \phi) + \nu[0; \sigma^2] \tag{2.2}$$

First, we wish to determine the minimum variance with which one can estimate ϕ. The Cramer-Rao bound establishes the minimum variance with which one can estimate a given parameter based on the information content of the signal. However, the determination of this bound does not guarantee the existence of an algorithm that achieves this performance. If such an algorithm exists, one describes it as an efficient estimator. Wilskey, Wornell, and Shapiro provide a thorough derivation of the Cramer-Rao bound for estimation of the parameters of a sinusoid from discrete samples.[36]. They show that the variance of the phase-estimate, σ_ϕ^2, is given by

$$\sigma_\phi^2 = \frac{(2N-1)}{\gamma N(N+1)} \approx \frac{2}{\gamma N} \tag{2.3}$$

where N is the number of samples of the signal, and the signal-to-noise ratio is given by $\gamma = a^2/\sigma^2$.

The first algorithm one would consider in estimating the parameters of a sampled sinusoid is the discrete-Fourier transform (DFT). For N samples of a signal $s(x)$, we define the DFT as

$$S(k) = \frac{1}{N} \sum_{n=0}^{N-1} e^{-jkx_n} s(x_n) \tag{2.4}$$

where k is the frequency, and x_n is the nth sample location. The DFT is an efficient estimator for a signal's phase, frequency, and amplitude as long as the frequency peak can be distinguished from the noise. If the frequency is known before hand, as in real-time spatial-phase locking, then this requirement is unnecessary.

The phase estimate is extracted from the DFT at the grid's spatial-frequency (k_g) using the real and imaginary parts of $S(k)$.

$$\phi(k_g) = \arctan\left(\frac{\mathrm{Im}\{S(k_g)\}}{\mathrm{Re}\{S(k_g)\}}\right) \tag{2.5}$$

where the inverse tangent is computed in the interval $[-\pi, \pi]$.

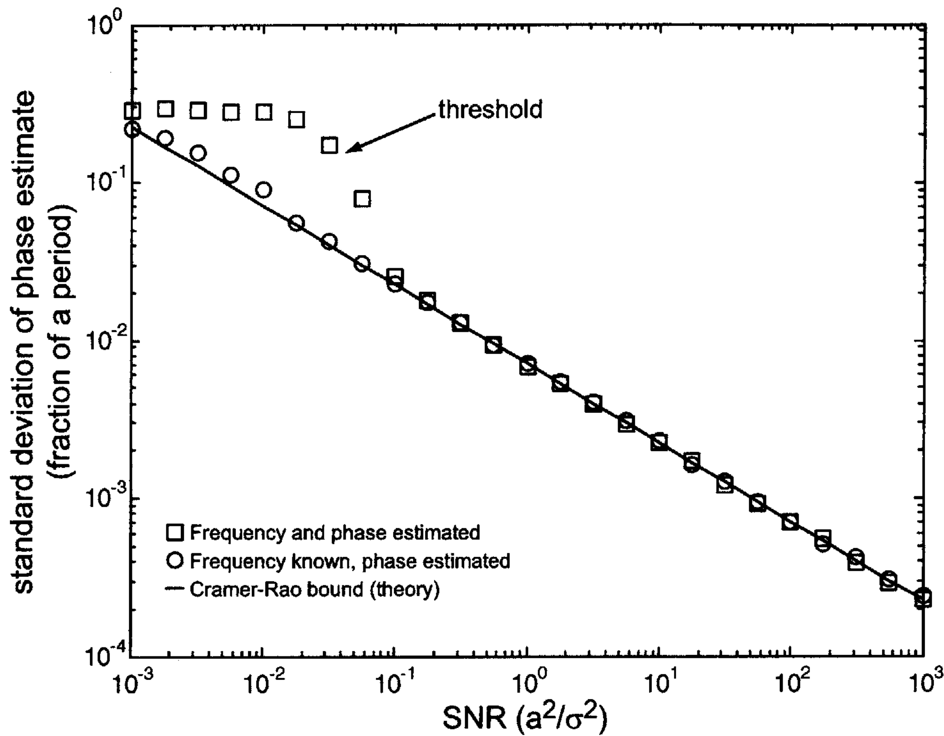

Figure 2.15: Cramer-Rao bound for phase-estimation of a 16-period sinusoid in white noise with 1000 samples. The abscissa shows the signal-to-noise ratio (a^2/σ^2) and the ordinate shows the standard deviation of the phase estimate as a fraction of 2π. Circles indicate the standard deviation of 500 simulated phase-measurements using discrete-Fourier transforms evaluated at the known frequency. Squares represent a similar simulation with simultaneous phase and frequency estimation.

Figure 2.15 plots the Cramer-Rao bound for phase-estimation of a sinusoid (16-periods) in white noise using 1000 samples. Simulations using discrete Fourier transforms to estimate the phase at the known frequency illustrate that the DFT is an efficient estimator under these conditions. Simulations using DFTs to estimate both phase and frequency simultaneously lead to a thresholding behavior. In this case, the DFT becomes an efficient estimator only when the amplitude of the fundamental peak consistently exceeds the noise. Below this threshold, inaccurate estimation of the frequency makes the phase estimate unreliable.

The DFT can be computed at several frequencies using fast-Fourier transform

(FFT) techniques, but for spatial-phase locking one needs to compute the phase at only two frequencies. Although FFT approaches greatly reduce the time required to calculate the amplitude and phase at several frequencies, it is always faster to compute these parameters directly for one or two frequencies.

Equations 2.1, 2.3, 2.5 and figure 2.15 show that one can improve spatial-phase locking precision by increasing the number of samples, improving the signal to noise ratio, or producing finer period grids. The standard deviation of the beam-shift estimate is proportional to $\Lambda/\sqrt{\gamma N}$; thus, decreasing the grid period, Λ, has the greatest effect. For scintillating grids this is often not possible without severely reducing the SNR, but for metallic grids, finer periods present few tradeoffs. In a real-time system increasing the number of samples reduces the bandwidth of the spatial-phase locking system. In "look-then-write" systems increasing the number of samples increases the background dose. This is fine for the segmented grid mode, but may not be acceptable for the sparse-sampling mode. Increasing the number of electrons per sample will also increase the SNR, but when exposing a pattern the dose is fixed by the resist sensitivity and the beam energy. Improving the SNR with better grid materials or detection systems will always be helpful.

Chapter 3

Segmented Fiducial Grid Spatial-Phase Locking

In the segmented grid mode of SPLEBL one isolates the fiducial grid to small unused portions of the substrate. In this way neither the grid itself nor the e-beam sampling of it affects the exposed pattern. By separating the grid from the exposed area, we can use strongly scattering, high-SNR, grids, and we can sample at doses well beyond the exposure dose for the resist. However, the grid still possesses long-range spatial coherence, insuring that the e-beam-exposed pattern exhibits global, as well as local, pattern-placement precision. Figure 3.1 shows the most common segmented-grid configuration with the grid and e-beam sampling windows in the corners of each deflection field.

The segmented fiducial grid is tailored to a vector-scan, "look-then-write," exposure strategy. The stage moves to a new position, the e-beam samples the fiducial grid, the beam deflection is corrected, and the pattern is exposed. This sequence is repeated for each field in the pattern. There is no feedback during pattern exposure, so the system must remain stable during the time required to expose one field. Exposure times for individual fields range from seconds to minutes depending on the SEBL system, the pattern density and resolution, and the resist sensitivity.

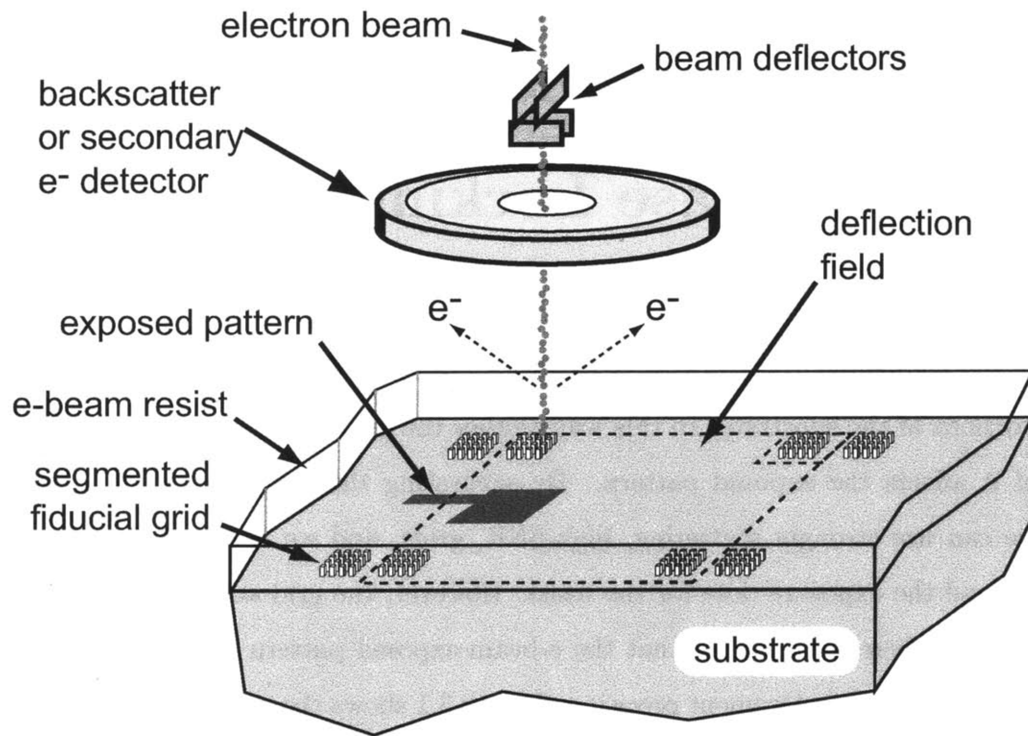

Figure 3.1: In segmented-grid spatial-phase locking, the e-beam scans over the grid in isolated areas. After measuring the spatial-phase in these regions, the beam deflection is corrected, and the pattern is exposed normally.

This approach was jointly developed by MIT and IBM and originally implemented on IBM's VS6 system.[26] Ferrera modified MIT's VS2A system to use the segmented-grid mode of spatial-phase locking. Using an 511 nm-period gold fiducial grating on a x-ray lithography mask (1μm thick SiN membrane), Ferrera obtained field stitching errors with 7.5 nm mean and 6.0 nm standard deviation (after deconvolving the measurement uncertainty). This indicates σ =4.3 nm field-placement precision with respect to the fiducial grid.[23] It is hypothesized that the laser interferometer resolution ($\lambda/128 \approx 5$ nm) limited the placement precision.

3.1 SEBL Field Calibration

In many ways the segmented-grid mode of SPLEBL acts as a sophisticated, field-by-field, calibration routine. Thus, it is important to understand the normal approach to field calibration in the absence of spatial-phase locking. Typically, SEBL systems calibrate the deflection of the electron beam by imaging a feature at various positions in the field. By comparing the observed position of the feature with the expected position, one can adjust the deflection system to match the stage motion.

Measuring the beam-deflection error at several points in the field allows one to correct for a variety of deflection errors. The most simple field-calibration approaches correct for shift, scale, and rotation of each deflection axis. This type of field calibration can be described by a simple set of equations that relate the actual and desired beam locations with a set of six coefficients.

$$x_B = a_0 + a_1 x_P + a_2 y_P \tag{3.1}$$

$$y_B = b_0 + b_1 x_P + b_2 y_P \tag{3.2}$$

where x_B and y_B are the actual beam positions and x_P and y_P are the intended positions from the pattern generator. The coefficients $a_0, a_1,$ and a_2 represent the shift, scale, and rotation errors of the x-axis respectively. Similarly, the coefficients

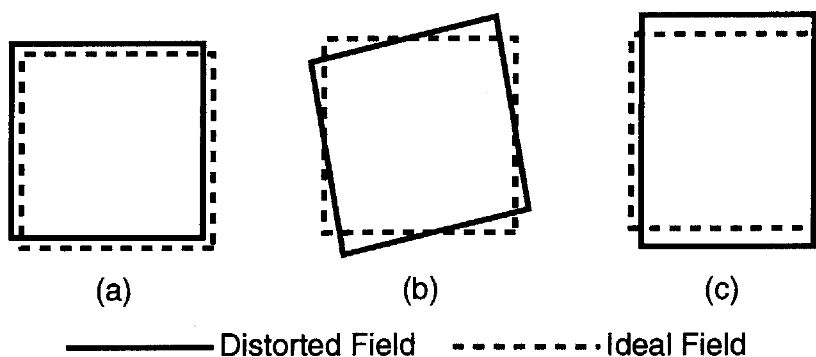

Figure 3.2: Basic field deflection errors. (**a**) Field shift along both axes. (**b**) Rotation and non-orthogonality of axes. (**c**) Scaling errors for both x- and y-axis. The illustrations are greatly exaggerated compared to the errors observed in SEBL systems.

$b_0, b_1,$ and b_2 represent the shift, rotation, and scale errors of the y-axis. Figure 3.2 illustrates these various errors.

By moving the stage to three locations within the deflection field one generates three measurements of x_B and y_B for three known coordinates x_P, y_P. Substituting each of these measurements into equations 3.1 and 3.2 results in a system of three equation and three unknowns ($a_0, a_1,$ and a_2) for the x-axis and a similar set for the y-axis. Once we have solved for these coefficients, one can store them and apply appropriate corrections to each exposed field.

This approach to deflection calibration can be extended to account for higher-order effects such as trapezoidal distortion and non-linearity of the DACs or deflection amplifiers. Ferrera's implementation on VS2A added the trapezoidal distortion term, as does the sparse-sample implementation described in chapter 4. The continuous feedback mode of spatial-phase locking incorporates corrections through third-order (10 coefficients per axis), and will be described in chapter 5.

3.2 Implementation on the Raith 150 SEBL System

3.2.1 The Raith 150 SEBL System

A segmented-grid approach similar to Ferrera's was implemented on MIT's Raith SEBL system. The Raith 150 combines the electron optics from a scanning electron microscope with a vector-scan pattern generator, an electrostatic beam-blanker, and a laser-interferometer-controlled stage. The system uses a thermal-field emission source to produce a beam with high resolution (< 3 nm) and current density at accelerating voltages from 100V to 30kV. Imaging for calibration and alignment is carried out with one of two secondary-electron detectors: an in-chamber Everhart-Thornley detector and an annular in-lens detector.

The Raith 150 pattern generator can increment the beam position in steps as small as 1 nm at rates up to 10 MHz using 16-bit digital-to-analog converters (DACs). The rise and fall times, τ, for the beam blanker are specified as $30\text{ns} < \tau < 50\text{ns}$. Combined with the high-current-density field-emission source, these specifications would seem to indicate good-throughput for a research-oriented system. However, the magnetic deflection system and vector-scan architecture require long-settling times when the beam is deflected to the starting point of each feature. In addition, deflecting the beam at velocities exceeding ≈ 10 mm/sec introduces unacceptable feature size variations. Finally, throughput is limited by the small deflection range ($< 200\ \mu$m for high fidelity patterning) and slow stage-movement (≈ 3 seconds per field). Thus, the throughput of the system is substantially lower than simple calculations would suggest.

The sample-positioning system consists of a roller-bearing stage with 150-mm travel and a piezo-controlled stage for fine-positioning. Raith specifies the laser-interferometer resolution as 2 nm. Many SEBL systems measure the position of the

stage with the laser-interferometer and feedback fine corrections to the beam deflection system. However, the Raith 150 feeds back the stage-motion to the piezo controls of the fine-positioning stage. The Raith strategy exhibits much lower bandwidth than the beam-deflection strategy, but it eliminates errors caused my miscalibration of the deflection system to the stage motion.

3.2.2 Implementation Strategy

The Raith 150 implementation of the segmented-grid mode assumes that the fiducial grid is isolated to small areas occupying several locations in each field. The custom software for spatial-phase locking can accommodate any grid positions the user desires, but it is often natural to place the grid in small squares at the corners of the field. In addition, placing the grid locations as far apart as possible increases the precision of field scale and rotation corrections.

During the segmented-grid-mode exposure, the stage first moves to the center position of the field. Then the electron beam scans over the grid within small windows located near the field corners. The secondary-electron signal from the grid is digitized and stored electronically. The window size is user selectable, and a one-dimensional signal is obtained for each axis by averaging grid signal along the orthogonal direction. For example, a 1D signal for the x-axis is obtained by averaging each element in the columns (y-axis) of the secondary-electron image.

One calculates the grid's spatial-phase for each axis using this 1D signal and the Fourier-techniques described in section 2.5. These phase estimates translate to beam placement errors for each position in the field. In contrast to the typical field calibration approach, we have acquired these error measurements from the fiducial grid, not by moving a feature around with the stage. Measuring the x- and y-displacement in the four corners of the field overdetermines the system of equations for the field-correction coefficients (four equations and three unknowns for each axis). Instead of discarding one measurement, we improve the calibration by finding the least squares

solution for the correction coefficients.

The Raith 150 system's software is proprietary, so the segmented-grid mode of spatial-phase locking was implemented using the software's scripting capabilities. Visual Basic (Microsoft Corporation, Redmond, Wa.) scripting routines control the Raith software, while the mathematical computations are performed by MATLAB (Mathworks, Inc. Natick, Ma.) scripts. The two software programs communicate using Microsoft's ActiveX[1] framework.

The software also provides an automated routine for mapping the stage movement to the grid axes. This is necessary, because the sample cannot be loaded accurately enough to align the stage motion with the grid. Nevertheless, the stage must position the sample within one grid period of the desired location because the grid's phase is ambiguous to 2π. To accomplish this, custom software moves the stage to various locations on the sample over several millimeters and measures the spatial-phase of the grid. In this way one can measure the rotation of the grid with respect to the stage axes, and correct for this each time the stage moves during the exposure.

3.3 Raith 150 Performance with Segmented-Grid SPL

A number of experiments were conducted to measure the performance of the segmented-grid mode of spatial-phase locking on the Raith 150 system. All of these experiments used fiducial gratings, as opposed to grids; as a result, only one-dimensional phase locking was tested. The Bragg-grating-based devices described in chapter 6 require accurate placement primarily along the grating vector, so 1D spatial-phase locking is sufficient.

[1] ActiveX encompasses a range of technologies developed by Microsoft. For our purposes, ActiveX provides a software program access to another program's data and code objects. For example, one can use MATLAB to access the Raith software's **column** object to set the accelerating voltage.

The first set of experiments was conducted using a double exposure technique in poly-methyl methacrylate (PMMA) resist on silicon substrates. Fiducial gratings of 244-nm period, originally produced by interference lithography, were printed with x-ray lithography in a 175 nm thick layer of PMMA. The gratings on the x-ray mask were isolated into stripes approximately 4 μm wide and 1 cm long to leave room for the devices. The patterns were developed in a solution of 2 parts iso-propyl alcohol to 1 part methyl-iso butyl ketone (2:1 IPA:MiBK) for 30 seconds. The substrate, with PMMA still covering most of the area, was loaded into the Raith 150 system. The gratings could be imaged using the in-lens secondary electron detector because of the material contrast between PMMA and silicon, and the resist topography. The x-axis was mapped to the grating vector, and the y-axis was mapped orthogonal to the grating vector (parallel to the grating lines).

Segmented-grid SPLEBL was used to expose gratings of identical pitch, offset by 500 nm in the y-direction from the fiducial gratings. These gratings were written at 14 locations within the field as shown in figure 3.3. This strategy allows us to measure absolute registration between the fiducial gratings and the SPLEBL-exposed gratings at a number of points within the field. As a result, we can observe distortion and exposure-parameter dependent errors within a single field. This diagnostic tool proved critically important.

The grating patterns were exposed using a beam energy of 10kV and a doses from 50 to 70 μC/cm^2. These doses are somewhat low for PMMA at 10kV as a result of the x-ray background dose present. The PMMA was developed for a second time for 60 seconds in 2:1 IPA:MiBK. The samples were once again loaded in the Raith 150 to measure the offset between the SPLEBL exposed gratings and the fiducial gratings. The gratings were imaged over a 8.4 μm x 3.1μm area and the spatial phase of the fiducial gratings was compared to that of the SPLEBL-exposed gratings to determine the registration error. This technique uses the same Fourier techniques as spatial-phase locking and has been described in detail by Ferrera.[23, 26] The relative

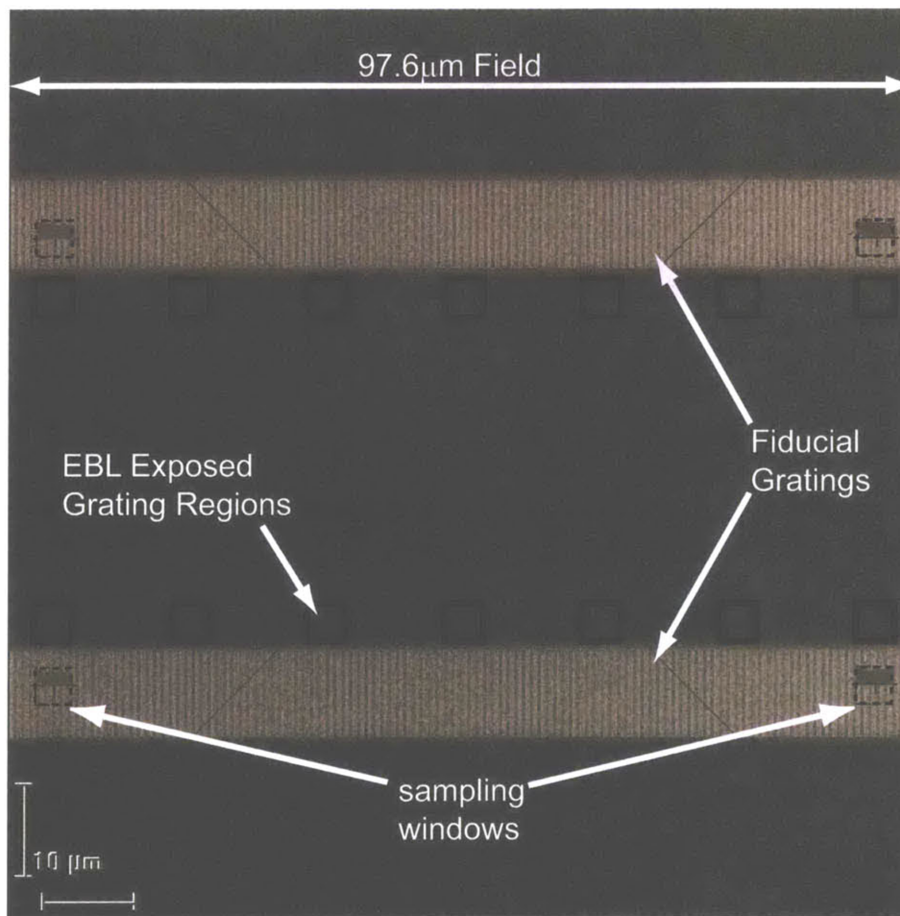

Figure 3.3: 244-nm period fiducial gratings printed in PMMA using x-ray lithography. The sampling windows for segmented grid spatial-phase locking are shown, as are the areas in which identical period grating structures were written with SPLEBL.

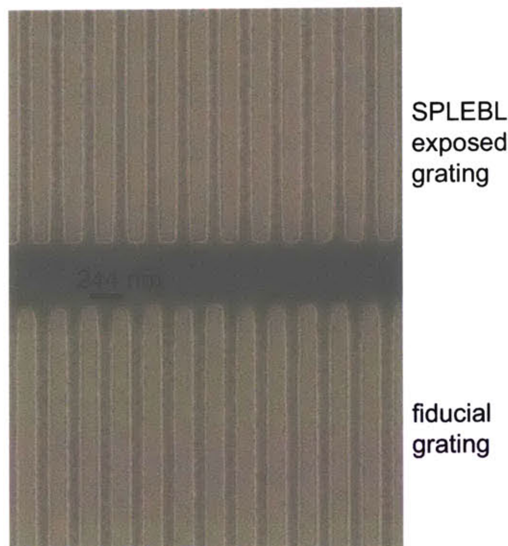

Figure 3.4: Sample image of aligned fiducial grating (top) and SPLEBL written grating (bottom) in PMMA. The π phase shift between the two gratings is intentional.

positions of the two gratings can be measured very precisely because the image is taken with a large dose and in a region of the field known to be distortion free. Figure 3.4 shows the x-ray and EBL exposed gratings in PMMA.

These experiments generated an enormous amount of data because the registration between the fiducial grating and the SPLEBL exposed gratings was measured at 10 or 14 positions in each of 50 fields. Here the results of only two such experiments are shown in detail, but the results from 20 experiments are summarized. Three key points emerge from this data. First, significant non-linear distortions remain after correcting scale, rotation, and shift errors. Second, the beam-deflection velocity in the y-direction influences pattern placement in the x-direction in a repeatable way. Finally, the registration varies from field-to-field with a standard deviation of ≈ 3 nm for all tested exposure conditions. To summarize further, the mean registration errors vary because of field distortion and exposure-dependent errors, but the variance of the errors within an exposure is consistently small.

Let us first examine the mean registration errors at each point in the field under

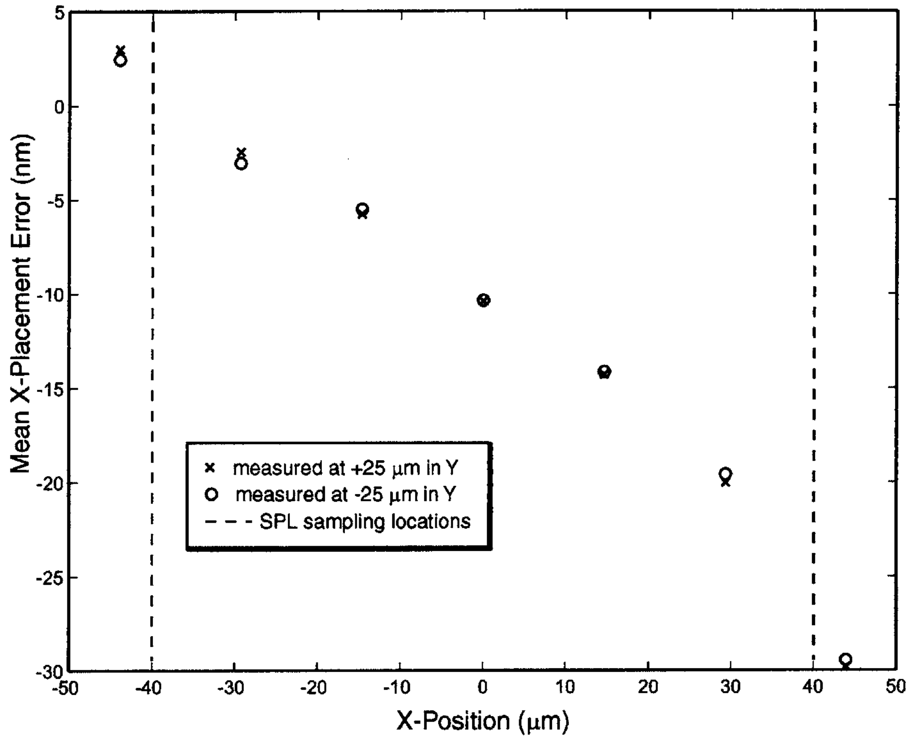

Figure 3.5: Mean x-alignment error versus x-position in scan field for vertical grating lines written with a deflection velocity of 25 mm/sec. Examining the error at the spatial-phase locking locations leads to a field scaling error of -3.1×10^{-4}. Alignment was measured with respect to the upper and lower fiducial gratings at ± 25 μm . Dashed lines represent spatial-phase locking locations.

two different exposure conditions. In both exposures the gratings were written by sweeping the beam from the bottom to the top of each line, not by boustrophedonic filling. The beam velocity was 25 mm/sec and the gratings were sampled at $\pm 40\mu$m in x and $\pm 25\mu$m in y. Figure 3.5 plots the mean offset between the fiducial and SPLEBL exposed grating versus the x-position in the field. The two data series represent registration to the top and bottom gratings. In this case, it is clear that the mean error changes somewhat linearly across the deflection field with significant non-linearities at the edges of the x-deflection range.

In figure 3.6 the data is plotted for a similar exposure where the beam velocity was reduced to 9 mm/sec. In this exposure, the difference between the phase-locking

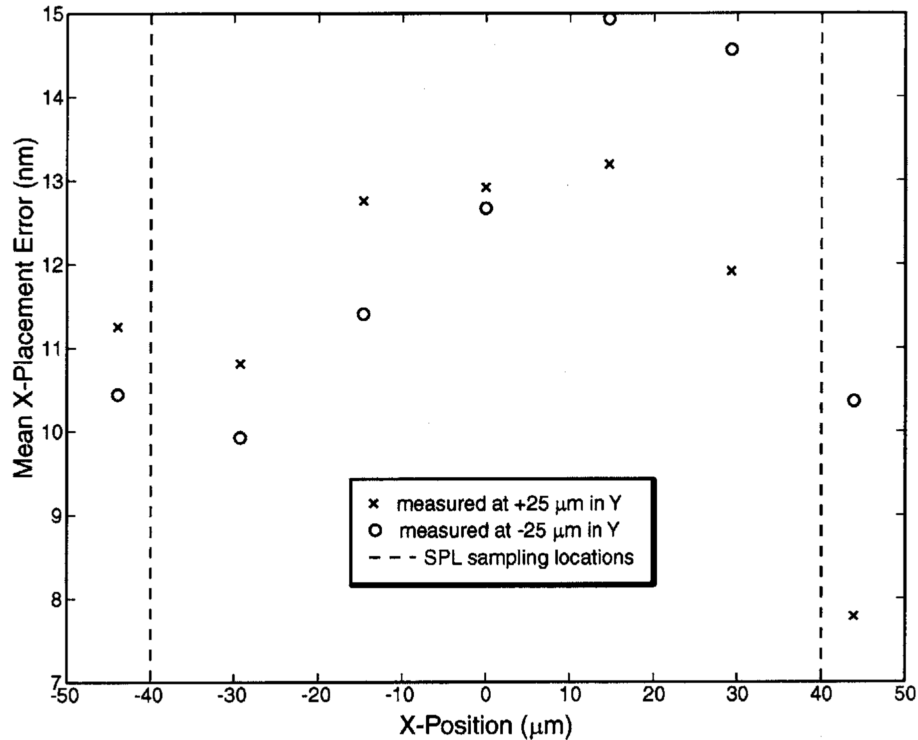

Figure 3.6: Mean x-alignment error versus x-position in scan field for vertical grating lines written with a deflection velocity of 9 mm/sec. Examining the error at the spatial-phase locking locations leads to a field scaling error of -1.1×10^{-5}. Alignment was measured with respect to the upper and lower fiducial gratings at ± 25 μm . Dashed lines represent spatial-phase locking locations.

positions is below 2 nm; although, we still observe the non-linear errors, now shifted to the interior of the field. If we take the grating sampling points as our references, we find that the fast exposure scale error is -3.1×10^{-4} and the slow exposure scale error is -1.1×10^{-5}. Conducting a number of these experiments, shown in figure 3.7, revealed that the scaling error changes linearly with beam velocity.

Naturally, one wishes to correct this error, and with such a simple relationship between scale error and beam velocity, this is practical. Two experiments were conducted at different deflection velocities, and a scale correction was applied to every field. The scaling error was reduced to less than 3×10^{-5} for the scale-corrected exposures. These corrected exposures are also shown in figure 3.7. Simply scaling the field

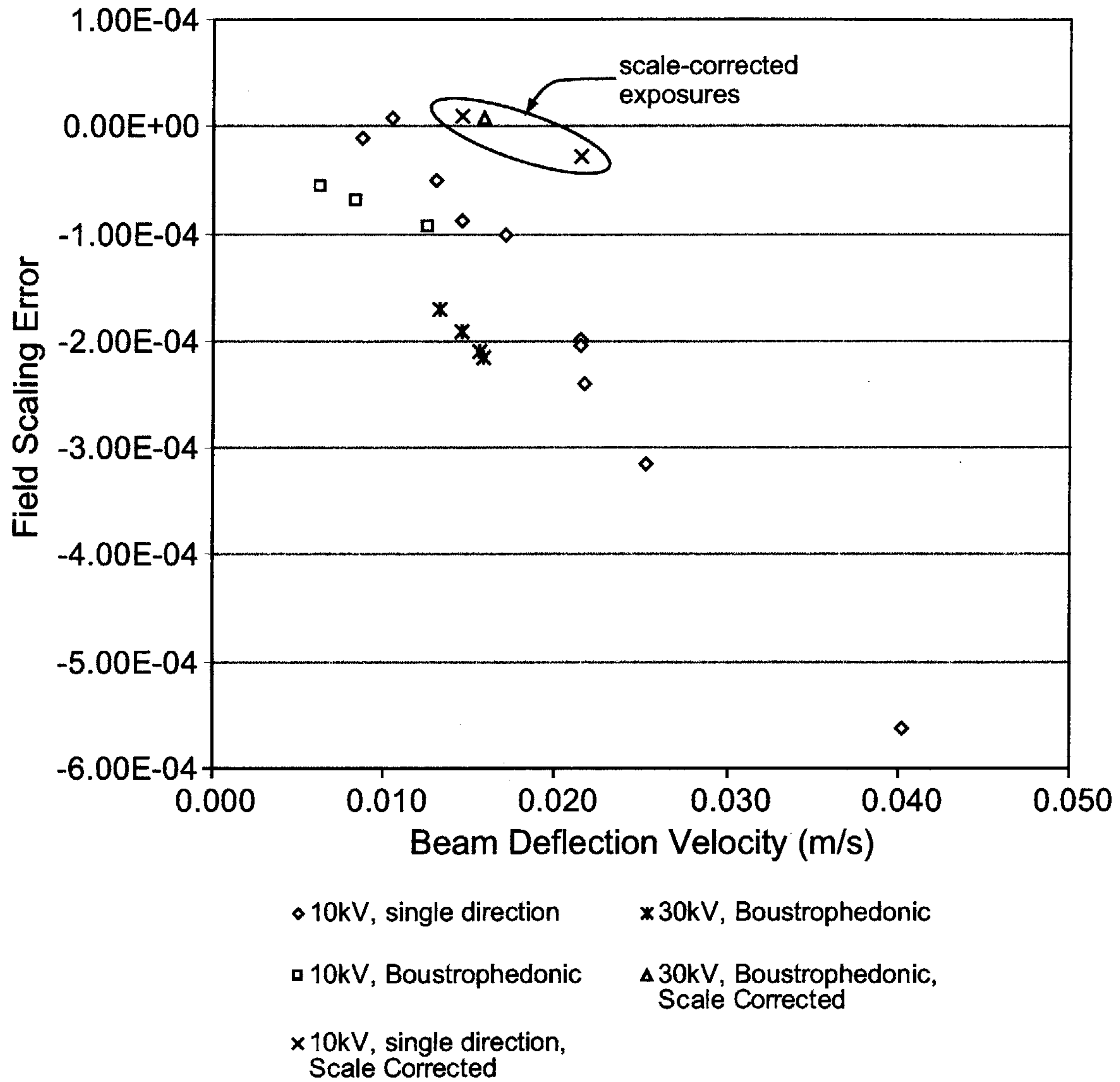

Figure 3.7: Field scaling error versus beam velocity for 10 and 30 kV exposures conducted with single-direction and boustrophedonic filling.

does not remove the non-linear deflection errors, but if one chooses sampling positions between -50 μm and +30 μm non-linear errors can be kept below 2 nm. We adopted this approach for the optical devices described in chapter 6. Also interesting is that the mean error at $x = 0\mu m$ is not necessarily zero for these exposures, indicating a mean shift with respect the fiducial grating. This shift seems to arise from a deflection velocity dependent error when scanning the fiducials themselves. The measured shift of the fiducial gratings is dependent on the velocity at which they are scanned.

In addition to direct registration exposures, a number of field stitching experiments were carried out. By vertically centering the stitched gratings at the same x-locations as the grating sample points, one can estimate the field scaling error from a single measurement. These experiments were conducted at both 10kV and 30kV with boustrophedonic filling, as opposed to single-direction filling. Comparing various experiments in figure 3.7, we observe a consistent linear relationship between beam velocity and scale errors, but slopes and intercepts depend on accelerating voltage and exposure strategy. We acquired the data in figure 3.7 over several months, so it appears that this error is stable with time, and can be corrected empirically.

While mean errors are important, we also need to examine pattern-placement variance. Figure 3.8 shows registration-error histograms for each measurement point in figure 3.6. The standard deviations for each point range from a low of 2.2 nm to a high of 3.4 nm for this experiment. A standard deviation between 2 and 3 nm is typical of all the experiments conducted. It is also interesting that the standard deviation does not increase as one moves toward the edges of the field. This suggests that correction for scaling fluctuations does not contribute significantly to placement error. Repeated stitching measurements of a pair of PMMA on silicon gratings varied with $\sigma = 0.5$ nm.

Although deflection-velocity dependent scaling errors are repeatable and predicatable for a given pattern, their cause remains unknown. Why does rapid deflection along the y-axis change the x-axis deflection symmetrically, and linearly, about the

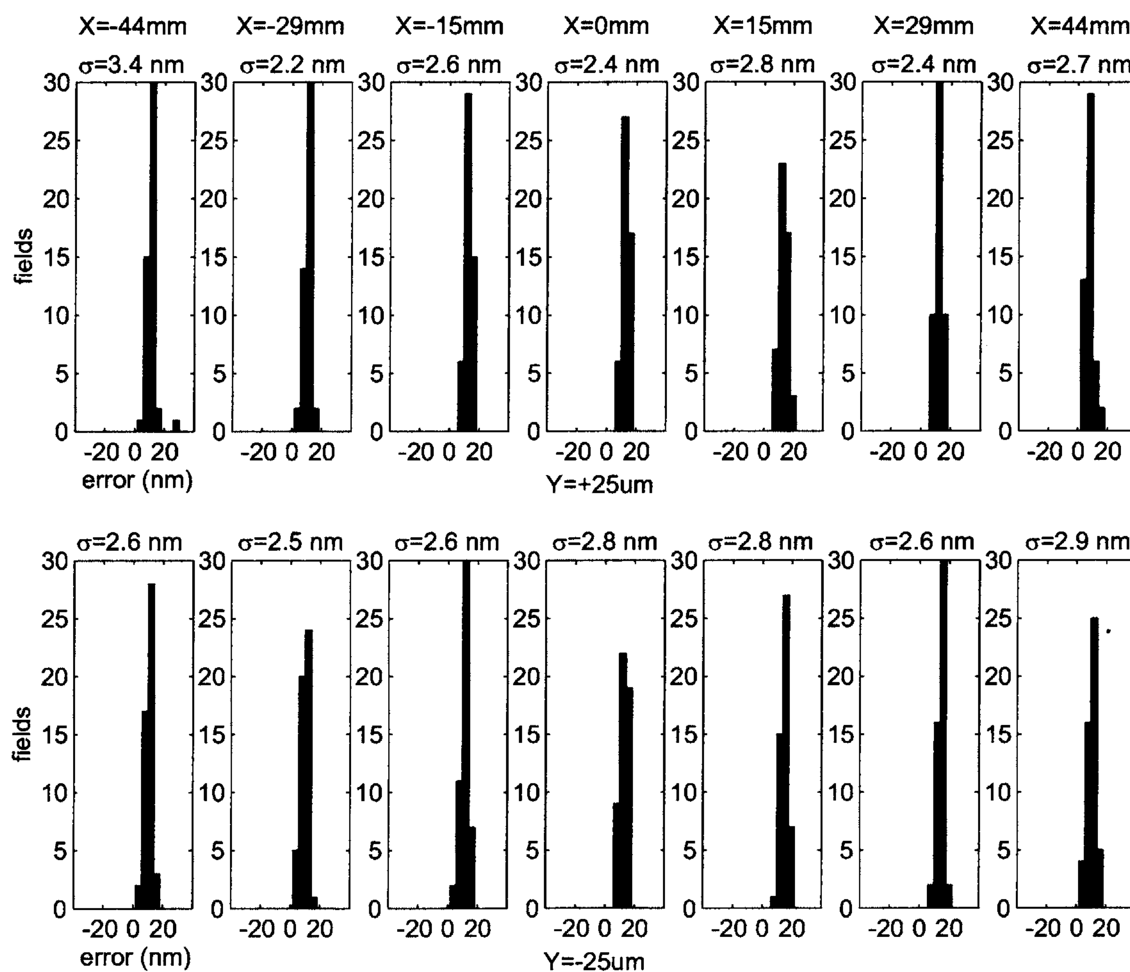

Figure 3.8: Segmented grid SPLEBL placement error histograms for each measurement location shown in figure 3.6.

field center? One might expect slight capacitive or inductive coupling between the magnetic deflectors, their amplifiers, and the interconnected wiring, but it is difficult to ascertain why the magnitude of the deflection error is proportional to the absolute deflection. One potential cause, though highly speculative, is dynamic loading of the deflection amplifier power supply. A rapid deflection back and forth along the y-axis looks like a triangle wave pattern, and the frequency is often hundreds of kilohertz. If this dynamic deflection loads the power supply such that it cannot provide sufficient current to the orthogonal deflector this would introduce scaling errors. If this loading increases linearly with deflection velocity (y-deflection frequency) then we would observe the results of figure 3.7.

Chapter 6 describes the fabrication of Bragg-grating-based optical devices using segmented-grid SPLEBL. Exposures in this process were conducted at 30 kV with boustrophedonic filling, and beam-velocity-dependent scale correction. The mean and standard deviation of the stitching errors along the x-axis (centered vertically in y) were -0.6 nm and 2.6 nm respectively. The 2.6 nm includes the measurement error associated with the system.

Chapter 4

SPLEBL via Sparse Sampling

In the sparse-sampling mode of SPLEBL a global-fiducial grid is sampled at discrete locations within the e-beam field with a sub-exposure dose. Like the segmented-grid mode, beam positioning feedback is only supplied before exposing each field. Unlike the segmented grid mode, the sparse-sampling mode uses a global grid that does not occupy valuable substrate area. This chapter addresses techniques for sampling the grid and extracting field-correction parameters from the resulting signal. These techniques were implemented on MIT's VS2A SEBL system, and tested with both metallic and scintillating fiducial grids.

4.1 Sparse Sampling Strategy

When performing spatial-phase locking via sparse sampling one must first move the substrate to a position within one grid period of the desired location. For laser-interferometer controlled stages and grid periods greater than 100 nm this presents no problem. Because the beam positioning is corrected for each deflection field, one need only move the stage with this accuracy relative to its previous position. Thus, the system can drift beyond one grid period as long as this drift does not occur during the exposure of one field. Of course, because feedback is supplied only at

the beginning of each field, the system must remain stable with the desired accuracy during the time required to expose the field.

After properly positioning the sample, the electron beam acquires a two-dimensional array of samples. In order to determine the grid position without exposing the e-beam resist, these samples are spaced much further apart than the beam diameter. Even if the samples themselves are taken with the same beam current and dwell time used to expose the pattern, they do not receive enough dose to transfer when the resist is developed. While the sampling grid is perfectly generated by the digital pattern generator, the beam does not follow a perfect grid on the substrate. Thus, errors in the beam positioning during sparse sampling appear as shifts or distortions in the fiducial grid image.

In practice, sparse samples are taken at spacings larger than the grid period. Because the spatial frequency of the fiducial grid is greater than the spatial frequency of the sparse samples, the acquired signal will be aliased. In the spatial domain, aliased periodic signals appear as moiré patterns. Figure 4.1 shows the moiré pattern formed by sampling a 1μm-period gold grid at 512x512 equally spaced points within a 528μm field. The number of periods in the moiré is simply given by the difference between the number of sample points and the number of fiducial grid periods in a given direction, in this case exactly 16 periods in both X and Y. Higher-order aliasing produces a similar effect, i.e. 512x512 samples of 1040x1040 periods will also yield a 16x16 period moiré pattern.

4.2 Determination of Deflection Errors from Moiré Patterns

Moiré patterns provide a sensitive tool for measuring deflection-field alignment and distortion. The spatial phase of the moiré signal represents the spatial phase of the periodic sample locations with respect to the underlying fiducial grid. Thus, the

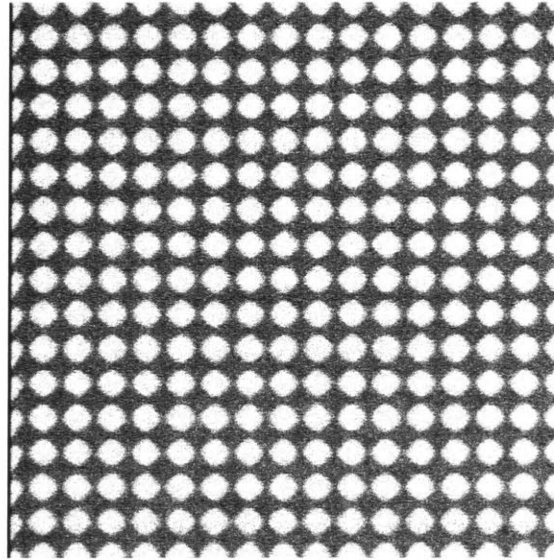

Figure 4.1: Moiré pattern formed by a 512×512 sample array of a 1-μm period grid over a 528 μm field. Image was acquired using backscattered electrons from a Au grid on silicon.

deflection field can be shifted into alignment with the fiducial grid by locking the spatial phase of the moiré pattern to a specified value. Moiré patterns also reveal deflection distortions. Variation of the moiré phase with position in X or Y indicates a rotation, or skew, of the deflection field with respect to the grid. If this variation differs between X and Y the deflection axes are not orthogonal. The spatial frequency of the moiré pattern allows one to precisely calculate the scale (magnification) of the field. Finally, a linear variation of X-spatial frequency with Y, or vice-verse, indicates the presence of trapezoidal distortion. Moiré techniques were addressed in early work on e-beam metrology and spatial-phase locking[37, 26, 38, 39]; however, the mathematical approaches for extracting field distortions were not described.

The VS2A SEBL system uses eight parameters to model and correct the error between desired beam position (x_P, y_P) and actual beam position (x_B, y_B). This correction is similar to the one described in section 3.1, except it adds two additional

terms to characterize trapezoidal distortion. These relationships are given by

$$x_B = a_0 + a_1 x_P + a_2 y_P + a_3 x_P y_P \tag{4.1}$$

$$y_B = b_0 + b_1 x_P + b_2 y_P + a_3 x_P y_P \tag{4.2}$$

where the coefficients $a_0, a_1, a_2, \text{and} a_3$ represent the shift, scale, rotation (skew), and trapezoidal distortion errors for the x-axis, respectively.

To determine the relationship between these errors and the observed moiré pattern, we begin by approximating the fiducial-grid signal as a sum of two orthogonal sinusoidal gratings. I_{grid} represents the signal level regardless of the signal type (backscattered electron, secondary electron, or photon),

$$I_{grid} \approx a\ \cos(\frac{2\pi}{\Lambda_G} x_B) + a\ \cos(\frac{2\pi}{\Lambda_G} y_B) + c + \nu, \tag{4.3}$$

where a is the amplitude, c is the background level, and Λ_G is the spatial period of each grid, typically 200nm to 1μm. ν is a simplified noise term having a Gaussian distribution with variance σ^2. The noise term approximates the electron-arrival statistics, scintillator-photon emission statistics, photomultiplier-tube noise, other electronic noise, and stray light in the vacuum chamber. The signal-to-noise ratio is defined as a^2/σ^2. Neglecting the noise term and substituting equations 4.1 and 4.2 into equation 4.3 for x_B and y_B, we find a function describing the appearance of the fiducial grid within a misaligned or distorted field. Figure 4.2 shows moiré patterns based on equation 4.3 for various field calibration errors.

If we take the Fourier transform of equation 4.3 with respect to x_P at arbitrary y_P, we find that the spatial phase and frequency of the fundamental Fourier component

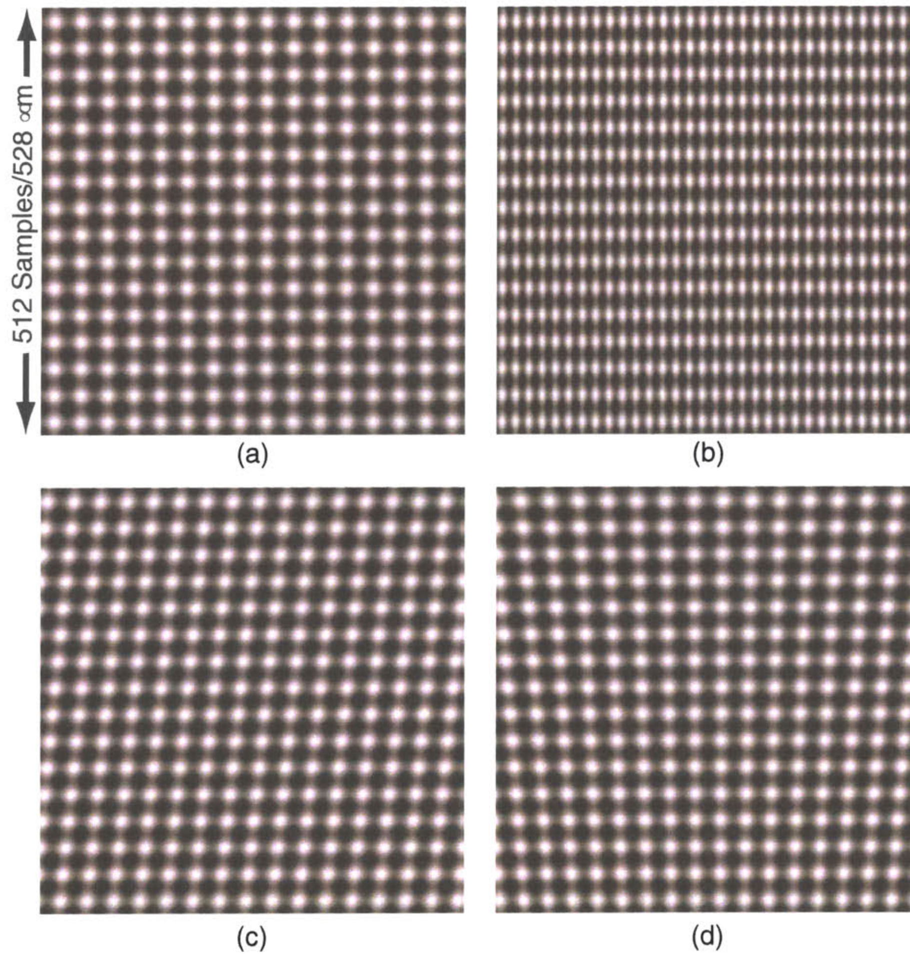

Figure 4.2: Moiré patterns formed by a 512×512 samples of 1-μm period grid over a 528 μm field with various deflection errors. (a) Perfect deflection. (b) X-deflection scaled: $a_1 = 1.03$. (c) X-deflection skewed: $a_2 = 0.003$ radians. (d) Trapezoidal distortion along the y-direction: $a_3 = 1 \times 10^{-5}$.

are given by

$$\phi_x = \frac{2\pi}{\Lambda_G}(a_0 + a_2 y_P) \tag{4.4}$$

$$k_x = \frac{2\pi}{\Lambda_G}(a_1 + a_3 y_P) \tag{4.5}$$

We see that both phase and frequency are linear functions of y_P, with slopes $2\pi a_2/\Lambda_G$ and a_3/Λ_G, and intercepts $2\pi a_0/\Lambda_G$ and a_1/Λ_G, respectively. When under-sampling the fiducial grid, the phase of the moiré pattern along an axis, ϕ_{xm}, remains identical to that of the fiducial grid, but aliasing must be taken into account for the moiré frequency, k_{xm}. Therefore,

$$\phi_{xm} = \frac{2\pi}{\Lambda_G}(a_0 + a_2 y_P) \tag{4.6}$$

$$k_{xm} = 2\pi \left| \frac{1}{\Lambda_G}(a_1 + a_3 y_P) - \frac{1}{\Lambda_S} \right| \tag{4.7}$$

where Λ_S is the mathematically-defined spatial period of the sparse samples.

After acquiring the moiré pattern with an array of discrete samples, we estimate its phase and frequency with respect to x at several y positions. This is accomplished using one-dimensional discrete Fourier transforms (DFT) and a simple peak-search routine for each row of data. Because the moiré spatial frequency is approximately known before beginning the analysis, one need only compute the amplitude at a few frequencies to estimate the peak position with high precision. This proves more computationally efficient than a large zero-padded fast-Fourier transform. After performing linear least-square fits of the phase and frequency versus y_P, the field corrections are given by

$$a_o = \frac{\Lambda_G}{2\pi}\phi_{xm}\Big|_{(y_P=0)} \tag{4.8}$$

$$a_1 = \Lambda_G(\frac{k_{xm}}{2\pi}\Big|_{y_P=0} + \frac{1}{\Lambda_S}) \tag{4.9}$$

$$a_2 = \frac{\Lambda_G}{2\pi}\frac{d\phi_{xm}}{dy_P} \tag{4.10}$$

$$a_3 = \frac{\Lambda_G}{2\pi}\frac{dk_{xm}}{dy_P} \tag{4.11}$$

The corresponding field corrections for the y-deflection are found by taking the Fourier transform of equation 4.3 with respect to y_B and proceeding in the same manner.

4.3 Sparse-sampling Algorithm

The mathematical description in the previous section relates phase and frequency changes in the moiré pattern to deflection errors; however, implementing these calculations requires attention to several details. First, signal-detection efficiency variations across the field lead to non-uniform intensity moiré patterns. These variations add low-spatial-frequency spectral components that introduce bias in the error estimates described above. To reduce this effect we least-squares fit a two-dimensional polynomial to the signal level across the field before beginning the exposure. When each field is sampled the signal is divided by this detection efficiency function to reduce the bias errors.

Second, if the grid is not well-described by equation 4.3 steps must be taken to ensure that the phase and frequency analysis remains valid. Specifically, when using a metallic grid the signal resembles a square wave, not a sum of two sinusoids. The higher-spatial frequencies components generally do not present a problem because we estimate the phase and frequency of the fundamental peak, but a metallic grid does introduce rows and columns of data with little or no modulation. As a results, one

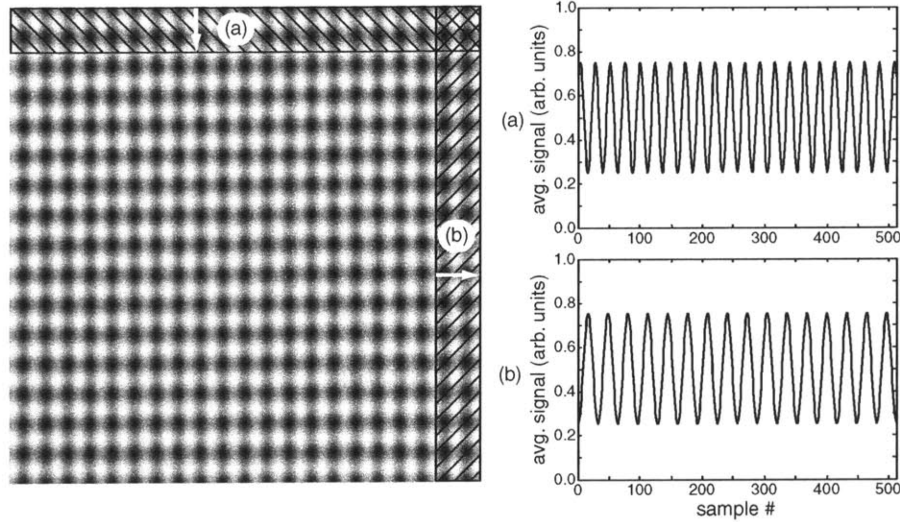

Figure 4.3: Blocks of the moiré pattern are row or column averaged to produce several one-dimensional signals for phase and frequency estimation. The moiré pattern represents a field with a x-scaling error. **(a)** shows the column averaged signal from the top-most block. **(b)** shows the row-averaged signal from the right-most block. One can readily see the different spatial frequencies.

does not want to rely on the phase of a row of samples if they lie between dots or on a single line of a lattice. To alleviate this concern, we average samples over at least one period orthogonal to direction of interest. Figure 4.3 illustrates this procedure.

Similarly, if the signal acquired from the fiducial grid has a low SNR, a single row or column of sample points may not reach the SNR threshold level (see section 2.5) for accurate spectral peak identification. In this case averaging several rows increases the SNR before performing the discrete Fourier transforms. In practice, one only wishes to average enough samples to accurately identify the fundamental peak. The more samples are averaged before performing the phase and frequency estimates the less spatial-resolution one has to determine the derivatives of phase and frequency. The parameter estimation variance does not change whether the raw data are averaged or the resulting phase and frequency estimates are averaged. Finally, the averaged data can be multiplied by a Hann (squared cosine) window before taking the Fourier transform. Windowing the data reduces bias from any residual low frequency

components at the expense of phase- and frequency-estimation precision.

For implementation in VS2A, the sampling periodicity is chosen to produce a 512×512 sample array of an 16×16 period moiré pattern covering the entire field. This pattern is broken into 8 vertical and horizontal stripes whose respective rows and columns are averaged to produce 8 one-dimensional signals for each axis. Several DFTs are performed near the expected fundamental frequency to precisely estimate the peak location for each block of data. After obtaining parameter estimates for each block, we perform a linear least-squares fit to the phase and frequency as a function of position. The phase and frequency intercepts, equations 4.8 and 4.9 provide the shift (a_0, b_0) and scale (a_1, b_2) errors respectively. The phase and frequency slopes, equations 4.10 and 4.11, yield the rotation (a_2, b_1) and trapezoidal (a_3, b_3) errors.

One concern about all "look-then-write" techniques is that field distortion will differ between sampling and exposure. This is the case in the segmented grid implementation on the Raith 150 system, and it is also the case with sparse-sampling on VS2A. The sparse samples are acquired in a raster fashion from left-to-right only, and the beam must "fly back" between each line of samples. This rapid deflection across the entire field introduces errors in both the x- and y-beam position at the beginning of the next line of samples. This distortion is seen in the moiré pattern in figure 4.1. As a result, we do not use the samples from the left-most period of the moiré pattern to calculate deflection corrections.

4.4 Sparse-sample spatial-phase locking with VS2A

4.4.1 Algorithm Implementation

MIT's VS2A SEBL system uses a thermionic LaB_6 emitter, 50 keV beam energy, and high-demagnification electron-optics to pattern at resolutions slightly below 100 nm over deflection fields up to 1 mm^2. Since the time of the experiments described here VS2A's electron optics have been upgraded to achieve sub-50 nm resolution with a

slight sacrifice in field size.[40]. The pattern generator uses 14-bit digital-to-analog converters (DACs), providing a minimum address grid of the field size divided by 2^{14}. The system is equipped with a solid-state backscattered electron (BSE) detector and with optical detection as described in section 2.4.

To control pattern-placement the system measures the stage position with a laser-interferometer (resolution $= \lambda/128 \approx 5$nm) and continuously corrects the beam position to track the stage. This arrangement allows acceptable field stitching and pattern-placement for some applications, but does not constitute true closed-loop feedback control, because the beam position is not measured. Goodberlet and Ferrera measured the field stitching precision of VS2A to be $\sigma = 23$ nm when field were written consecutively, but when each field exposure was separated by 10 minutes, the stitching-error standard deviation increased to $\sigma = 127$ nm.[23, 41] This long-term instability is easily corrected with spatial-phase locking, but can only be compensated in a normal EBL system by frequent reference to a fiducial mark on the substrate or stage.

To perform sparse-sample spatial-phase locking the DT2851 image acquisition board captures the fiducial-grid signal from the PMT or BSE detector. We wrote custom software for an Alacron AL860MP dual-i860 microprocessor board (Alacron, Inc., Nashua, NH) to perform the signal processing described in section 4.3. To test the algorithm we repeatedly locked to 1-μm period gold (high SNR) and chromium (low SNR) grids. VS2A allows continuous control of the beam current, so the SNR, γ, can be varied continuously as well.

Figure 4.4 shows the standard deviation of 100 measurements for each field-correction parameter. The field size was 528 μm $\times$ 528 μm , and the field was corrected after each measurement. The variance, σ^2, of the field correction parameters was found to decrease as $\gamma^{-1\pm0.06}$. The γ^{-1} dependence is expected from the analysis of section 2.5; therefore, it seems the field correction parameters estimates are SNR limited with this large period grid. However, the field shift uncertainty

reaches a minimum near $\sigma = 2$ nm. In this regime, the shift correction is limited by system instability, most likely the laser interferometer's 5-nm resolution and the field-correction unit's 4-nm resolution.

4.4.2 Field-stitching Experiments

To test the effectiveness of sparse-sample spatial-phase locking, field-stitching experiments were carried out in the VS2A system with a scintillating fiducial grid. Silicon wafers were coated with 400 nm of the PMMA-based scintillating resist described in section 2.4. Orthogonal 530-nm period gratings were quenched using 351-nm wavelength light from an Ar-ion laser in the interference lithography system described in section 2.1. Figure 4.5 shows a 16x16 moiré pattern obtained from a 530nm-period scintillating fiducial grid, sampled over a 279.840 μm field.

The signal-to-noise ratio was $\approx$0.004 for the scintillating grid; this was too low to permit accurate rotation, scaling, and trapezoidal correction for each field. Trapezoidal distortion was corrected using a traditional field-calibration routine, and rotation and scale were fixed to their initial values after applying the sparse-sampling routine to one deflection field. Shift correction was enabled for all fields.

To test stitching and pattern placement, we exposed an array of fields with 400nm-period gratings at the field boundaries. An intentional gap was left between the gratings so that the field boundary could be easily identified. The grid was sparsely-sampled for 1 μs per point with a beam current of 300 pA. We developed the scintillating PMMA in 2:1 IPA:MiBK at 21.0° C for 90 seconds. The gratings were transferred to the substrate by evaporating 50 Å of chromium and 600 Å of gold, and then removing the PMMA in n-methyl pyrrollidone heated to 80° C. This "lift-off" process leaves Cr-Au gratings behind on the silicon substrate. Figure 4.6 shows a backscattered electron image of the stitched gratings.

Backscattered electron images of the gratings were analyzed using a technique developed by Ferrera et al.[26, 23] to determine stitching errors. The method com-

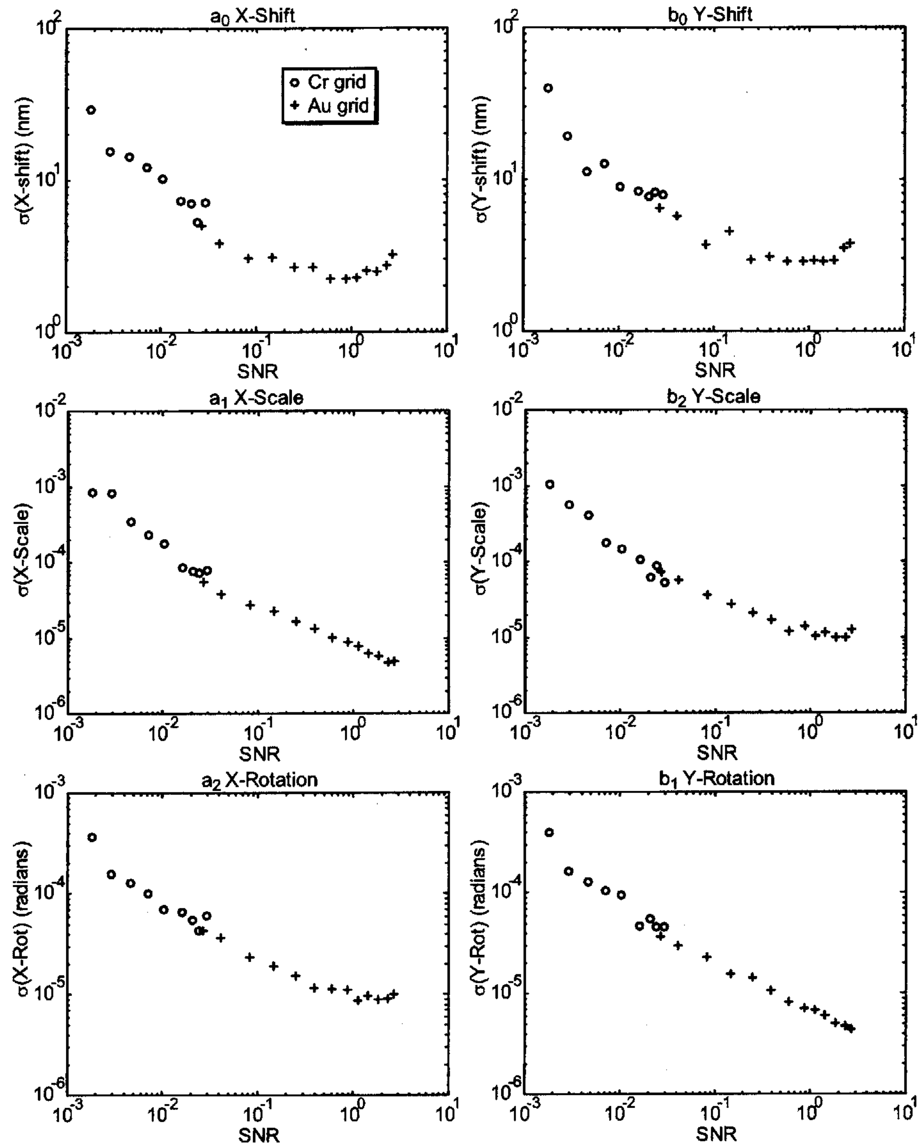

Figure 4.4: Standard deviation of the field-correction parameters versus signal-to-noise ratio for sparse sampling. Each point represents 100 measurements using 512 × 512 samples of a 528 μm field with a 1-μm period fiducial grid.

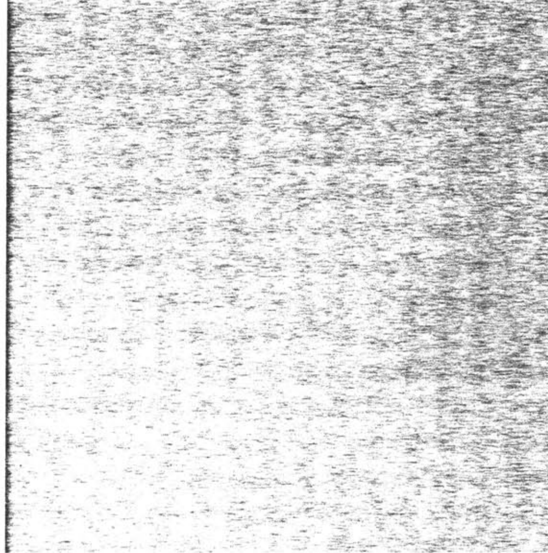

Figure 4.5: Moiré patterned formed by 512 × 512 samples of a 530-μm scintillating grid over a 280 μm field. The scintillating layer (PMMA, anthracene, naphthalene, and POPOP) served as a the e-beam resist and the fiducial grid.

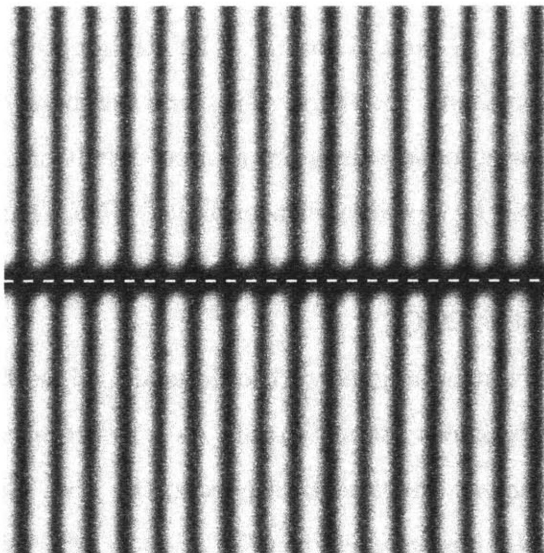

Figure 4.6: Stitched 400-nm period Cr/Au gratings patterned with sparse-sample SPLEBL and lift-off. The field-boundary is indicated by the dashed line.

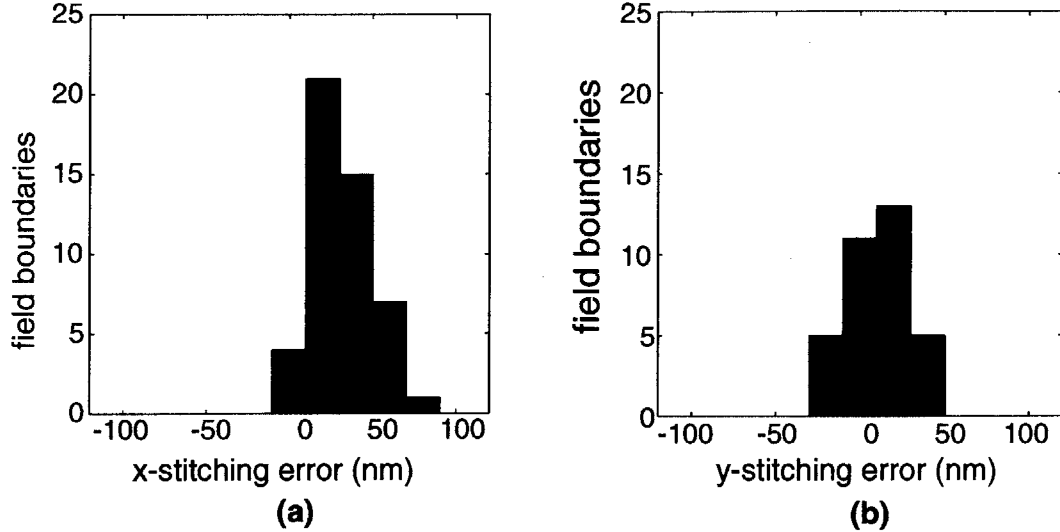

Figure 4.7: Histograms for x (**a**) and y (**b**) stitching errors obtained with a 530-nm period scintillating grid and sparse-sampled SPLEBL.

pares the spatial-phase of the patterned gratings on either side of the field boundary. Because of the high magnification and SNR of these images, the stitching error can be measured with an uncertainty of σ=3nm. Figure 4.7 shows histograms of the measured stitching errors in both X and Y. The stitching error standard deviation was 17nm and 18nm for X and Y respectively, while the mean errors were 31nm in X and 10nm in Y. The large mean values are a direct result of not correcting rotation for each field, which will be possible with improved SNR. The stitching variance is partially attributable to the 17-nm resolution[1] of the deflection DACs and the 4-nm resolution of the field shift DACs.

The patterns were written aligned to the fiducial grid, so there is no cumulative error or placement drift across the substrate. As a result, stitching errors translate directly into field-placement errors with respect to the grid. Given a field-placement errors with σ_{fp}, the stitching error is given by $\sigma_{\text{st}} = \sqrt{2}\,\sigma_{\text{fp}}$. We find that the field-placement for the experiment above varies with σ_x=12nm and σ_y=13nm. The residual

[1]The digital-to-analog converter resolution is dependent on the field size. For a 280 μm field and 14-bit DACs, the resolution is $280\mu\text{m}/2^{14} = 17$ nm.

placement error represents contributions from the deflection, field correction, and laser-interferometer DAC quantization, as well as limited phase-estimation precision from the poor signal-to-noise ratio.

Chapter 5

SPLEBL with Continuous Feedback

While the various discontinuous feedback approaches to SPLEBL are effective for certain applications, only continuous feedback will allow sub-nanometer pattern placement accuracy and eliminate pattern-dependent placement errors. Raster-scan exposure, described in section 1.1, lends itself to continuous feedback because the system addresses every exposure-grid element. If one modulates the beam current between a level that exposes the resist and a level that does not, the grid signal can be continuously monitored, even when the system scans over unpatterned areas. This chapter describes the implementation of raster-scan pattern generation and real-time spatial-phase locking on the Raith 150 EBL system. This system, coupled with a global fiducial grid patterned in thin aluminum, reduced field-stitching errors to $\sigma = 1.3$ nm without sacrificing substrate area or time for alignment steps.

5.1 Raster-Scan Pattern Generation

The simplicity of raster-scan exposure minimizes pattern-dependent errors and allows faster beam deflection across the sample. In spatial-phase locking, scanning the beam

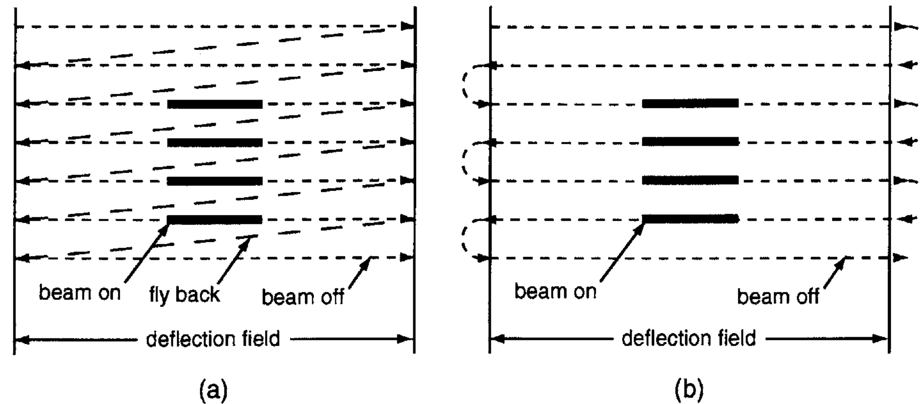

Figure 5.1: Raster-scan strategies implemented on the Raith 150. **(a)** Left-to-right only scanning with blanking and "fly back" between each line. **(b)** Boustrophedonic scanning with blanking while the beam turns and accelerates in the opposite direction.

repeatedly over the same path provides a consistent signal from the grid and simplifies deflection-distortion correction. In a vector-scan system both the grid signal and deflection errors are pattern dependent. As a result, a raster-scan strategy was developed and implemented on the Raith-150 system to enable real-time spatial-phase locking.

Unlike the raster-scan systems described in section 1.1.2, vector-scan systems, such as the Raith 150, typically do not provide a scanning stage. As a result, a hybrid approach was developed that leaves the stage stationary while the beam scans over each field. Two beam-deflection approaches were implemented on the Raith 150: left-to-right only, with blanking and "fly back" between each line, and boustrophedonic, with blanking at the end of each line while the beam turns and accelerates in the opposite direction. Figure 5.1 illustrates these two approaches. In both cases the blanker is turned on-and-off at the appropriate time to form the desired pattern.

To perform raster-scanning with the Raith 150, the standard pattern generator is used to scan the beam over the entire field while supplemental hardware and software, diagramed in figure 5.2, control the beam blanker. The Raith 150's electrostatic blanker consists of two plates extending parallel to the beam between the anode and

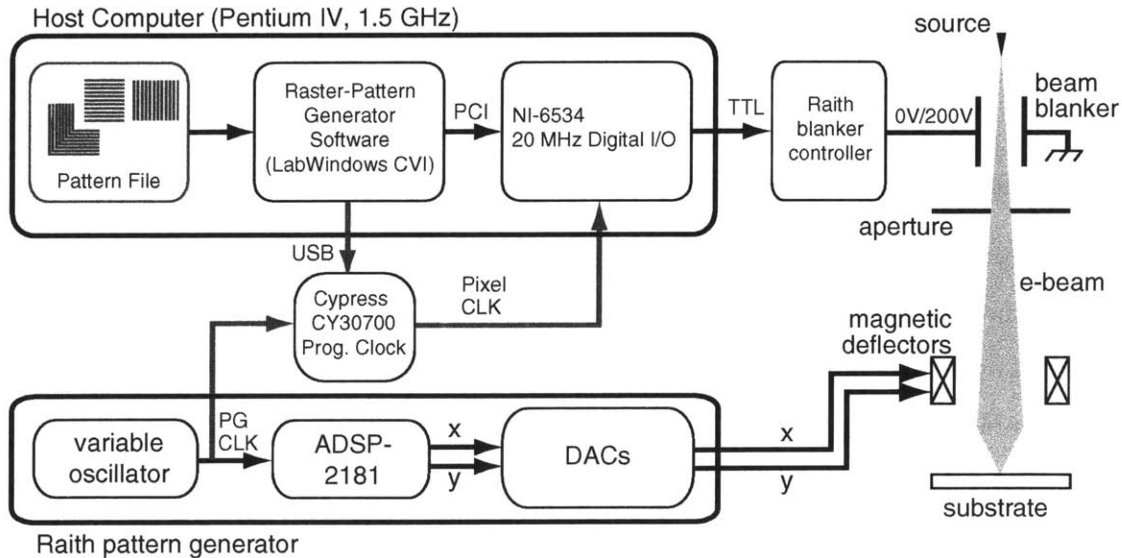

Figure 5.2: Raster-scan pattern generation sub-system for the Raith 150. A digital input/output board in the host computer controls the beam blanker which is synchronized to the beam deflection by the Raith pattern generator's clock.

the first aperture in the column. The beam is normally aligned to pass through the aperture, but when the blanker is energized the beam is deflected so that it does not. The Raith blanker requires a potential difference of 200 V on the plates, but it can be controlled with a 5 V input. This input is supplied by a digital input/output board (model PCI-6534, National Instruments, Natick, Ma.) added to the Raith control computer. The board provides continuous digital output at up to 20 MS/s, which is sufficient for the Raith system's 10 MHz address rate.

The control computer supplies the digital I/O board with data based on a user's pattern file. This pattern file contains a series of polygons defined by their vertices, and can be generated from standard GDS-II[1] files using Raith's layout software. Custom software was written to read the user's layout file and convert it to the stream of 1s and 0s sent to the beam blanker. This conversion occurs in nearly real-

[1]GDS-II is the layout standard for microlithography. A GDS-II file contains a hierarchical database of structures based on polygon primitives.

time, as the beam scans over the field, to eliminate pattern-conversion overhead and storage of large data files. Despite the capability to include polygons in the design, currently the raster-scan pattern-generator only exposes rectangles. Straightforward modifications to the software will add full polygon support in the future.

Accurate pattern placement requires precise synchronization of the beam blanker and the beam deflectors. The pattern-generator steps the beam from pixel-to-pixel based on a variable clock, and this clock is used to synchronize the deflection with the beam-blanker data stream. The pattern generator's pixel clock is based on a variable oscillator (11.111 to 16.666 MHz) that is multiplied and divided within an Analog Devices ADSP-2181 processor. The pixel clock signal is reproduced and distributed to the beam-blanker controller and the spatial-phase locking system using a Cypress Semiconductor CY30700 programmable clock board. The board contains a Cypress CY22150 re-programmable clock chip that multiplies and divides an external clock's frequency by almost any combination of integers. The CY30700 board is programmed through the universal-serial bus of the Raith 150 control computer using Cypress's CyberClocks software. If necessary, the clock can be divided further using counters on the National Instruments boards.

Figure 5.3 contains scanning-electron micrographs of a 200-nm and 400-nm period "nested L" patterns written with the Raith 150 in raster-scan mode. The beam step rate, or pixel clock, was 2.6216 MHz, corresponding to a dwell time of 380 ns per (10 nm)^2 pixel. The accelerating voltage was 10 kV, the beam current was 211 pA, and the areal dose was $80 \mu C/cm^2$. The patterns were exposed by scanning left-to-right only. The vertical pattern edges, perpendicular to the scan direction, show excellent fidelity. This is to be expected because the blanker rise and fall times are specified as less than 50 ns, or 13% of the dwell time. The horizontal pattern edges exhibit a slight modulation in the area immediately after the beam turns on. It appears that the beam is shifting back and forth along the y-direction when it unblanks. This is presumably caused by ringing of the RLC circuit formed by the blanker plates and the

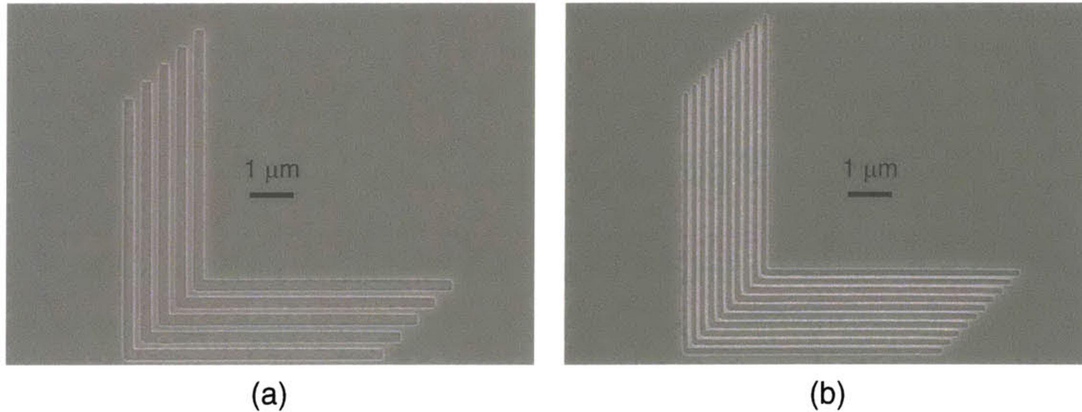

Figure 5.3: SEM of "Nested Ls" in PMMA exposed by raster-scanning on the Raith 150. The pitch of the lines is 400-nm in **(a)** and 200-nm in **(b)**.

associated wiring and power supply. This problem occurs over a time scale too short to be corrected with spatial-phase locking, so the blanker itself needs improvement. This problem has been observed in commercial mask writing systems[42], and presumably largely solved to meet current mask specification while blanking as fast as 250 ps.[43]

The ideal raster-scan SPLEBL system will allow dose modulation so that the grid can be monitored while not exposing the resist. In the Raith 150 system this could be achieved by partially deflecting the beam over the upper aperture. This will result in beam shift on the substrate, but one could anticipate this and apply an appropriate correction. When this was attempted with VS2A[44] the beam shift was found to change with time. If this is the case, one could use the fiducial grid signal to periodically measure the beam shift during the exposure.

Zhang has proposed dose modulation using a fast electrostatic stigmator to expand the beam over an aperture.[28] This technique should reduce unwanted beam deflection on the substrate. The latest MEBES mask-writing system from ETEC provides dose control by blanking the beam at every pixel. The system dwells on each pixel for 2 ns, but the beam turns on for durations between 250 ps and 2 ns, depending on the dose. This scheme provides eight dose levels[43], and could be readily

adapted to spatial-phase locking.

5.2 Real-time Spatial-Phase-Locking

As the e-beam raster-scans across the field, the grid produces a continuous signal. If the grid is aligned to the deflection axes, and the beam scans rapidly along the x-axis, we will have to acquire a number of lines of data to detect any y-deflection error. To correct for shift along both axes simultaneously, it is necessary to rotate the grid with respect to the field. With a rotated grid, one can estimate the beam shift for each axis, pass this signal through an appropriate filter, and feedback corrections to the deflection system. We implemented this strategy in the Raith 150 system by adding a dedicated microprocessor running a real-time, deterministic operating system and high-speed analog-to-digital and digital-to-analog conversion. Processing the signal in the digital domain allowed the bulk of the phase-locking and distortion-correction systems to be implemented and revised in software.

5.2.1 Beam-Shift Extraction from the Grid Signal

To provide continuous feedback control we must first extract the beam-placement error from the fiducial grid signal. Following the notation from chapters 3 and 4, we define the following coordinate system: x_P and y_P are the intended e-beam coordinates produced by the digital pattern generator. x_B and y_B are the real coordinates of the electron beam. For real-time spatial-phase locking, we are only interested in the beam shift, other deflection errors are dealt with separately, as described in 5.3. Thus, the real and intended coordinates are simply related by

$$x_B = x_P + \Delta x \tag{5.1}$$

$$y_B = y_P + \Delta y \tag{5.2}$$

To correct deflection along both axes, we wish to lock the beam position to a grid with period Λ_G that is rotated by some angle θ with respect to the scan direction. Figure 5.4 shows an SEM image of the fiducial grid rotated with respect to the scan axes. The x-axis is the fast deflection axis and the direction along which we perform phase-detection. If we assume a purely sinusoidal grid signal, we can model it as

$$S(x_B, y_B) = a\cos\left[k_0\left(x_B\cos\theta + y_B\sin\theta\right)\right] + a\cos\left[k_0\left(y_B\cos\theta - x_B\sin\theta\right)\right] \tag{5.3}$$

where the grid's spatial-frequency is given by $k_0 = 2\pi/\Lambda_G$.

If we substitute equations 5.1 and 5.2 into equation 5.3 and take the Fourier transform with respect to x_P we find that

$$\begin{aligned} F_x(k, y_P) = &\frac{a}{2}\delta\left(k \pm k_0\cos\theta\right)\exp\left[\pm jk_0\left(\Delta x\cos\theta + \Delta y\sin\theta + y_P\sin\theta\right)\right] \\ &+ \frac{a}{2}\delta\left(k \pm k_0\sin\theta\right)\exp\left[\pm jk_0\left(-\Delta x\sin\theta + \Delta y\cos\theta + y_P\cos\theta\right)\right]. \end{aligned}$$

We obtain two positive spatial-frequency components: $k_{\mathrm{HI}} = k_0\cos\theta$ and $k_{\mathrm{LO}} = k_0\sin\theta$. The phases, ϕ_{HI} and ϕ_{LO}, for these two frequencies are given by

$$\phi_{\mathrm{HI}} = k_0\left(\Delta_x\cos\theta + \Delta_y\sin\theta + y_P\sin\theta\right), \text{ and} \tag{5.4}$$

$$\phi_{\mathrm{LO}} = k_0\left(-\Delta_x\sin\theta + \Delta_y\cos\theta + y_P\cos\theta\right). \tag{5.5}$$

The last term in each of the above equations is determined by θ and y_P, both of which are known for any given measurement. This last term leads to a deterministic phase progression in ϕ_{HI} and ϕ_{LO} as the beam progresses in the y direction. Thus, we can subtract this phase offset and measure only the phase-error terms, $\Delta\phi_{\mathrm{HI}}$ and $\Delta\phi_{\mathrm{LO}}$,

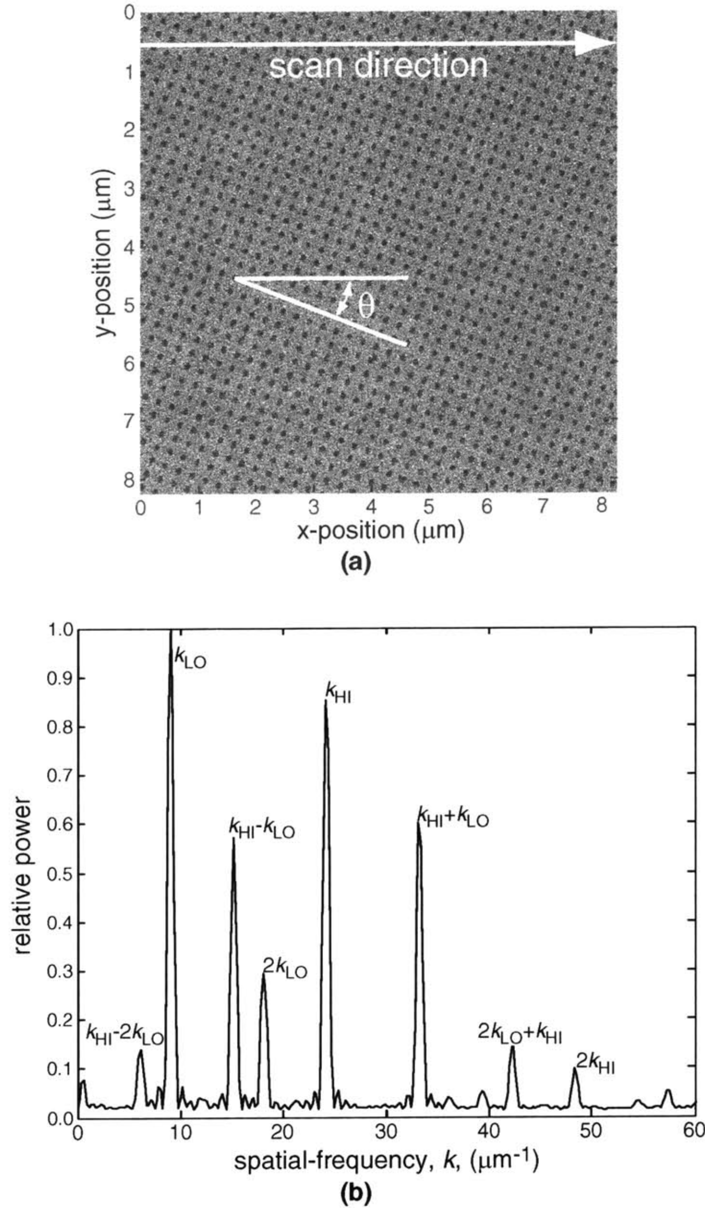

Figure 5.4: For 2D, real-time spatial-phase locking we scan the beam at an angle, θ, with respect to the grid axes. **(a)** shows a secondary electron image of a 246-nm period Al grid on SiO_2 on PMMA. The averaged spatial-frequency spectrum is shown in **(b)** where fundamental, harmonic, and sum and difference frequency components are labeled.

given by

$$\Delta\phi_{\text{HI}} = k_0 \left(\Delta_x \cos\theta + \Delta_y \sin\theta\right), \text{ and} \tag{5.6}$$

$$\Delta\phi_{\text{LO}} = k_0 \left(-\Delta_x \sin\theta + \Delta_y \cos\theta\right). \tag{5.7}$$

We calculate the x- and y- shift by solving these equations for Δx and Δy.

$$\Delta x = \frac{1}{k_0} \left(\Delta\phi_{HI} \cos\theta - \Delta\phi_{LO} \sin\theta\right), \text{ and} \tag{5.8}$$

$$\Delta y = \frac{1}{k_0} \left(\Delta\phi_{HI} \sin\theta + \Delta\phi_{LO} \cos\theta\right). \tag{5.9}$$

It is possible to extend this technique to calculate scaling, rotation, and higher-order distortions in real time. Such an analysis proceeds similarly to that of section 4.2, without assuming the high- and low-frequencies are known. After estimating k_{LO}, k_{HI}, ϕ_{LO}, ϕ_{HI}, and their first derivatives with respect to y_P, one can correct shift, scaling, and rotation for each axis in real-time. This was deemed unnecessary because these errors are relatively stable during a single exposure. In addition, one can monitor these errors, and higher-order distortions, from field-to-field using the technique described in section 5.3.

It may appear that locking to a rotated grid provides better phase-locking precision for one axis than the other. Fortunately, this is not the case. As discussed in section 2.5, if one samples several periods for each spatial-frequency, and satisfies the Nyquist criterion, the variance of the phase estimate, equation 2.3, depends only on the SNR and the number of samples. Therefore,

$$\sigma^2_{\phi_{\text{HI}}} = \sigma^2_{\phi_{\text{LO}}} = \sigma^2_{\phi} \approx \frac{2}{\gamma N} \tag{5.10}$$

where γ is the signal-to-noise ratio and N is the number of samples. If we calculate

the variance of Δx and Δy based on equations 5.8 and 5.9, we find that

$$\sigma_{\Delta x}^2 = \sigma_{\Delta y}^2 = \frac{\sigma_\phi^2 \left(\cos^2\theta + \sin^2\theta\right)}{k_0^2} = \frac{\sigma_\phi^2}{k_0^2} \tag{5.11}$$

While most rotation angles provide good phase-locking, one must remember that k_{LO} approaches zero for small angles and the discrete Fourier-transform is no-longer an efficient estimator. As θ approaches 45° both k_{LO} and k_{HI} approach $\sqrt{2}k_0/2$ and cause interference between the phase estimates. Finally, signals from metallic grids also contain harmonics and sum and difference frequencies of k_{HI} and k_{LO}, as seen in figure 5.4(**b**). Overlap between these spurious frequencies and the fundamental frequencies causes additional phase estimation errors.

5.2.2 Feedback Control Loop

SPLEBL provides closed-loop control for e-beam lithography by detecting the beam position and feeding back corrections to the deflection system. This process can be represented by the system shown in figure 5.5. The control loops for the x- and y- axes are decoupled as long as we can estimate the phase of the low- and high-frequency components independently. If the frequency separation is large enough, and care is taken with the location of spurious frequencies, this is an appropriate assumption.

Figure 5.5(**a**) shows the decoupled x-axis loop which consists of the position input from the pattern generator, X_P, the EBL system, H_S, the placement-error estimation process, H_E, physical disturbances, D_{p1} and D_{p2}, and errors in the phase-estimation process, D_e. The physical disturbances are divided between those occuring in the electronics before the SEBL system input, D_{p1}, and those occuring between the beam deflection and the sample, D_{p2}. We wish to correct the physical errors without introducing excessive noise from the estimation errors. The subtraction of X_P from X_B is necessary because only the beam placement error is being fed back, not the beam position itself.

Before analyzing the system, we make two helpful simplifications shown in figure 5.5(**b**). First, we assume that large deflection errors have been removed with field calibration, and that the SEBL system function is ≈ 1 for the small amplitude, low frequency corrections of interest. As a result, we combine the two physical disturbances into a single term, D_p. Secondly, the estimation function is a simple average over the number of samples used for the DFTs. Thus, we can move the estimation error input before the estimator sub-system in the feedback path, and increase its magnitude by $\sqrt{N}$, where N is the number of samples. This simplification decouples the impact of signal-to-noise ratio and number of samples on the error estimate. Thus, the final analysis reveals the impact of increasing or decreasing the number of samples for a constant signal-to-noise ratio.

It remains to quantify the other system functions in figure 5.5(**b**). We have implemented a discrete time feedback system, so we will work in the z-transform domain. The phase estimates are performed over a number of samples N; therefore, $\Delta\bar{x}(n)$ represents the average beam displacement from sample $n - N$ to sample n. Thus,

$$\Delta\bar{x}(n) = \frac{1}{N} \sum_{m=n-N+1}^{n} \Delta x(m), \text{ and} \tag{5.12}$$

$$H_E(z) = \frac{1}{N} \left[\frac{1 - z^{-N}}{1 - z^{-1}} \right]. \tag{5.13}$$

We describe the loop filter by its transfer function, H_F. We define transfer function coefficients, p and q, for the numerator and denominator respectively, and obtain

$$H_F(z) = \frac{p_1 + p_2\, z^{-1} + p_3\, z^{-2} + \cdots}{q_1 + q_2\, z^{-1} + q_3\, z^{-2} + \cdots}. \tag{5.14}$$

This form of the transfer function is implemented in a digital filter using the following

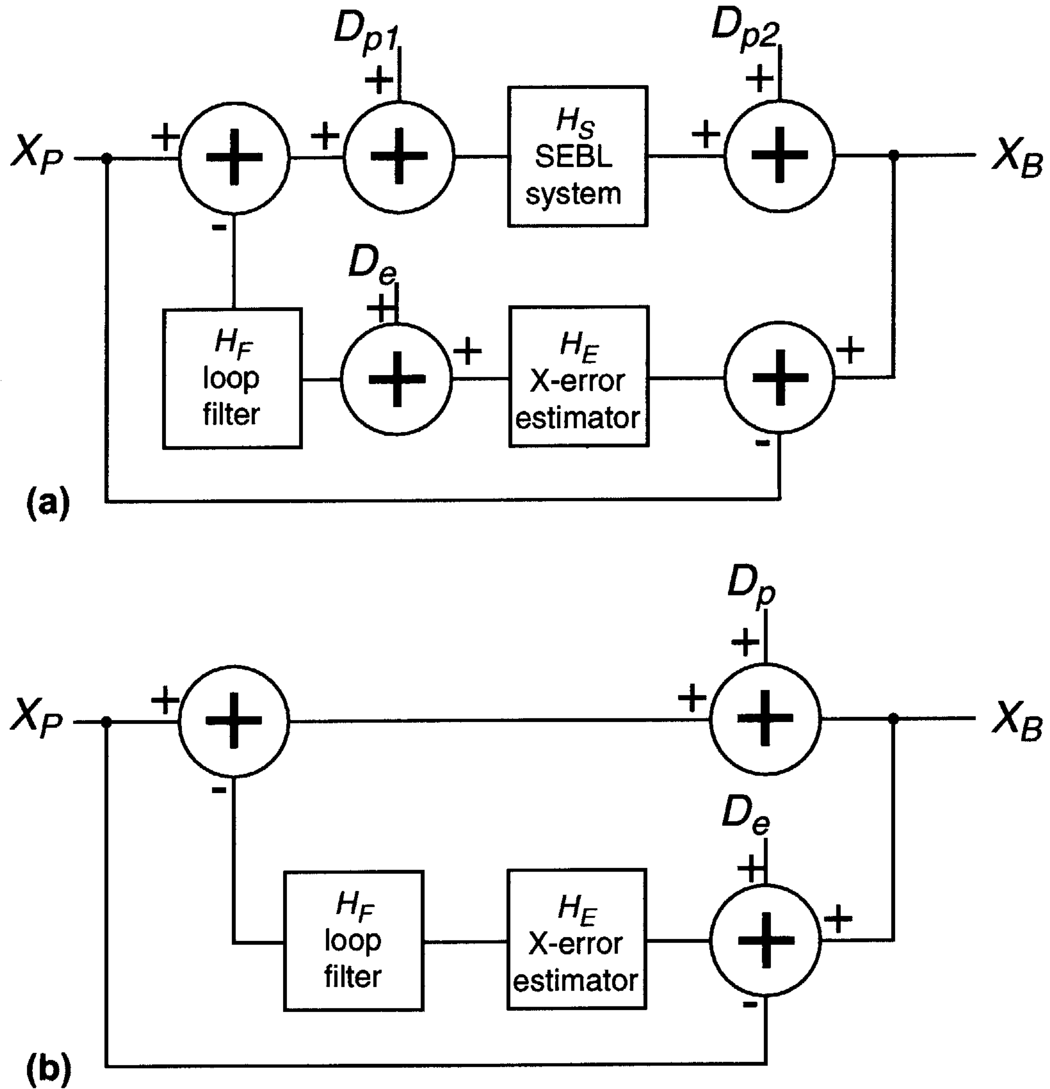

Figure 5.5: (a) Full control loop for the x-axis. The ideal beam position is given by X_P and the real beam position by X_B. D_{p1} and D_{p2} represent physical disturbances while D_e represents estimation errors. (b) Simplified x-axis control loop. The SEBL system transfer function is assumed to be 1, and the physical disturbances are combined in a single term, D_p.

algorithm.

$$q_1\delta x(n) = p_1\Delta x(n) + p_2\Delta x(n-1) + p_3\Delta x(n-2) + \cdots$$
$$- q_2\ \delta x(n-1) - q_3\ \delta x(n-2) - \cdots \quad (5.15)$$

where $\Delta x(n)$ is the nth beam-error estimate and $\delta x(n)$ is the nth filtered output for feedback correction.

Combining the estimator and loop-filter responses with the disturbance functions, the beam-placement error, is given by

$$X_B - X_P = D_e \frac{H_E H_F}{1 + H_E H_F} - D_p \frac{1}{1 + H_E H_F} \quad (5.16)$$

in the z-transform domain. Equation 5.16 reveals trade-offs in loop-filter design. For frequencies where $|H_F|$ becomes large $(X_B - X_P) \to D_e$; thus, estimation errors couple directly to the beam deflection. For frequencies where $|H_F|$ becomes small $(X_B - X_P) \to D_p$, and physical disturbances are not compensated. As a result, an intermediate filter response must be chosen such that one compensates for real disturbances without introducing errors from the phase-estimation process. Experimental details for the estimator and filter are given in section 5.4.

5.2.3 Implementation on the Raith 150 System

To implement real-time spatial-phase locking, we combined a multi-function analog input-output board (model PXI-6115) with a dedicated Pentium III, 1.26 GHz microprocessor (model PXI-8714) in a PXI[2] chassis (model PXI-1000B) all supplied by National Instruments. The general purpose microprocessor and interface bus provide a flexible platform on which to developed spatial-phase locking. The phase-locking

[2]PXI (PCI eXtensions for Instrumentation) is an enhanced version of the compact-PCI (Peripheral Component Interconnect) standard, which itself is an industrial version of the standard PCI bus found in personal computers.

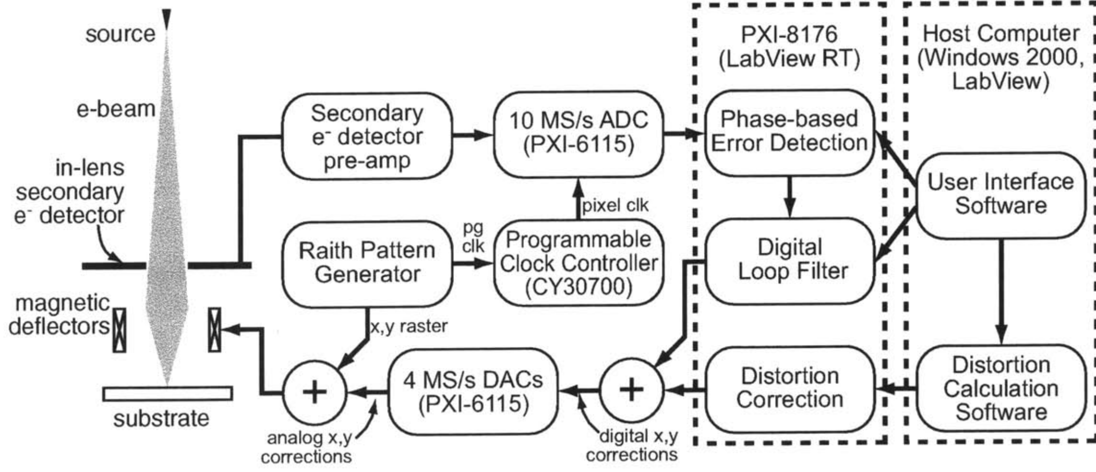

Figure 5.6: Schematic of the real-time spatial-phase locking system.

and distortion-correction algorithms reside entirely in software, allowing rapid testing and revision. Figure 5.6 shows a schematic of the real-time spatial-phase locking system. The following section discusses each component in detail.

To date, all real-time phase-locking experiments conducted with the Raith 150 system have used metallic grids and secondary electron detection. Thus, the signal from the in-lens secondary electron detector is routed to a 10 MHz analog-to-digital converter (ADC) on the National Instrument PXI-6115 data acquisition card. A 500 kHz, 3rd order, analog low-pass filter prevents aliasing in conversion.

The pixel clock derived from the pattern generator, described in section 5.1, triggers the ADC to sample the secondary electron signal at each location the e-beam addresses. Thus, one converts from spatial to temporal frequency by multiplying by the beam-deflection velocity, v_B.

$$\omega_{\mathrm{HI}} = k_{\mathrm{HI}} v_B \tag{5.17}$$

$$\omega_{\mathrm{LO}} = k_{\mathrm{LO}} v_B \tag{5.18}$$

After the data acquisition board stores the desired number of samples the data is

transferred over the PCI bus (133 MB/sec maximum bandwidth) to the Pentium processor. This processor runs National Instrument's LabView Real-Time operating system. Real-time operating systems allow deterministic system control and require few memory or processor resources. As a result, critical control algorithms run reliably and consistently. Real-time systems generally do not provide user input or video output, so the software is developed on a standard PC and downloaded to the real-time system over Ethernet. User settings and data are also passed between the real-time processor and the Raith control computer over Ethernet.

Once the sampled grid signal reaches the processor, we estimate x- and y- placement error by calculating the DFT at k_{LO} and k_{HI}. For each value of y_P, corresponding to each scanned line, we phase shift the Fourier transform kernels, $e^{-jk_{\mathrm{LO}}x_n}$ and $e^{-jk_{\mathrm{HI}}x_n}$, by $y_P \cos\theta$ and $y_P \sin\theta$ respectively. Thus, we calculate only the phase errors, $\Delta\phi_{\mathrm{LO}}$ and $\Delta\phi_{\mathrm{HI}}$, and obtain the beam shifts, Δx and Δy, from equations 5.8 and 5.9. One could also calculate the phases with the standard Fourier transform kernel and then subtract the phase-offsets, but this approach introduces wrapping errors when the phases and phase-offsets approach $\pm\pi$.

We verified the performance of the phase-detection system using the 246-nm period aluminum fiducial grid described in section 5.4. The grid was rotated -0.352990 radians with respect to the deflection axes, and sampled at a variety of signal-to-noise ratios. We adjusted the SNR by varying the beam current and beam energy. The real-time system only stores phase- and amplitude estimates for each block of 1000 samples, not the signal level for every sample of the grid. As a result, we estimate the SNR by finding the mean and variance of the two fundamental frequency amplitudes, a. For high SNR, $\mathrm{var}(a) = 2\sigma^2/N$;[36] thus, the SNR is given by $\gamma = 2\bar{a}/(N\,\mathrm{var}(a))$. This is a biased estimator, but we can reasonably correct for the bias down to $\gamma \approx 0.01$. We compare the SNR and variance of the phase-estimate over a small region (10 μm $\times$ 10 μm) where we assume the mean phase is constant. Figure 5.7 plots this comparison in terms of beam shift. One can see that the standard deviation of the shift-estimate

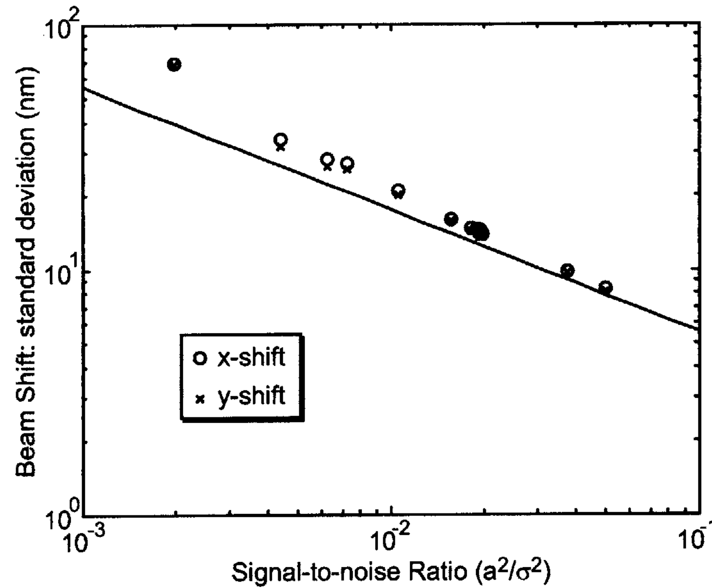

Figure 5.7: Standard deviation of shift error versus SNR measured over 10 μm $\times$ 10 μm regions of the deflection field. Also shown is the Cramer-Rao bound for phase-estimation of a sinusoid in white noise. Because the measured standard deviations track the lower bound, instead of reaching a minimum, we remain in a noise limited regime.

tracks the Cramer-Rao bound, so we remain in the noise limited regime. We need to filter the feedback signal to compensate for real disturbances without introducing additional errors from phase-estimation uncertainty.

The results from the shift-error calculation are passed to the digital loop-filter. The user specifies the filter coefficients based on equation 5.14 and the software calculates the filtered output using equation 5.15. A separate routine allows the filter coefficients to change, depending on exposure location. For example, a larger bandwidth filter can be used for the first few lines of the field to rapidly correct the initial beam-position error. Once this error is corrected, the filter bandwidth can be narrowed to reduce the effect of estimation errors. In addition, fully exposed areas will have higher signal-to-noise ratios than sparsely patterned areas, and one might wish to adjust the filter coefficients based on pattern density. Currently, these adjustments must be preprogrammed by the user, but one can imagine an adaptive algorithm that

monitors the signal-to-noise ratio and physical disturbances to continuously optimize the filter coefficients.

Next, we multiply the loop-filter output for each axis by a scaling factor to convert from beam displacement to the voltage required for deflection. These signals, x and y, are routed to the digital-to-analog converters whose output is summed electronically with the main deflection signal. For a 10kV exposure using a 100 μm field the beam deflects 300 nm/V. A voltage divider in line with the correction signal reduces this to 10 nm/V. The range of the DAC output, ($\pm$10V), covers corrections up to $\pm$100nm with 12-bit precision (LSB $\approx$ 0.05 nm). This range is sufficient for the errors found in a single field; however, the total drift between beam and stage over an entire exposure may be several hundred nanometers. Thus, after each field we add the cumulative correction to the Raith 150's shift correction which ranges up to $\pm 80\mu$m . At the beginning of the next field the phase-locking system's correction is reset to zero.

5.3 Higher-order Distortion Correction

Several experiments with the Raith 150 revealed field-distortions that were not well corrected by first order (scale, rotation, and shift) parameters. Higher-order distortions must be minimized to achieve nanometer level pattern placement. Scanning over the fiducial grid is an excellent way to measure these errors, and one would hope to correct them using spatial-phase locking. Unfortunately, some of the distortions cause the beam position to vary too rapidly across the field for the SPL system to correct. As a result, we measure these distortions with respect to the fiducial grid, and then add the appropriate corrections to the feedback signal while exposing each field. The distortions need only be measured once per exposure, so the overhead time for this procedure is negligible.

It is not surprising that one can extend the field corrections in sections 3.1 and 4.2 with higher order terms. To improve distortion in the Raith 150 system we

implemented correction through third order with 10 terms per axis. We express the relationship between the desired and actual beam position in a manner analogous to section 3.1.

$$\begin{aligned} x_B = &\ a_0 + a_1 x_P + a_2 y_P + a_3 x_P y_P + a_4 x_P^2 + a_5 y_P^2 \\ &+ a_6 x_P^3 + a_7 y_P^3 + a_8 x_P^2 y_P + a_9 x_P y_P^2 \end{aligned} \tag{5.19}$$

$$\begin{aligned} y_B = &\ b_0 + b_1 x_P + b_2 y_P + b_3 x_P y_P + b_4 x_P^2 + b_5 y_P^2 \\ &+ b_6 x_P^3 + b_7 y_P^3 + b_8 x_P^2 y_P + b_9 x_P y_P^2 \end{aligned} \tag{5.20}$$

where, once again, x_P is the ideal beam position and x_B is the actual beam position. One could estimate the coefficients in equations 5.19 and 5.20 by moving the stage to 10 different position and measuring the deviation of an image from it's expected position, but this is unnecessary with spatial-phase locking available. If one disables the feedback signals to the deflection system, and simply records the spatial-phase of the grid throughout the field, it is relatively straightforward to calculate the coefficients above.

In our implementation, we divide the deflection field into a 10×10 array of blocks. For a 100 μm field each of these blocks is 10 μm on a side, and if the address grid is 10 nm, each block contains 1000×1000 samples of the grid. Calculating the average beam-placement error in each of these blocks provides a map of the field distortion after only a single raster-scan. Figure 5.8(**a**) shows typical distortion with only first order corrections applied. The outermost distortion measurements are not shown in order to make the central region more clear. The extreme distortion at the left edge of the field is induced by the beam "fly back" between each exposed line. This error is reduced for boustrophedonic scanning, but different correction coefficients are required for left-to-right and right-to-left scanning. Distortion correction for both directions during boustrophedonic scanning is a straightforward and important future improvement.

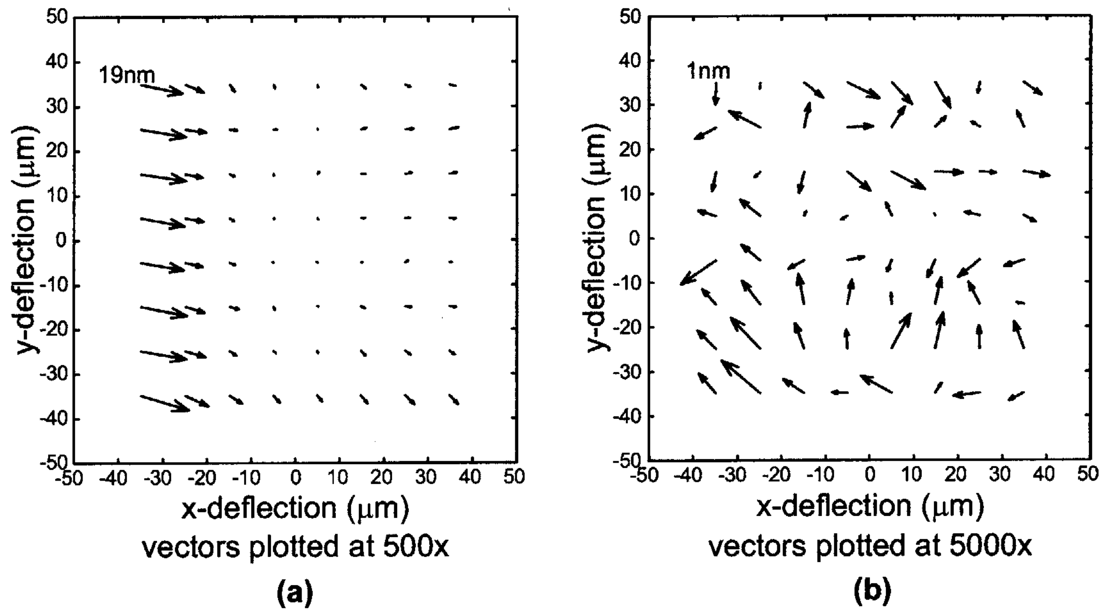

Figure 5.8: Field distortion maps: **(a)** First order correction only. **(b)** Correction through third order. Vectors indicate beam displacement from desired position for each point in the field. Note the difference in vector scaling between the two plots.

Once a distortion map has been constructed one can calculate the correction coefficients with a least-squares solution to the following matrix equation.

$$\begin{bmatrix} x_{B1} \\ x_{B2} \\ x_{B3} \\ \vdots \\ x_{B100} \end{bmatrix} = \begin{bmatrix} 1 & x_{P1} & y_{P1} & x_{P1}y_{P1} & x_{P1}^2 & y_{P1}^2 & x_{P1}^3 & y_{P1}^3 & x_{P1}^2 y_{P1} & x_{P1}y_{P1}^2 \\ 1 & x_{P2} & y_{P2} & x_{P2}y_{P2} & x_{P2}^2 & y_{P2}^2 & x_{P2}^3 & y_{P2}^3 & x_{P2}^2 y_{P2} & x_{P2}y_{P2}^2 \\ 1 & x_{P3} & y_{P3} & x_{P3}y_{P3} & x_{P3}^2 & y_{P3}^2 & x_{P3}^3 & y_{P3}^3 & x_{P3}^2 y_{P3} & x_{P3}y_{P3}^2 \\ & & & & & \vdots & & & & \\ 1 & x_{P100} & y_{P100} & x_{P100}y_{P100} & x_{P100}^2 & y_{P100}^2 & x_{P100}^3 & y_{P100}^3 & x_{P100}^2 y_{P100} & x_{P100}y_{P100}^2 \end{bmatrix} \begin{bmatrix} a_0 \\ a_1 \\ a_2 \\ a_3 \\ a_4 \\ a_5 \\ a_6 \\ a_7 \\ a_8 \\ a_9 \end{bmatrix} \quad (5.21)$$

the coefficients for y-deflection correction can be calculated in the same way. These calculations are stored for the duration of the exposure and the appropriate corrections are added to the feedback signal as the beam scans over the field. Figure 5.8(**b**) shows the residual distortion after applying third order corrections. In the current implementation this correction is updated every 1000 samples; as a result, there are discretization errors at the left edge of the field not observable in the distortion map. Although the mean error is minimized for this region, the error changes too rapidly over 10 μm to be adequately corrected. For the experiments described in section 5.4 we used only a 60 μm $\times$ 60 μm section of the field where the discretization error is below 1 nm.

5.4 Field-Stitching Experiments

We conducted field-stitching experiments to assess the effectiveness of real-time spatial-phase locking. In the absence of a dose-modulation scheme we were limited in the patterns that can be exposed. Nevertheless, we wrote arrays of 200-nm-period gratings with stitching errors below 1.3-nm (1-σ). In addition, every feature is placed with respect to the fiducial grid, so long-range pattern placement exhibits comparable precision.

An aluminum lattice served as the fiducial grid for the first set of real-time spatial-phase-locking experiments. Zhang developed a process, detailed in reference [28], to place such a lattice on top of a 100-nm thick layer of PMMA resist with the help

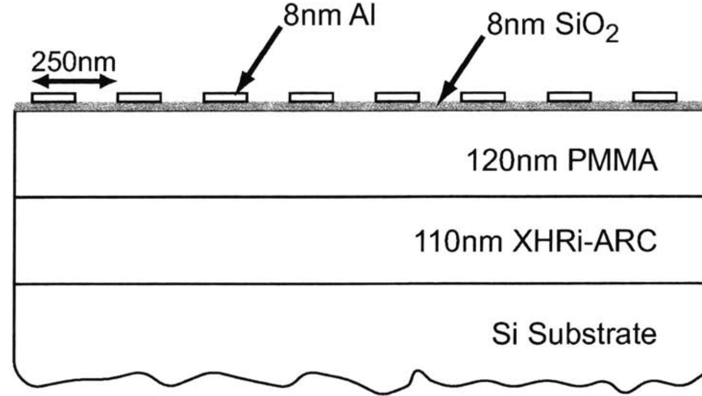

Figure 5.9: Resist and fiducial grid cross-section for real-time SPLEBL exposures developed by Zhang[28]. The anti-reflection coating (ARC) reduces the vertical standing wave in interference lithography, while PMMA serves as the e-beam resist. The SiO_2 layer prevents interaction of the positive IL resist with the PMMA, and the aluminum lattice forms the fiducial grid. The top two layers are largely electron transparent.

of a 8-nm-thick SiO_2 interlayer and an underlying anti-reflection coating. The final layer structure is shown in figure 5.9. This particular structure was chosen to provide electrical continuity so that the grid could be biased for voltage contrast experiments. These experiments are currently underway, but we did not use voltage contrast for initial spatial-phase-locking tests.

The grid itself was patterned with interference lithography in a positive resist (Sumitomo PFI-88) using a Lloyd's-mirror interferometer and a 325-nm wavelength HeCd laser. Two orthogonal exposures produced an array of posts in resist, and an 8-nm-thick aluminum layer was electron-beam evaporated onto to the sample. When the resist was removed only the aluminum lattice remained. Mirror non-flatness and spurious interference patterns limit the spatial-coherence of grids patterned with the Lloyd's-mirror inteferometer; therefore, one would not use such an interferometer for real masks or devices. However, the Lloyd's mirror provides rapid and convienient process development and the resulting grids are adequate for testing spatial-phase locking.

A sample with a 246-nm period grid was loaded into the Raith 150 system at an angle of approximately -0.352 radians (≈ -20.2 °) with respect to the stage's x-axis. The deflection system can correct up to $\pm 6°$ of rotation, so mechanically setting the angle with a protractor was sufficient. Once loaded in the system, the laser-interferometer controlled stage was mapped to the grid coordinates by following a single grid line over several millimeters. Zhang wrote software automating the stage movement and angle calculations.[28]. The stage was adjusted to move along axes rotated -0.352990 radians with respect to the grid. This angle was chosen because it provided an integral number of periods for k_{HI} and k_{LO} across a 99.624 μm field. As a result, one need not track accumulated phase shift from field to field. Field-to-field phase tracking can be implemented in future software revisions.

The Raith 150 system was configured for operation with a 10 keV beam energy and 172.9 pA beam current. Beam focus and stigmation were optimized by imaging 40-nm-diameter Au spheres applied to an unused portion of the sample from a colloidal suspension. Because we have not implemented a dose-modulation scheme in the Raith system, a test pattern was chosen where the beam remains on during almost the entire field exposure. This pattern, shown in figure 5.10, consists of 200-nm period vertical and horizontal gratings at each field boundary. Instead of exposing the grating lines themselves, we expose the entire surrounding area. After development, PMMA remains in regions where the beam was briefly turned off.

The Raith 150 system is installed close to a city street that is under construction, so the exposures were conducted at night when there is reduced vibration. Increasing the signal-to-noise ratio of the grid, and thus expanding the bandwidth of the feedback loop, would allow exposures in the presence of larger mechanical and acoustic disturbances.

The test pattern was isolated to a $60 \times 60\mu m$ region of the field where $-20\mu m \leq x \leq 40\mu m$ and $-30\mu m \leq y \leq 30\mu m$. Although the third order distortion correction removes the mean displacement error over a larger area; these corrections are currently

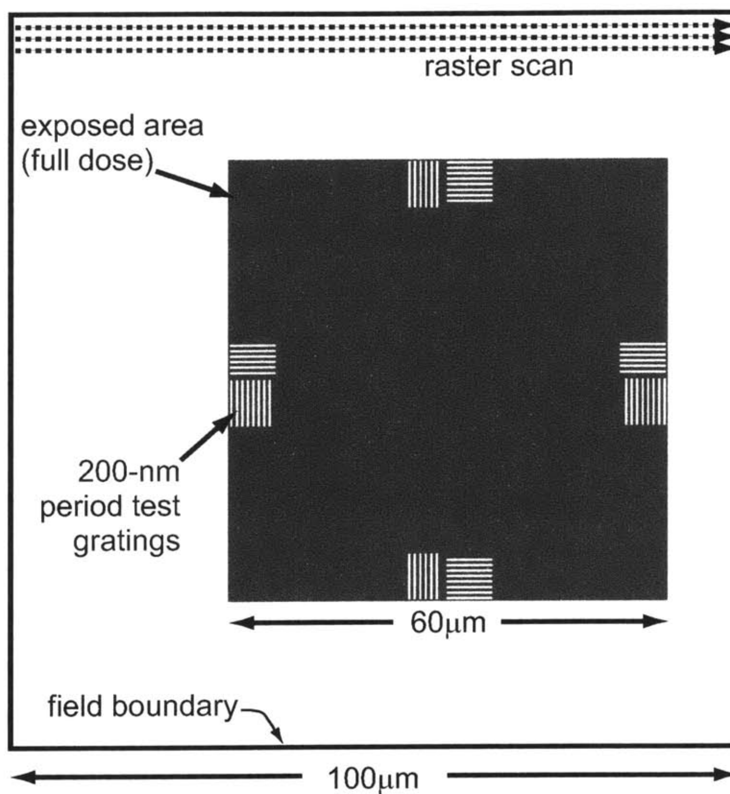

Figure 5.10: Field-stitching test pattern for real-time spatial-phase locking. The exposed pattern occupies a 60 μm $\times$ 60 μm square within the 100 μm field. The pattern contains horizontal and vertical 200-nm period gratings at the field boundaries for stitching measurements.

updated too infrequently. At the left edge of the field, when the beam is beginning its scan, errors within the 10 μm correction regions change by several nanometers. Thus, we decided to restrict the pattern to a region with sub-2-nm residual distortions. Patterning larger regions of the field will be possible after software revision for more frequent distortion correction.

The desired 10 keV dose, D, for such a pattern in PMMA is $70\mu C/cm^2$. With the given beam current, I_B, and a 9.962-nm (99.624 μm /10000) address grid, l, the dwell-time, dt, is

$$dt = \frac{l^2 D}{I_B} = 405 \text{ ns per pixel.} \tag{5.22}$$

This translates to a 2.469 MHz pixel clock. The patterns were exposed from left-to-right only, and 3 ms was allotted for beam settling after fly-back between lines. As a result, each field required 70 seconds to expose. This is not a throughput limit, even for the Raith system. Boustrophedonic scanning would reduce this exposure time to 40 seconds by eliminating most of the fly-back delay. In addition, one could use the full pattern generator speed, 10 MHz, with a higher beam current (available with only slight sacrifice of resolution) to obtain 10 second field exposures. These improvements would be beneficial for laboratory use, but the Raith system is fundamentally unsuited for high-throughput exposures.

We exposed 7×7 field arrays of the test pattern in figure 5.10 so that the gratings at the edge of one field align with those of the four adjacent fields. Figure 5.11 shows the overall pattern layout. Before starting the exposure we scanned the fiducial grid and calculated the first-order field correction coefficients (scale, rotation, and shift). These corrections were applied with the Raith field-correction hardware. Then we scanned

the grid twice more and calculated corrections through third order.[3] These revised corrections were applied simultaneously with the spatial-phase locking corrections.

Scanning the grid at the exposure dose showed that the standard deviation of the x- and y- shift estimates, over a 10μm $\times$ 10μm region, was $\approx$ 14 nm. As discussed in section 5.2, this is clearly in the noise limited regime. Therefore, we set the loop filter coefficients to [0.0025 0.0025] for the numerator and [1 -1] for the denominator. This is approximately equivalent to an accumulator with a gain of 0.005. This should provide a noise component of $\sigma \approx 1$ nm for the feedback control signal. For the first 4 lines (40 nm) of the field the numerator coefficients were increased by a factor of 16. This allows the system to rapidly correct for the initial placement error present at the beginning of each field. Of course, this trade-off adds noise to the system for the first 4 lines in the field. Figure 5.12 plots the calculated system response for physical disturbances, $1/(1 + H_E H_F)$, for the initial and standard filter coefficients.

After exposing the grating pattern we removed the aluminum grid and the SiO_2 interlayer using a buffered hydrofluoric acid solution ($\approx$10% HF, Transene Co. Inc., Danvers, Ma.). We developed the PMMA in a solution of IPA and MiBK (2:1 by volume) for 60 seconds at 21.0 ° C. The PMMA on ARC gratings were sputter coated with a gold-palladium alloy before measuring the stitching errors. Figure 5.13 shows the aligned gratings across the vertical and horizontal field boundaries. Beam blanking oscillations are visible at the left edge of the horizontal grating lines.

The stitching precision was measured by comparing the spatial-phase of the grating across the field boundaries. Figure 5.14 shows histograms of the x- and y-stitching

[3]For reference, the final correction values were

$$
\begin{array}{llll}
a_0 = 8.95E-6\mu m & a_5 = -3.0874E-7\mu m^{-1} & b_0 = 4.22E-3\mu m & b_5 = 2.4451E-6\mu m^{-1} \\
a_1 = 9.9994E-1 & a_6 = 2.4776E-7\mu m^{-2} & b_1 = -7.3047E-6 & b_6 = -3.405E-8\mu m^{-2} \\
a_2 = 4.8335E-5 & a_7 = -1.1354E-8\mu m^{-2} & b_2 = 9.9998E-1 & b_7 = -5.9220E-9\mu m^{-2} \\
a_3 = -6.4194E-7\mu m^{-1} & a_8 = -1.8704E-8\mu m^{-2} & b_3 = -1.1284E-6\mu m^{-1} & b_8 = -7.6222E-9\mu m^{-2} \\
a_4 = -7.877E-6\mu m^{-1} & a_9 = -5.751E-9\mu m^{-2} & b_4 = 1.9806E-6\mu m^{-1} & b_9 = 1.7146E-8\mu m^{-2}
\end{array}
$$

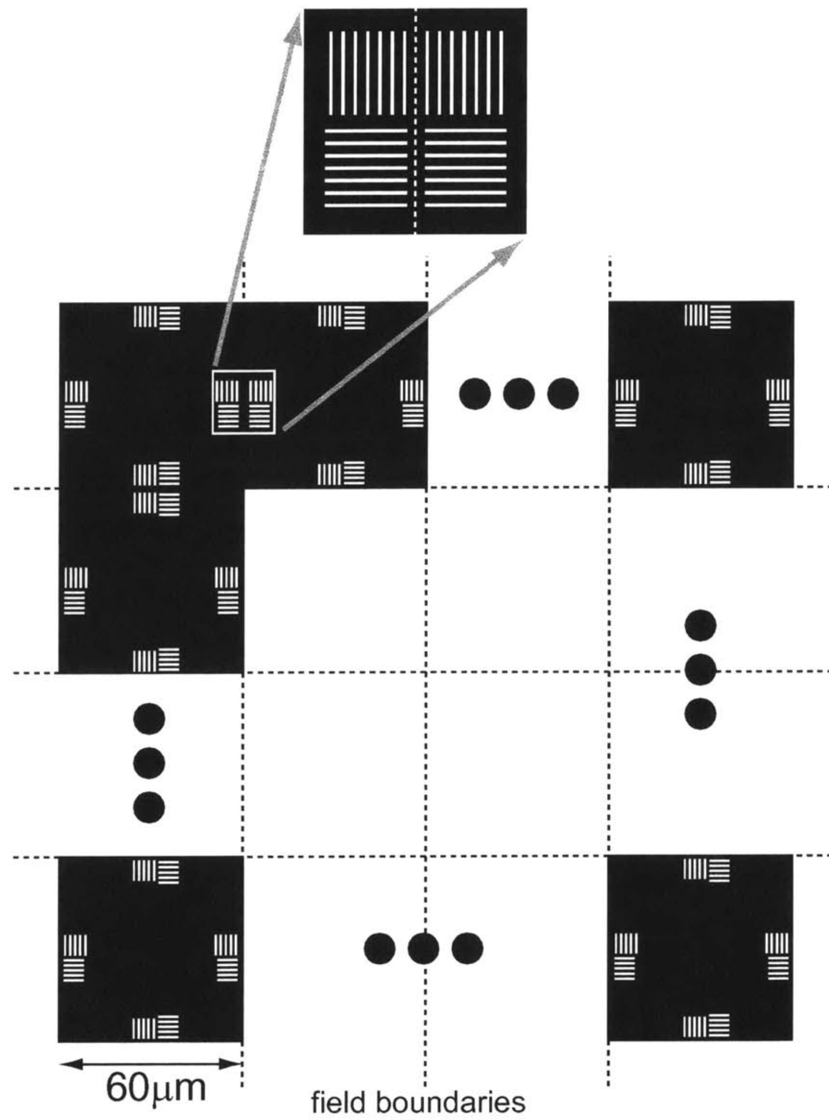

Figure 5.11: Full pattern layout for field-stitching experiments. A 7×7 array of fields was exposed with the gratings aligned at each edge.

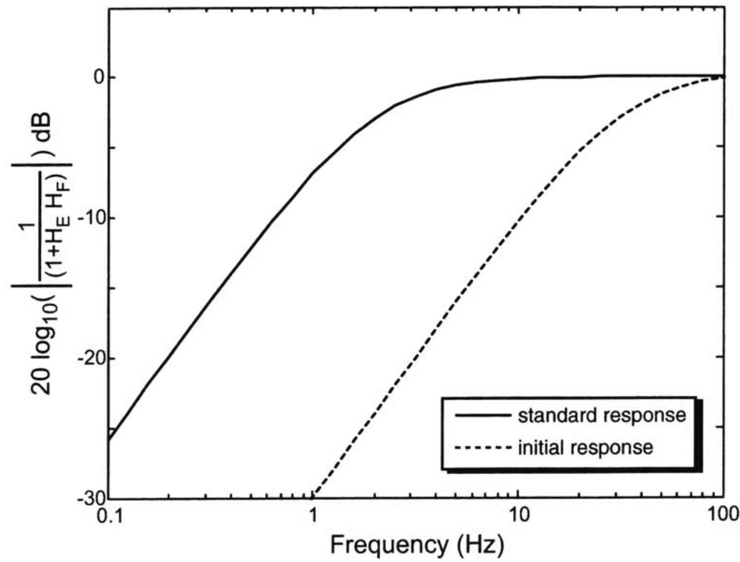

Figure 5.12: Calculated system response for physical disturbances for a 1000 point phase estimate. The dashed line indicates the response for the first 4 lines in the field, and the solid line for the remainder of the field.

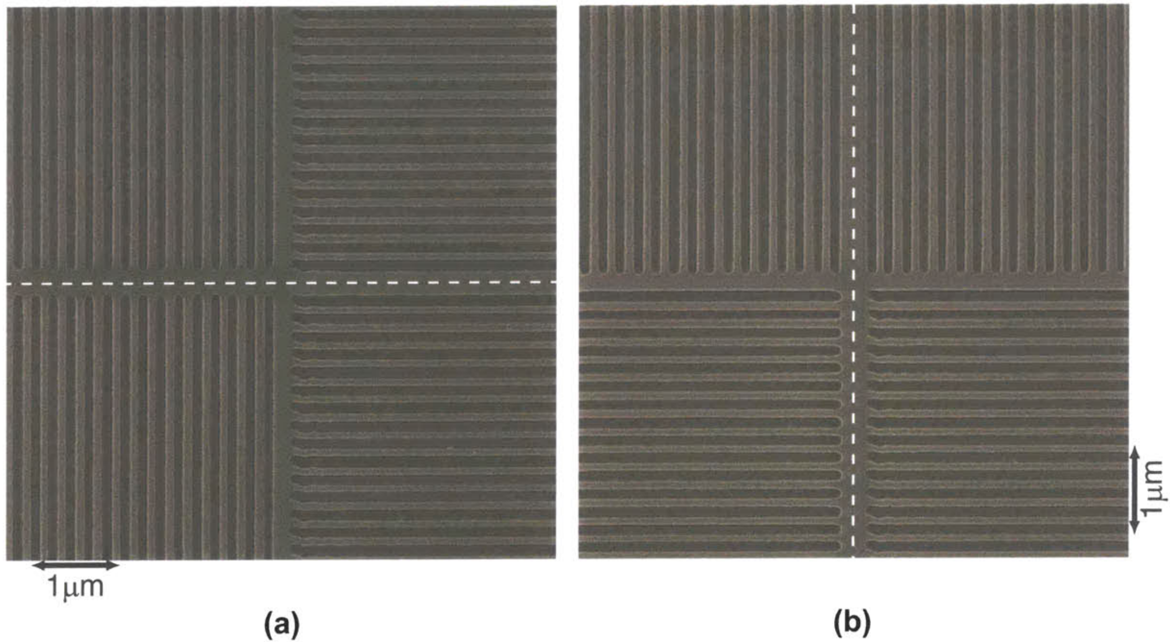

Figure 5.13: SEM of stitched gratings at the **(a)** horizontal and **(b)** vertical field boundaries. The pattern intentionally contains gaps between gratings so that the boundaries, denoted by the dashed line, could be identified.

errors for vertical and horizontal boundaries. The mean errors, μ_{st}, range from -1.4 to 2.5 nm and the standard deviations, σ_{st} from 1.0 to 1.3 nm. Remeasuring the same grating pair 42 times yielded a standard deviation of 0.2 nm, so the measurement uncertainty is not significantly contributing to the observed standard deviations. In comparison, the manufacturer specifies stitching precision for the Raith 150 system as 40 nm, mean + 2 standard deviations. Our own evaluation of the system showed stitching errors between $\mu = -0.6$ nm, $\sigma = 6.2$ nm, and $\mu = -15.4$ nm, $\sigma = 9.1$ nm for a single exposure depending on location in the field.[45].

The Raith system does not guarantee global pattern placement, and the relative beam and stage position was found to drift by ≈ 6 nm per minute without spatial-phase locking. The system drifts faster until the sample and stage have thermally stabilized, and can drift more slowly under certain conditions.[45] In contrast, all patterns exposed using spatial-phase locking are positioned with respect to the fiducial grid. As a result, we can estimate overall pattern-placement errors from relative stitching measurements. If the placement errors of features on opposite sides of the field boundary are uncorrelated, then the pattern placement precision, σ_{pp}, with respect to the grid is given by $\sigma_{pp} = \sigma_{st}/\sqrt{2} \leq 0.9$ nm. Without spatial-phase locking, stitching measurements are not a reliable measure of global placement precision. The slow drifts described above may produce small stitching errors while a large global placement error accumulates

These results were obtained with the Raith 150, a converted scanning-electron microscope, in a standard laboratory environment. No special efforts were made to control temperature fluctuations, vibration, or electromagnetic interference beyond those present in the original electron microscope. The pattern-placement quality, though limited by the grid signal-to-noise ratio, confirms the importance of closed-loop control.

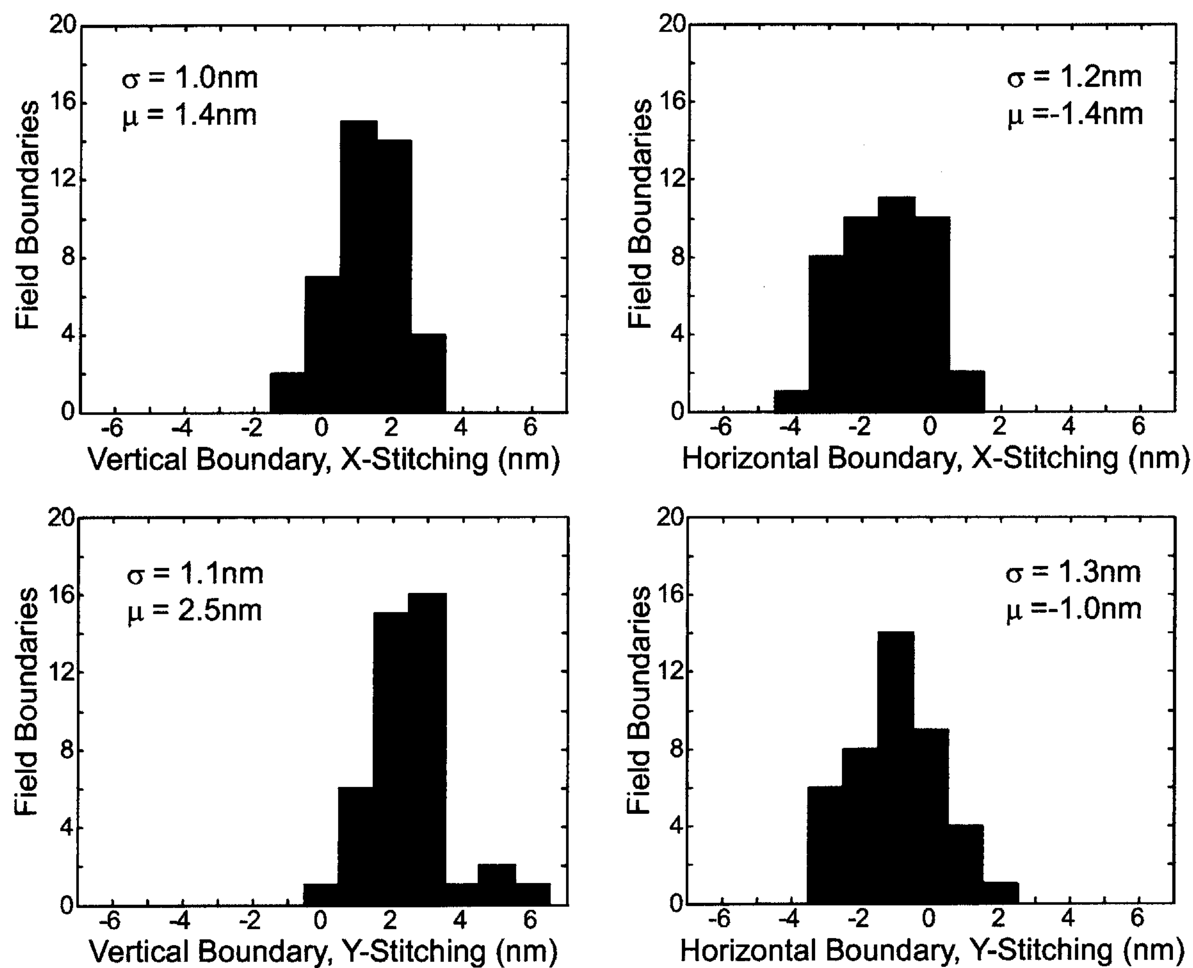

Figure 5.14: Stitching error histograms from real-time SPLEBL exposures. X- and Y-stitching measurements are shown for both vertical and horizontal boundaries, and the mean, μ, and standard deviation, σ, are included.

Chapter 6

Silicon-on-insulator Integrated Optical Devices

Optical data transmission is the only technology available that can meet the demand for high-bandwidth, long-distance communications. As these communications networks grow in complexity, they will increasingly rely on compact, integrated components that manipulate signals in the optical domain. Planar processing promises to bring the same manufacturability and miniaturization to optical devices that it has to semiconductor devices. The promise of integrated optics remains only partially fulfilled because optical devices place different demands on the materials and fabrication techniques than do electronic devices. One key example of this is the integrated-Bragg-grating filter.

A number of integrated-optical components require diffraction gratings, periodic modulations of refractive index or physical structure, within an optical waveguide. Examples include distributed-feedback (DFB) and distributed-Bragg-reflector (DBR) lasers, gain equalization filters, dispersion compensators, input/output couplers, and channel add/drop filters for wavelength-division-multiplexing (WDM). Some of these devices are realized in photosensitive optical fiber, but most candidate materials for integrated optics are not photosensitive. Modulation of the physical waveguide di-

mensions by lithographic patterning provides a general technique to form gratings in any material.

This chapter addresses the design, fabrication, and performance of grating-based filters for wavelength-division-multiplexing (WDM) using silicon as the waveguide core material. The devices were designed around standard WDM system bandwidths and channel spacings. In contrast to typical devices, the gratings were patterned in the sides of the waveguide instead of the top or bottom. This geometry provides additional design flexibility and reduces fabrication complexity. Spatial-phase-locked e-beam lithography guarantees highly-coherent gratings. The filter performance was characterized and compared to the predictions of coupled-mode theory.

6.1 Integrated-Bragg Grating Theory

To design useful grating-based devices one needs to describe the propagation of light in a waveguide with a periodically varying refractive index or physical dimension. Thus, we wish to find time-dependent solutions to Maxwell's equations in three dimensions. Typically, one employs numerical techniques with a range of simplifying assumptions that trade accuracy for reduced computational time. Rapid numerical results are essential if one wishes to consider a broad range of design parameters, but the chosen techniques must provide sufficient accuracy such that fabricated devices function properly.

The time required for fabrication and testing greatly exceeds that required for design, so it would seem that any investment of resources in more accurate modeling would be worthwhile. While generally true, such an investment cannot be made blindly without verifying the techniques with real devices along the way. In addition, design techniques must account for real-world fabrication tolerances. An issue that is all too often neglected.

This section presents techniques to determine the electric and magnetic fields for

waveguides with integrated gratings. First, we analyze the fields in uniform waveguides, and then we introduce coupled-mode theory to model the fields in the presence of a grating. From the coupled-mode solutions for a uniform grating we build up models for the non-uniform gratings necessary for WDM channel add/drop filters.

6.1.1 Integrated Waveguides with Gratings

Dielectric waveguides consists of a higher refractive-index core region surrounded by a lower refractive-index cladding region. Light is guided in the core region by total-internal reflection, and the boundary conditions yield discrete solutions to Maxwell's equations. These solutions describe the waveguide's modes of propagation. Cylindrical glass optical fiber is the most common optical waveguide in use, while integrated optical devices use a variety of materials and geometries.

Two of the most common planar waveguides are illustrated in Figure 6.1. The channel waveguide, Figure 6.1(**a**), consists of a rectangular core region embedded in a uniform cladding region. Figure 6.1(**b**) depicts a ridge waveguide, the geometry addressed in this work. Ridge waveguides confine light vertically with high and low refractive-index layers, while the ridge protruding from the high-index slab provides lateral confinement. The most common coordinate definition for waveguide analysis is also shown in 6.1(**b**).

To introduce gratings one must periodically modulate the waveguide's dimensions or refractive index. Typical materials used for planar waveguides are not photosensitive. One cannot induce a permanent refractive-index change by exposure to light, so physical changes of geometry provide the most general solution. Considering the waveguides described above we can imagine placing a grating at one or more of the core-cladding interfaces. Figure 6.2(**a**) shows a typical channel waveguide with a grating at its top interface. Placing the gratings in the sidewalls of the waveguide, figure 6.2(**b**), is equally effective and presents several advantages. Gratings can be introduced in ridge waveguide structures as shown in figure 6.2**c** and **d**.

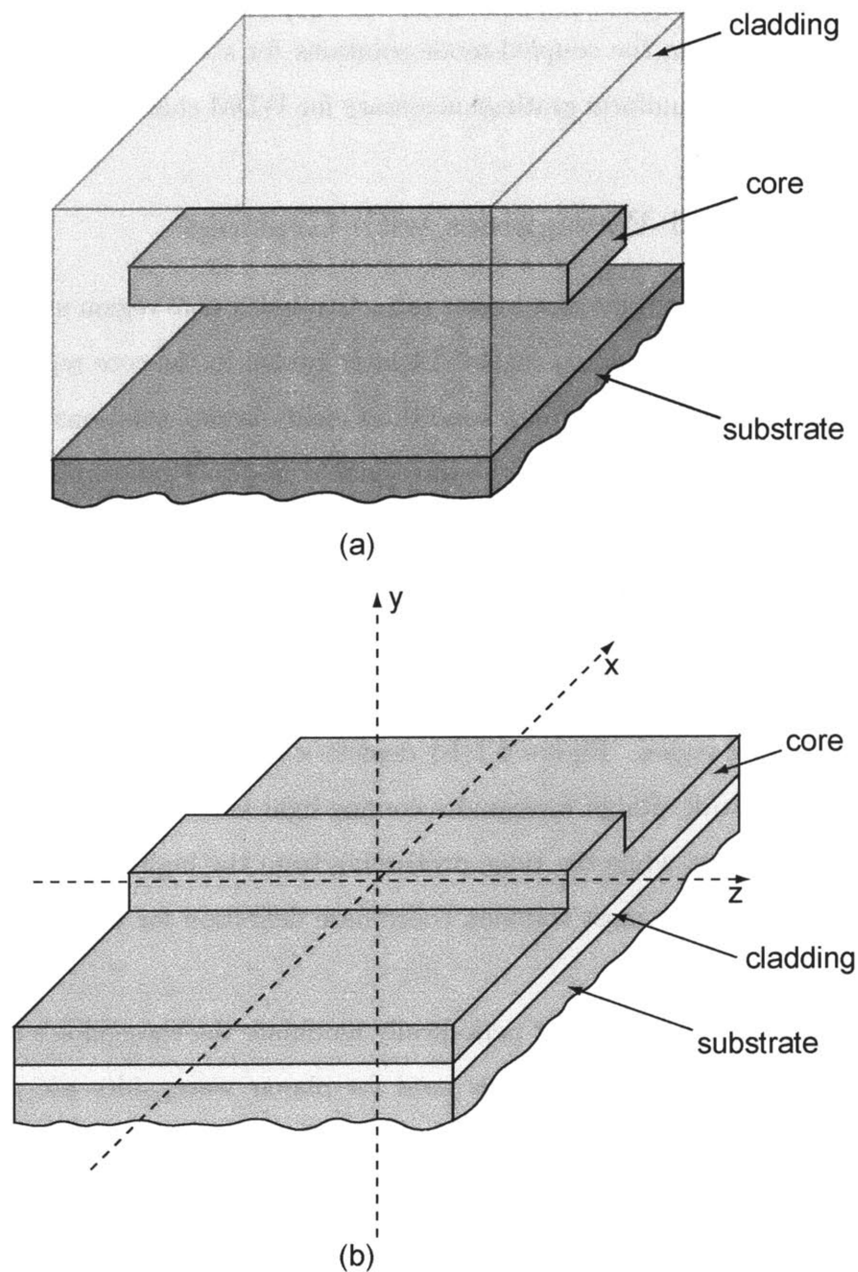

Figure 6.1: Common waveguide geometries achieved in planar processing. **(a)** Rectangular channel waveguide. **(b)** Ridge waveguide. **(b)** also shows the most common coordinate system for waveguide analysis.

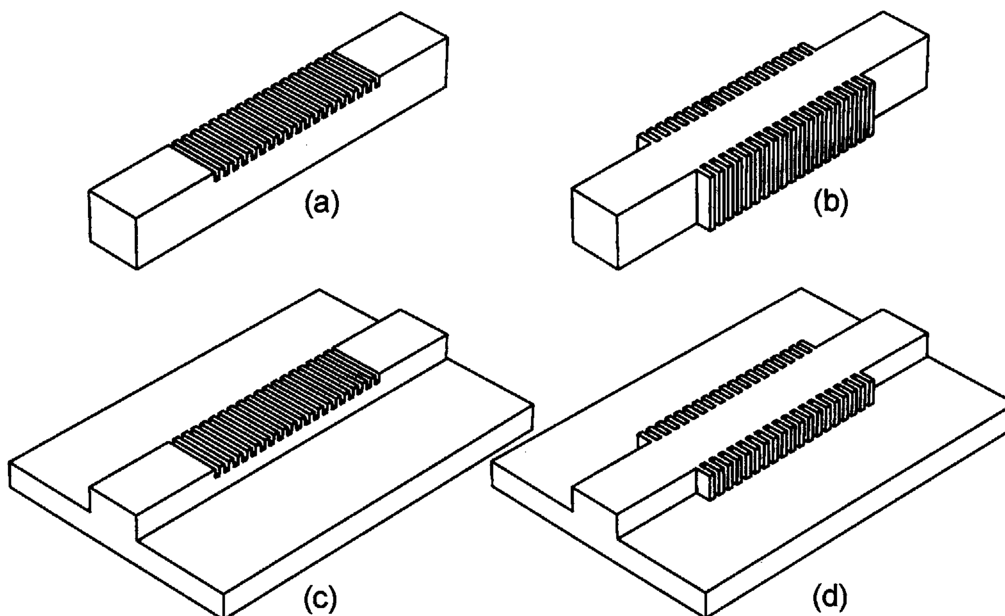

Figure 6.2: A few possible waveguide-grating structures. **(a)** Rectangular channel waveguide with grating at the top core-cladding interface. **(b)** Channel waveguide with sidewall gratings. **(c)** and **(d)** Ridge waveguides with top and sidewall grating.

Fully functional add/drop filters typically require additional waveguide structures. The most basic of these is the co-directional coupler. An integrated coupler transfers a desired amount of power (often 50%) from one waveguide into another. This is usually accomplished by bringing the waveguides close together over a prescribed distance. A Mach-Zehender interferometer can be formed from two 50% couplers and two identical gratings as shown in figure 6.3. To design any such device we must begin with the analysis of a uniform waveguide.

6.1.2 Uniform Waveguide Analysis

One of the most effective design techniques in balancing accuracy and computational intensity is to model a uniform waveguide and then treat gratings, or coupled waveguides, as perturbations. A uniform waveguide's refractive-index profile, $n(x, y)$, is defined over the x-y plane and is invariant in the $\mathbf{z}$ direction. As a result, it will have

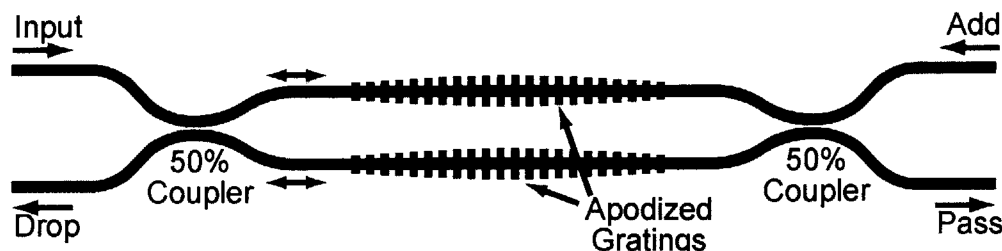

Figure 6.3: The integrated Mach-Zehender interferometer combines two 50% directional couplers with two identical Bragg gratings. This device serves as a WDM channel dropping filter by routing the reflected light from the gratings to the drop-port of the first coupler. All other channels pass through the grating region and are routed to the pass-port.

one or more modes whose field-profile magnitudes are, by definition, constant in **z**.

To analyze such a waveguide we begin with Maxwell's equations in an isotropic, source free medium, of permittivity ϵ and permeability μ_0.

$$\nabla \times \mathbf{E} = -\mu_0 \frac{\partial \mathbf{H}}{\partial t} \tag{6.1}$$

$$\nabla \times \mathbf{H} = \epsilon \frac{\partial \mathbf{E}}{\partial t} \tag{6.2}$$

$$\nabla \cdot (\epsilon \mathbf{E}) = 0 \tag{6.3}$$

$$\nabla \cdot \mathbf{H} = 0 \tag{6.4}$$

We assume the time dependence of all fields is described by $e^{j\omega t}$, where ω is the angular frequency.[1] Using equations 6.1, 6.2, and 6.3, we can derive the vector wave

[1]Throughout this thesis the same notation is used for real and complex vector fields. Thus $\mathbf{E}(x, y, z, t) = \mathrm{Re}\{\mathbf{E}(x, y, z)e^{j\omega t}\}$.

equation for **E**.

$$\nabla^2 \mathbf{E} + \nabla \left(\frac{1}{\epsilon} \nabla(\epsilon) \cdot \mathbf{E} \right) + \omega^2 \mu \epsilon \mathbf{E} = 0 \tag{6.5}$$

where $\epsilon = n^2 \epsilon_0$ can vary spatially.

Only two **E** or **H** field components are necessary to specify a solution to equation 6.5. Usually, it is most interesting to solve for the transverse components of the electric field. To do this it is convienient to express equation 6.5 as a function of the transverse field $\mathbf{E}_T$. We assume all field components evolve in **z** as $e^{-j\beta z}$ where β is the propagation constant characteristic of the solution. Factoring out the **z** component gives the transverse wave equation.

$$\nabla^2 \mathbf{E}_T + \nabla \left(\frac{1}{n^2} \nabla(n^2) \cdot \mathbf{E}_T \right) + n^2 k^2 \mathbf{E}_T = \beta^2 \mathbf{E}_T \tag{6.6}$$

We have expressed ϵ in terms of n^2 and introduced the free-space wavenumber, $k = \frac{\omega}{c}$. Equation 6.6 is a partial-differential eigenvalue equation with eigenvalues β_n and eigenfunctions $\mathbf{E}_T$.

Two simplifications of the vector wave equation are often employed in waveguide design. If we assume that the change in refractive index within the guiding structure is small, we can treat n as constant and equation 6.6 reduces to the scalar wave equation:

$$\left(\frac{\partial^2}{\partial x^2} + \frac{\partial^2}{\partial y^2} + n^2 k^2 \right) \phi(x, y) = \beta^2 \phi(x, y) \tag{6.7}$$

where $\phi(x, y)$ is the scalar field.

This equation does not differentiate between the quasi-TE and TM modes of the structure; as a result, it does not reveal any polarization dependent behavior. This is problematic for the high-index-contrast ridge waveguides addressed here. Alternatively, if one transverse-field component is much larger than the other, the approxi-

mate scalar eigenvalue equation for this component is given by

$$\frac{\partial}{\partial x}\left[\frac{1}{n^2}\frac{\partial n^2 E_x}{\partial x}\right]+\frac{\partial^2 E_x}{\partial y^2}+n^2k^2=\beta^2 E_x \tag{6.8}$$

for quasi-TE modes, or by

$$\frac{\partial^2 E_y}{\partial x^2}+\frac{\partial}{\partial y}\left[\frac{1}{n^2}\frac{\partial n^2 E_y}{\partial y}\right]+n^2k^2=\beta^2 E_y \tag{6.9}$$

for quasi-TM modes. These equations, the semi-vectorial eigenvalue equations, partially retain the vector nature of the field.

In practice, these equations are solved numerically by a number of different methods. Here we have chosen to solve the semi-vectorial equations using the finite-difference approach described by Stern [46] as detailed by Murphy [47]. Finite-difference techniques sample both the refractive-index profile and the mode's field profile over a discrete mesh of points.

The second derivatives of equations 6.8 and 6.9 are approximated by difference equations at each mesh point. This large set of equations can be couched as a single matrix-eigenvalue equation. Several techniques can be used to compute the desired eigenvalues and eigenvectors; following Murphy, we use the MATLAB *eigs* function.[48] We need only compute the few largest eigenvalues that correspond to physical modes; for single-mode waveguides only the largest eigenvalue needs to be determined. Figure 6.4 also shows the result of the semi-vectorial finite difference computation for the E_x field.

6.1.3 Contra-directional Coupled-Mode Theory

Adding a Bragg-grating to a uniform waveguide couples a forward propagating mode to its corresponding backward propagating mode for a narrow range of wavelengths

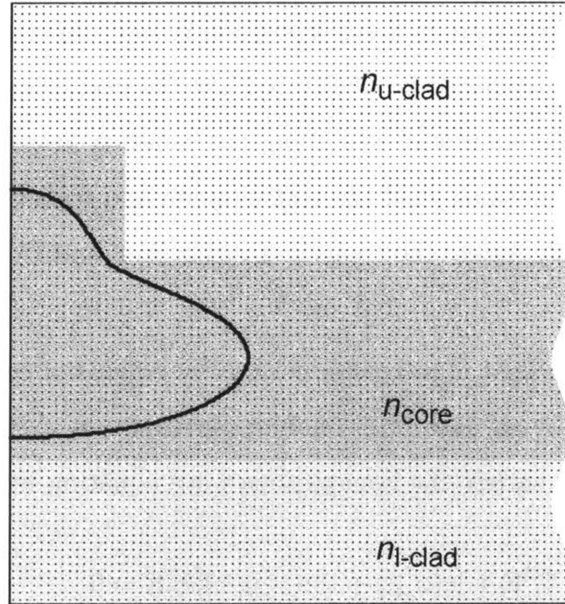

Figure 6.4: Refractive-index profile, finite-difference mesh points, and mode shape for a ridge waveguide. The mode's y-axis symmetry allows one to calculate only half the mode profile.

about the Bragg wavelength, λ_B, given by

$$\lambda_B = 2n_{\text{eff}}\Lambda \tag{6.10}$$

where $n_{\text{eff}} = \beta/k$ is the mode's effective index and Λ is the grating period. The rate of contra-directional coupling and the range of wavelengths effected are determined by the strength of the grating. The grating strength is determined by the refractive-index difference between the grating teeth and their surrounding material and by the overlap of the waveguide-mode with the grating region. In this section we seek to quantify the relationship between the physical waveguide-grating structure and its spectral response.

Once we determine the waveguide mode profile and its corresponding propagation constant, we need to quantify the effect of adding a grating. Coupled-mode theory treats the grating as a perturbation to the waveguide, and expands the fields of

the waveguide-grating structure as a superposition of the unperturbed waveguide's modes. When this mode expansion is substituted into the perturbed wave equation we obtain a set of differential equations describing the coupling between various modes. The solutions to these equations yield the transmission and reflection response of the structure. Here we closely follow the treatment of Coldren and Corzine.[49]

Consider a waveguide that is piecewise defined by regions of constant n and that has a grating described by an dielectric-constant perturbation, $\Delta\epsilon(x, y, z)$. The fields of such a structure must satisfy the homogenous wave equation with a perturbation,

$$\nabla^2\mathbf{E} + [\epsilon(x,y) + \Delta\epsilon(x,y,z)]k_0^2\mathbf{E} = 0. \tag{6.11}$$

For a waveguide supporting only a single mode for each polarization, we can express the fields of the perturbed waveguide as a superposition of the forward and backward traveling modes.

$$\mathbf{E}(x,y,z,t) = \mathbf{E}_T(x,y)\left[E_+(z)e^{j(wt-\beta z)} + E_-(z)e^{j(wt+\beta z)}\right] \tag{6.12}$$

where $\mathbf{E}_T$ is the transverse-mode profile and E_+ and E_- are the amplitudes of the forward and backward traveling modes. In fact, to form a complete basis set of modes we must include radiation modes as well as the waveguide modes. By neglecting radiation modes, our solutions will not account for grating induced loss in the structure.

Now we multiply equation 6.11 by $\mathbf{E}_T^*(x, y)$ and integrate over the waveguide cross section. At this point many authors disregard all terms involving second derivatives of the amplitude functions E_+ and E_-. This is a convienient simplification, but it has been shown to be unnecessary.[50] We obtain the exact coupled-mode equations regardless of whether we retain the second-derivative terms. In any case, we obtain

the following relationship

$$\frac{dE_+}{dz}e^{-j\beta z} - \frac{dE_-}{dz}e^{j\beta z} = -j\frac{k_0^2}{2\beta}\left[E_+e^{-j\beta z} + E_-e^{j\beta z}\right]\frac{\int\int \Delta\epsilon \mathbf{E}_T^*\mathbf{E}_T dxdy}{\int\int \mathbf{E}_T^*\mathbf{E}_T dxdy} \tag{6.13}$$

It is useful to expand the dielectric constant perturbation in terms of it's Fourier components in z. Thus,

$$\Delta\epsilon(x,y,z) = \sum_m \delta\epsilon_m(x,y)e^{-j2m\pi z} \tag{6.14}$$

where $\delta\epsilon_m$ is the mth Fourier coefficient. If we choose our waveguide-grating geometry appropriately the grating does not alter the propagation constants of the waveguide modes, and $\delta\epsilon_0 = 0$. We note from equations 6.13 and 6.14 that unless $m = \pm 1$, $\frac{dE_+}{dz}$ and $\frac{dE_-}{dz}$ will oscillate rapidly and there will be no net coupling of power between the modes. Said another way, unless the reflections from the grating teeth combine in phase, there will be little net reflection from the entire grating.

Equation 6.13 now simplifies into two coupled differential equations.

$$\frac{dE_+(z)}{dz} = -j\kappa_{+1}E_-(z)e^{j2\delta z} \tag{6.15}$$

$$\frac{dE_-(z)}{dz} = j\kappa_{-1}E_+(z)e^{j2\delta z} \tag{6.16}$$

Where the coupling coefficient, κ, determines the strength of coupling between the forward and backward propagating modes.

$$\kappa_{\pm 1} \equiv \frac{k_0^2}{2\beta}\frac{\int \delta\epsilon_{\pm 1}\mathbf{E}_T^*\mathbf{E}_T dA}{\int \mathbf{E}_T^*\mathbf{E}_T dA} \tag{6.17}$$

And the detuning parameter, $\delta = \beta - \pi/\Lambda$, defines how far the frequency of interest differs from the Bragg condition.

This formulation of the coupled mode equations makes sense intuitively. The

amplitude of the backward propagating wave increases at a rate proportional to the amplitude of the forward propagating wave. In addition, the rate of change is proportional to strength of the grating, κ, and is influenced by any deviation, δ, from the Bragg condition. However, to solve equations 6.15 and 6.16 it is useful to make the following change of variables

$$A_+(z) = E_+(z)e^{-j\beta z} \tag{6.18}$$

$$A_-(z) = E_-(z)e^{j\beta z} \tag{6.19}$$

Switching to matrix notation, we find that

$$\frac{d}{dz}\begin{bmatrix} A_+(z) \\ A_-(z) \end{bmatrix} = \begin{bmatrix} -j\delta & -j\kappa_{+1} \\ j\kappa_{-1} & j\delta \end{bmatrix}\begin{bmatrix} A_+(z) \\ A_-(z) \end{bmatrix} , \tag{6.20}$$

which has solutions

$$\begin{bmatrix} A_+(z) \\ A_-(z) \end{bmatrix} = \begin{bmatrix} \cosh(\gamma z) - j\frac{\delta}{\gamma}\sinh(\gamma z) & -j\frac{\kappa_{+1}}{\gamma}\sinh(\gamma z) \\ j\frac{\kappa_{-1}}{\gamma}\sinh(\gamma z) & \cosh(\gamma z) + j\frac{\delta}{\gamma}\sinh(\gamma z) \end{bmatrix}\begin{bmatrix} A_+(0) \\ A_-(0) \end{bmatrix}. \tag{6.21}$$

where $\gamma^2 = \kappa^2 - \delta^2$.[51] The transfer matrix in equation 6.21 is also the transfer matrix for the forward and backward propagating mode amplitudes provided the beginning and ending reference planes of the grating are placed such that $e^{j\beta_0 z} = 1$. This is easily accomplished when modeling the grating.

So we see that the coupled-mode equations emerge from the perturbed wave-equation when we expand the fields of the perturbed waveguide in terms of the unperturbed waveguide modes. The equations are simplified by expanding the perturbation in terms of its Fourier components, and noting that only the ± 1 components couple the lowest order forward and backward propagating modes. Finally, we have expressed the strength of this coupling in terms of a coupling coefficient, κ, that de-

pends on the index contrast of the grating and the mode-overlap with the grating region.

6.1.4 Uniform Grating Analysis

Calculating κ is key to applying the coupled-mode solutions to a real waveguide-grating structure. First, we calculate the unperturbed waveguide modes with the grating replaced by a uniform region of intermediate refractive index given by

$$n_{\text{grat}}^2 = \left[D\, n_{\text{core}}^2 + (1-D)\, n_{\text{clad}}^2\right]. \tag{6.22}$$

n_{grat} is the index assigned to the grating region and D is the grating duty cycle. Including the grating region in the initial mode calculation avoids the assumption that the grating does not alter the mode-profile and ensures that $\delta_{\epsilon_0} = 0$. Figure 6.5 shows the refractive-index and mode profiles for a rib waveguide with 50% duty cycle sidewall gratings.

Once the fields for a given mode have been determined one can calculate κ from equation 6.17. For a grating with rectangular teeth and a 50% duty cycle, the first Fourier component is given by

$$\delta\epsilon_1 = (n_{\text{core}}^2 - n_{\text{clad}}^2)/\pi \tag{6.23}$$

and κ simplifies to

$$\kappa_{\pm 1} = \frac{k_0^2}{2\pi\beta}(n_{\text{core}}^2 - n_{\text{clad}}^2)\Gamma \tag{6.24}$$

where

$$\Gamma = \frac{\int_{\text{grat}} |\mathbf{E}_T|^2 dA}{\int |\mathbf{E}_T|^2 dA} \tag{6.25}$$

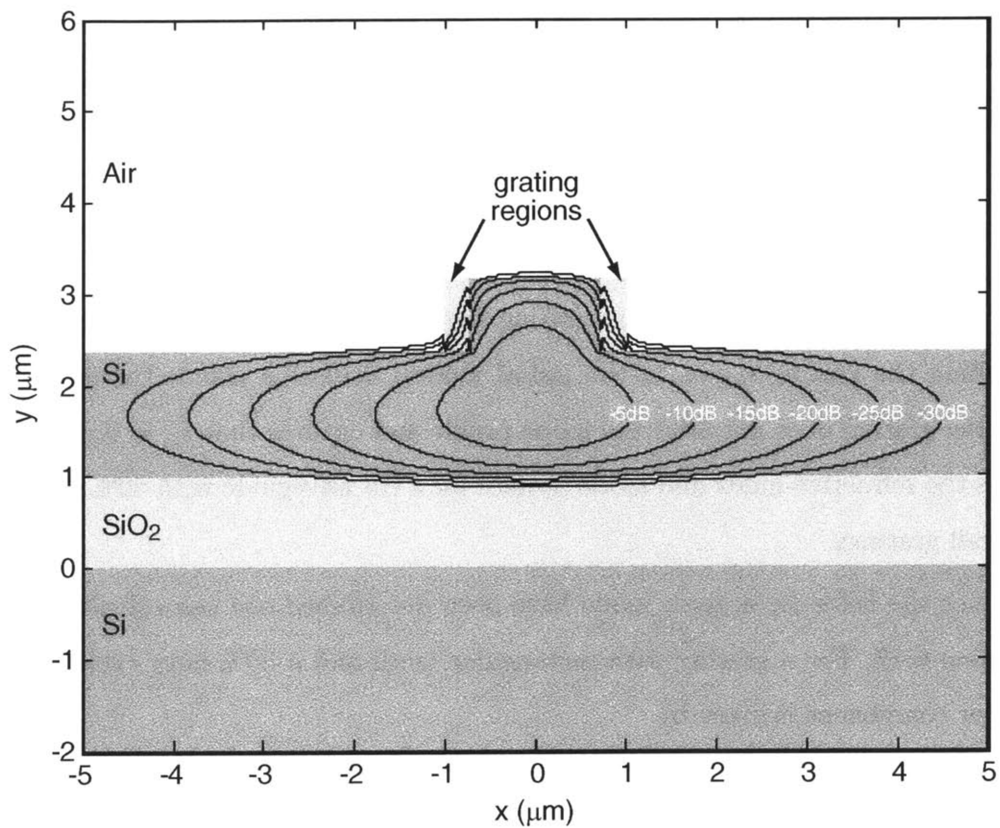

Figure 6.5: TE-mode profile of a silicon-on-insulator ridge waveguide with 50% duty-cycle grating regions. The gratings extend 300-nm on each side of the ridge

Γ, the mode-overlap integral, is the ratio of modal-power in the grating region to the total power in the mode. For the grating designs described here, the transverse electric field, $\mathbf{E}_T$ is approximated by the dominant component for each polarization, E_x for TE-modes, and E_y for TM modes.

Now that we know κ we can use equation 6.21 to calculate the reflection and transmission coefficients for a uniform grating. Suppose a forward traveling wave is incident on a grating lying in the region $0 < z < L$. The incident wave has amplitude 1 at $z = 0$, and there is no backward traveling wave at $z = L$. Thus, $A_+(0) = 1$, $A_-(0) = r$, $A_+(L) = t$, and $A_-(L) = 0$ in equation 6.21. Solving for the reflection and transmission coefficients, r and t, we find

$$r(\delta) = \frac{-j\frac{k_{-1}}{\gamma}\tanh(\gamma L)}{1 + j\frac{\delta}{\gamma}\tanh(\gamma L)} \tag{6.26}$$

$$t(\delta) = \frac{\operatorname{sech}(\gamma L)}{1 + j\frac{\delta}{\gamma}\tanh(\gamma L)} \tag{6.27}$$

These equations provide closed form solutions for the reflection and transmission coefficients of a uniform grating, but the transfer matrix itself, equation 6.21, is used to analyze non-uniform gratings.

6.1.5 Non-uniform Grating Analysis

Uniform gratings are useful for some applications, but their performance is insufficient for WDM channel add/drop filtering. Uniform gratings exhibit significant reflectivity outside the main stopband of the filter, and these side lobes in the reflection spectrum introduce cross-talk between WDM channels. For systems seeking to utilize 100, 50, or even 25GHz channel spacings, uniform gratings cannot provide adequate channel isolation.

The process of suppressing the side lobe levels in the reflection and transmission spectra is termed apodization. It is accomplished by gradually increasing and then

decreasing the grating strength along the length of the grating. In practice, this means gradually increasing and then decreasing the depth and or duty cycle of the grating teeth. There are several techniques available to model apodized gratings and non-uniform gratings in general.

The most intuitive technique divides a non-uniform grating into small segments where the grating strength, grating period, and propagation constant can be considered constant. The response of the non-uniform grating is calculated by multiplying the transmission matrices of the small uniform grating segments. Using the forward transmission matrix of equation 6.21 the non-uniform grating response is given by

$$\begin{bmatrix} t \\ 0 \end{bmatrix} = \mathbf{T}_N \mathbf{T}_{N-1} \cdots \mathbf{T}_1 \mathbf{T}_0 \begin{bmatrix} 1 \\ r \end{bmatrix} \tag{6.28}$$

where $\mathbf{T}_n$ is the transmission matrix for a uniform grating segment. Additional transmission matrices can be inserted to model intentional or erroneous phase shifts in the grating. The forward transmission matrix for a phase-shift $\Delta\phi$ is

$$\mathbf{T} = \begin{bmatrix} e^{-j\Delta\phi} & 0 \\ 0 & e^{j\Delta\phi} \end{bmatrix} \tag{6.29}$$

where the phase shift is given by

$$\Delta\phi = \beta\,\Delta z \tag{6.30}$$

While the transfer matrix method is an approximation for gratings with continuously varying parameters, gratings fabricated with computer aided design often change parameters in discrete steps determined by the system's design grid. The transfer matrix approach is particularly appropriate for these structures. Unlike calculations involving thin film stacks this technique does not use a separate transfer matrix for each grating tooth. Rather, the transfer matrices for uniform gratings as-

sume that the fields vary slowly over several gratings periods; as a result,the uniform segments must encompass a number of periods.

6.2 Silicon-on-insulator WDM Filter Design

Grating-based filters have been fabricated in a number of materials systems including III-V semiconductor[52], doped silica[47], silicon oxy-nitride[53, 54], and SiN.[55] Like many of these materials silicon exhibits low absorption for wavelengths near 1550 nm. The availability of high-quality silicon-on-insulator (SOI) substrates makes silicon an interesting material system for integrated-optical devices. This section details the design process for a silicon-on-insulator WDM filter. The design process translates a specified reflection spectrum into a suitable waveguide geometry with apodized sidewall gratings.

6.2.1 Silicon Based Optical Devices

Silicon's material properties, low loss at 1550nm, single crystal films, and low material birefringence, make SOI an attractive platform for integrated optics. In addition, materials processing techniques are well established for silicon, and many silicon-based electronic devices can be integrated with optical devices. The high index-contrast between silicon and silicon-dioxide supports a range of waveguide geometries allowing one to optimize device size and loss. Some optical components realized in SOI include modulators[56], switches[57], gratings[58, 59], ring resonators[60], and photonic band-gap structures[61].

The atomic structure of crystalline silicon yields an electronic bandgap of 1.1eV. As a result, light in the low fiber-loss widow near 1550 nm, or ≈ 0.8 eV, is not strongly absorbed in silicon. The engineering demands of the semiconductor-electronics industry have made silicon available with high purity and excellent crystalline quality. As a result, other forms of loss (free-carrier absorption and Raleigh scattering) are min-

imized and the refractive index can be highly predicatable and repeatable.

In addition to the high-index core, silicon integrated optics require lower-index cladding layers. Silicon-on-insulator (SOI) substrates introduce a dielectric layer, typically silicon-dioxide, below the critical silicon layer. For semiconductor devices, the SiO_2 layer provides electrical isolation between the transistors and the bulk-silicon substrate. For integrated optics, this layer forms the lower cladding. Another dielectric layer can be deposited for the upper cladding, or one can simply use air.

Most SOI substrates are produced by one of two approaches. In the first approach oxygen is ion-implanted to the desired depth below the silicon. Implantation damage is subsequently removed by annealing. The second technique, more common for thicker silicon and silicon-dioxide layers found in integrated optics, utilizes wafer bonding and selective etching. Companies following this approach include SOITEC, SA; SiGen, Inc.; SiBond, LLC; and Canon. As the example most relevant to this work, we describe Canon's ELTRAN (Epitaxial Layer Transfer) process.[62]

Canon's ELTRAN process begins with a seed Si wafer up to 300mm in diameter. Two layers of porous silicon are formed on this wafer with different porosities. The device silicon layer is grown epitaxially on the porous layer, and then thermally oxidized to form the insulating SiO_2 layer. To complete the process this stack is bonded to a handle Si wafer and split off using a water jet aimed at the porous layers. The porous layer is selectively etched away, and the final wafer is annealed in a hydrogen atmosphere to reduce roughness.[63] This prevents material loss that would normally be associated with chemical-mechanical polishing. The seed wafers can be reused several times. Figure 6.6 illustrates this process.

6.2.2 Filter Specifications

For a grating-based add/drop filter to be useful for wavelength-division multiplexing it must meet a number of specifications. Clearly, the device must not introduce excessive loss in either the dropped or passed channels. In addition, residual light on

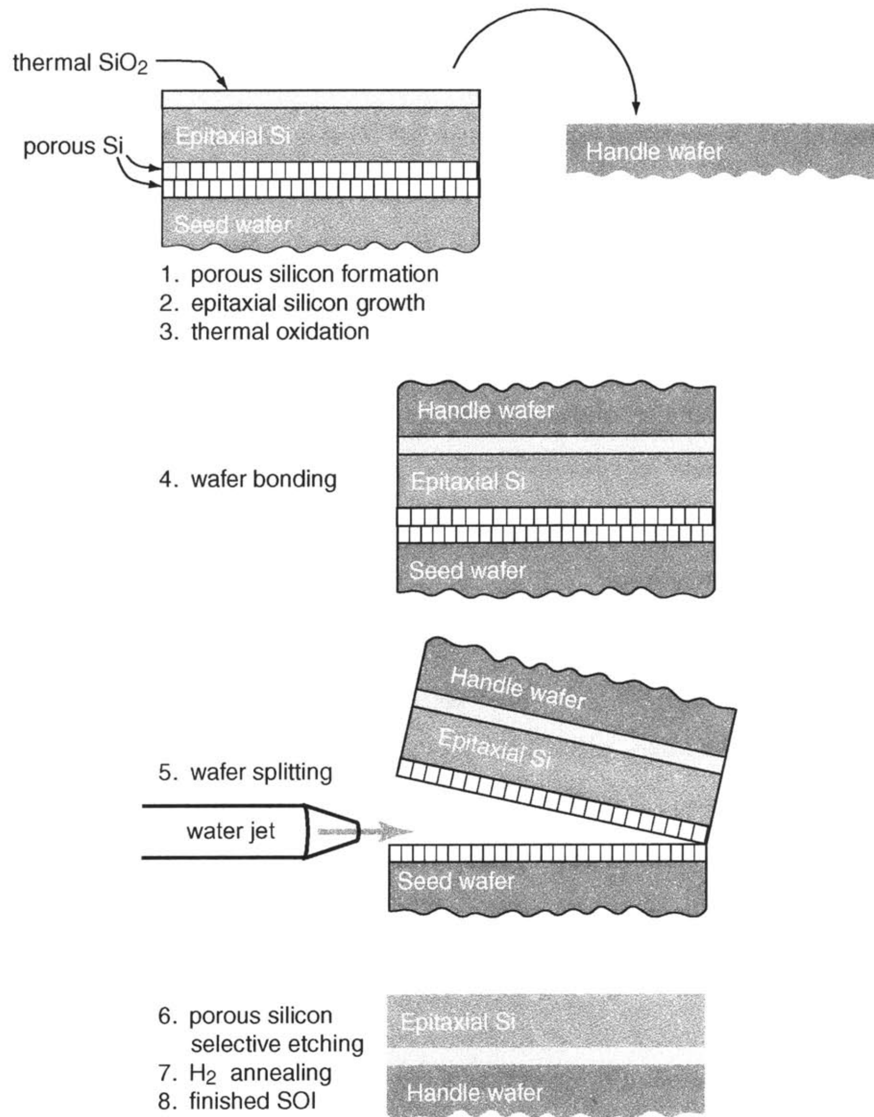

Figure 6.6: Canon's Epitaxial Layer Transfer (ELTRAN)process. Two layers of porous silicon are formed with different porosities. Epitaxial Si and thermal SiO_2 are formed on top of the porous Si. After bonding to a handle wafer, the seed wafer is removed by aiming a water jet at the porous layers. The SOI wafer is completed by selectively etching the porous Si and annealing.

the primary bus from the dropped channel must be sufficiently week to not interfere with an added channel. It is equally important that light from passed channels not couple into the dropped port. Excessive cross-talk between the dropped and passed channels introduces transmission errors.

Commercial WDM systems currently use 2.5 Gbit/s and 10Gbit/s channels spaced 50, 100, or 200 GHz apart. For most applications these channels fall in the "c-band," wavelengths from 1530.33nm to 1569.59nm. In order to make use of existing fiber, one would like to maximize spectral efficiency, the ratio of data rate per channel to channel spacing. Spectral efficiency improves with both denser channel spacing, e.g. 10Gbit/s at 25 GHz spacing, or higher data-rates, e.g. 40Gbit/s at 100 GHz spacing. Which approach gains wider use will be determined not only by the technical capabilities, but also by component costs[2] and by the way in which service providers apportion bandwidth to their customers.[3]

Grating-based add/drop filters can be designed for any physically realizable combination of data-rate and channel-spacing. Whether one chooses smaller channel-spacings or higher data-rates, filter induced cross-talk becomes increasingly problematic. To address this issue, the reflection bandwidth of the filter is typically specified at several power levels. For example, Telcordia specifies minimum bandwidths at -1 dB and -3 dB and maximum bandwidths at -20dB and -30dB[64]. This ensures that the filter response is sharp enough to completely drop one channel without affecting others.

Although grating-based add/drop filters can provide a useful replacement for current WDM technology, the devices described here are designed for a next generation system operating at 40Gbit/s data-rates and 100GHz channel spacing. Such systems

[2]Low channel-count high data-rate systems generally require fewer, but more expensive, components. Likewise, high channel-count, low data-rate systems require a greater number of components that may be somewhat less expensive.

[3]If a service provider wishes to sell discrete WDM channels to its customers, then lower data-rate system provide the flexibility to sell bandwidth in smaller increments. On the other hand, high data-rate channels can be further divided by electronic time-division multiplexing to provide reconfigurable bandwidth slices to customers.

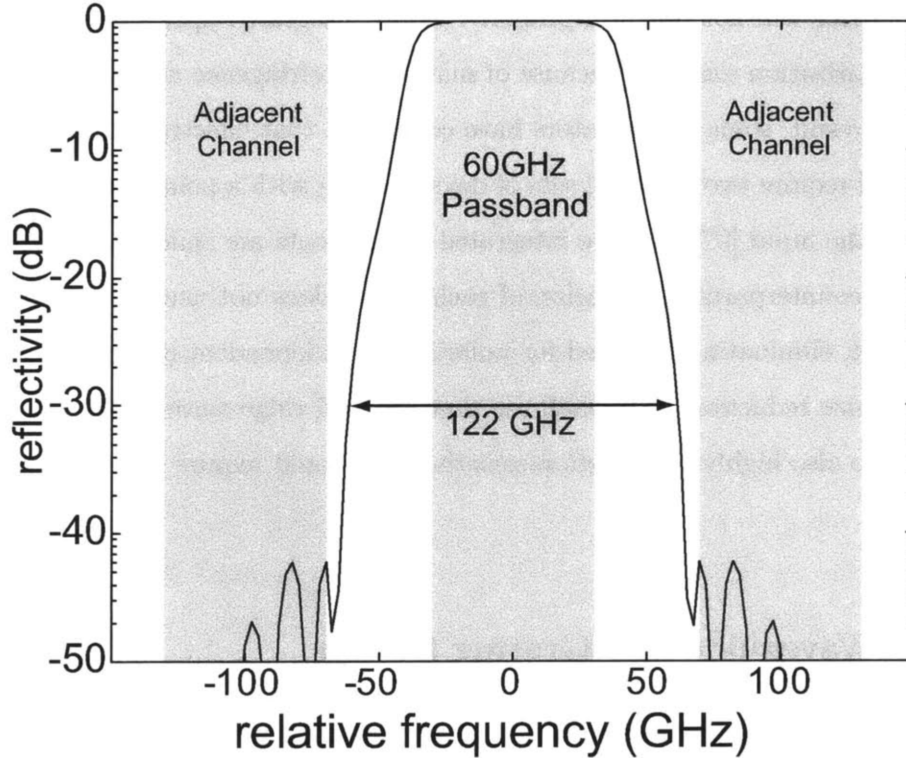

Figure 6.7: WDM filter specifications and calculated response for 40Gbit/s data rate and 100 GHz channel spacing. The minimum and maximum bandwidths are shown for -0.5dB and -30dB respectively. Reflections within other channels is reduced below -40dB. The calculated response is shown for a SOI sidewall-grating device with $\kappa = 28cm^{-1}$, a length of 3.0mm, and a raised-cosine apodization function.

are not yet commercially available, but have been demonstrated for 40 channels (1.6 Tbit/s total data-rate) over 480km of optical-fiber,[65] and 25 channels (1 Tbit/s total data-rate) over 90 km of fiber[66]. The filter described here was required to have a minimum bandwidth of 60GHz at -0.5dB and a maximum bandwidth of 130 GHz at -30dB. In addition, reflection of all other channels is less than -30dB. Figure 6.7 shows these specifications along with the calculated filter response for the final design (see section 6.2.3).

Typically, a WDM filter's loss, center frequency, and channel isolation must be specified for each polarization. If these parameters are too highly polarization sensi-

tive the device will not function properly. Many integrated optical components are, in fact, polarization sensitive because of material birefringence and waveguide geometry. As a result, some investigators have concluded that effective integrated-optical devices will require two identical sets of devices along with a polarization splitter and rotator at the input.[67] Because integrated components are small compared to their bulk-optic counterparts, duplication of each device does not usually present a problem. In fact, eliminating the need for polarization independent design paves the way to further size reduction.[4] We shall see that the SOI ridge waveguides with sidewall gratings are also highly polarization sensitive and would require the duplicate device approach.

6.2.3 Waveguide and Grating Design

To realize the filter response described in section 6.2.2 we must first choose a suitable waveguide design for the input, output, and grating region. The ideal waveguide geometry supports only one mode, maximizes coupling efficiency, and minimizes propagation loss. In addition, the waveguide design must provide adequate grating strength and limit grating-assisted coupling between guided modes and slab modes. The effective-index of the selected waveguide determines the grating period, and the specified filter response determines the grating apodization function, $\kappa(z)$. The grating and waveguide dimensions are chosen to provide the desired variation of κ without altering the mode's effective-index.

The high refractive-index contrast between silicon ($n_{Si} = 3.48$ at 1550 nm) and silicon dioxide ($n_{SiO_2} = 1.46$) dictates a maximum single-mode slab-waveguide thickness of about 200 nm. Channel waveguides must be similarly constrained in at least

[4] The smallest waveguides with the tightest bend radii are usually based on thin (about 200nm) and wide (about 5 μm) high index contrast (silicon/air) structures that have large geometrical birefringence. The loss in these structures is reduced because the top and bottom surfaces are epitaxially defined while the rough edges, which are far from the high electric field region, are lithographically defined.

one dimension. Such structures offer unmatched miniaturization, but they can exhibit high fiber-coupling and propagation loss. Alternatively, ridge waveguides remain single mode with larger mode cross-sections. Ridge waveguides offer improved input-coupling efficiency because the larger mode-size better matches that of an optical-fiber. Large cross-section ridge-waveguides also reduce propagation losses because of the reduced mode-overlap with rougher etched surfaces. Both Schmidtchen et al. and Rickman et al. have fabricated single-mode SOI waveguides with dimensions of several microns and losses as low at 0.5 dB/cm.[68, 69].

Multi-mode waveguides are unsuitable for grating based devices because each mode interacts differently with the grating region. The modes' differing propagation constants lead to different center stopband wavelengths, while the modes' differing field-profiles lead to different grating strengths. A multi-mode waveguide-grating device cannot serve as an effective narrow-band filter. As a result, it is helpful to have a simple criteria for determining if a waveguide is single-mode, and a common starting point is the effective-index method (EIM). While this method is not sufficiently accurate for grating design, Pogossian has shown, using Rickman's experimental data [68], that the EIM provides a conservative bound for single-mode ridge-waveguide design.[70]

Because the effective-index method has been well described in several texts [49], only a brief summary is given here. The EIM divides a two-dimensional waveguide into several, usually three, one-dimensional slab waveguides. Figure 6.8 shows a ridge waveguide subdivided in this way. To find the overall propagation constant of the 2D-waveguide we first find the propagation constants of the three constituent slab waveguides. The propagation constant of the 2D-waveguide is approximately the propagation constant of the slab-waveguide formed by layers with the previously calculated effective-indices.

For a ridge waveguide whose thickness, H, would allow several slab modes, proper choice of the ridge width, w, and ridge height, rh, will provide single-mode opera-

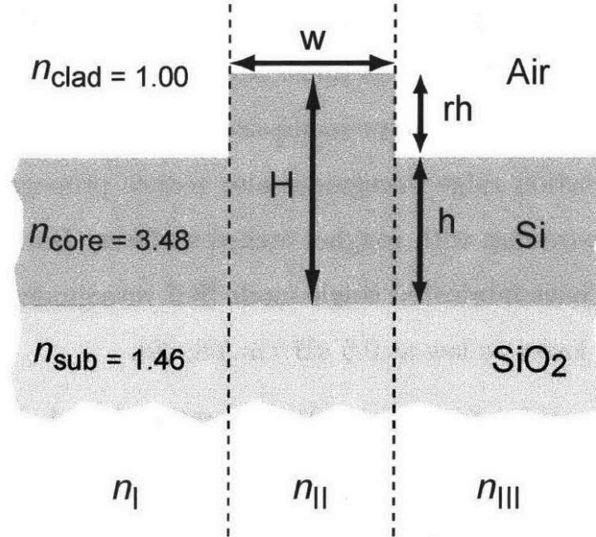

Figure 6.8: SOI ridge waveguide refractive-index profile with divisions for effective-index method.

tion. As Pogossian [70] shows, the EIM produces two criteria for the ridge waveguide single-mode condition. First, the effective-indices of the fundamental-modes of the three constituent slab waveguides must produce a single-mode "effective" slab guide. Secondly, the effective-indices of the higher order slab-modes for the ridge region, height H, must be smaller than the effective-index of the fundamental mode in the adjacent slab-regions, height h. Pogossian uses these two criteria to derive an approximate, but conservative, bound on the single-mode condition for a ridge waveguide.

$$t < \frac{r}{(1 - r^2)^{1/2}} \tag{6.31}$$

where

$$
\begin{aligned}
t &= w_{eff}/H_{eff}, \\
r &= h_{eff}/H_{eff} < 0.5, \\
h_{eff} &= h + q, \\
H_{eff} &= H + q, \\
w_{eff} &= w + 2\gamma_{\text{clad}}/\left[k(n_{\text{core}}^2 - n_{\text{clad}}^2)^{1/2}\right], \\
q &= \gamma_{\text{clad}}/\left[k(n_{\text{core}}^2 - n_{\text{clad}}^2)^{1/2}\right] + \gamma_{\text{sub}}/\left[k(n_{\text{core}}^2 - n_{\text{sub}}^2)^{1/2}\right]
\end{aligned}
$$

and where

$$
\begin{aligned}
&\gamma_{\text{clad}} = \gamma_{\text{sub}} = 1 && \text{for TE modes, and} \\
&\left.\begin{aligned}\gamma_{\text{clad}} &= (n_{\text{clad}}/n_{\text{core}})^2 \\ \gamma_{\text{sub}} &= (n_{\text{sub}}/n_{\text{core}})^2\end{aligned}\right\} && \text{for TM modes.}
\end{aligned}
$$

For a given set of refractive indices, n_{clad}, n_{core}, and n_{sub}, we can evaluate the single-mode condition in terms of the ratio's w/H and h/H. Figure 6.9 plots the EIM-based single-mode condition for a silicon-on-insulator ridge waveguide. This plot serves as an excellent guide for initial waveguide geometry selection, but single-mode propagation is not the only constraint.

For efficient fiber coupling, one would normally target a silicon-layer thickness and rib width comparable to the fiber's mode size, $\approx 9\mu$m . However, reasonably sized gratings placed in such large waveguides do not provide adequate grating strength for the desired filters. To minimize coupling and propagation loss, we choose the largest cross-section waveguide that provides sufficient grating strength for the filter in question. It was found that an initial silicon thickness of $H = 2.2\mu m$, a ridge height of $rh = 0.8\mu m$, and a ridge width of $w = 1.6\mu m$ provide sufficient grating strength in a single-mode waveguide.

While a properly designed rib waveguide supports only a single bound mode, there

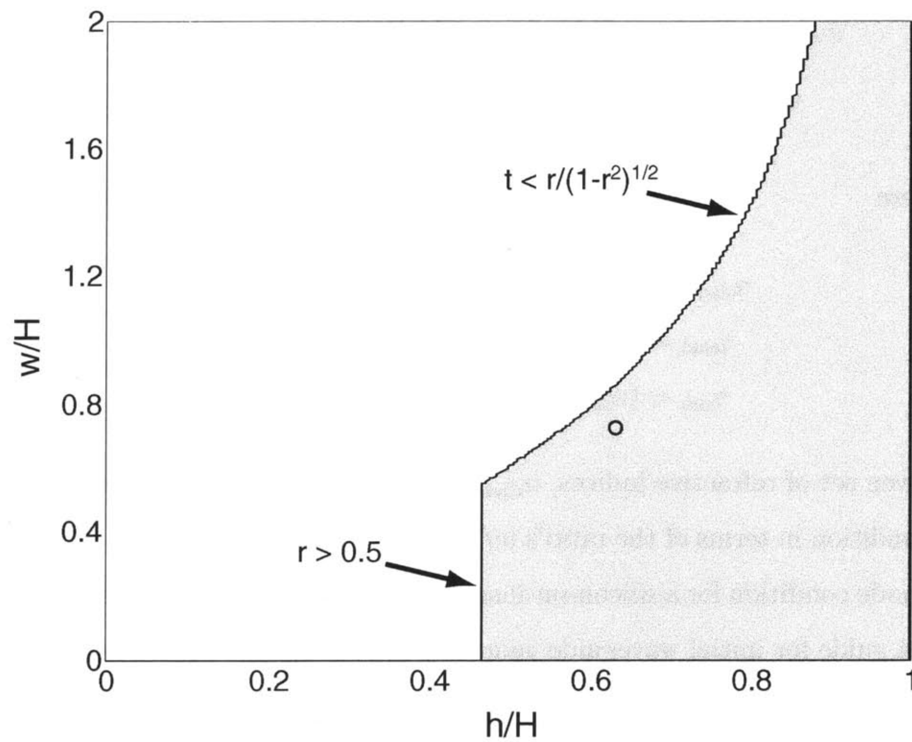

Figure 6.9: Plot of the EIM-based single-mode condition for a SOI ridge waveguide. The shaded region indicates geometries which support only a single bound mode. The circle indicates the design point for the waveguide described in section 6.2.3.

exist higher order states, so called leaky "modes", that can propagate for significant distances along the waveguide. The introduction of a grating into the waveguide can couple the fundamental forward mode to backward-propagating leaky modes. Previous experiments have shown that these modes are approximately the slab modes of the structure in the absence of the rib.[58] As expected, efficient coupling between these modes occurs when the grating k-vector is approximately the difference between the forward and backward mode's k-vectors. By taking this effect into consideration when designing a waveguide-grating structure we can reduce transmission losses on the short-wavelength side of the spectrum.

Murphy et al. illustrated this effect by plotting the dispersion relations for the forward and backward propagating slab modes.[58] Wavelengths with both desirable (fundamental forward to fundamental backward) and undesirable (fundamental forward to higher-order backward) mode coupling can be easily identified. Figure 6.10 shows the dispersion relations for the first four TE slab modes of a 1.4 μm thick SiO_2-Si-Air structure. A 224.9-nm-period grating introduces the illustrated coupling between the lowest-order forward mode and backward modes. The coupling near 1550 nm performs the filter function, while the coupling near 1524 nm is undesirable. Nevertheless, this design eliminates extraneous coupling within the communications c-band.

A final design was chosen that allows adequate grating strength and minimizes extraneous coupling. Specifically, the silicon slab region is 1.4 μm thick, while the rib region is 2.2 μm thick. The rib is 1.6 μm wide in regions with no grating. Given these parameters, we determine the propagation constant for the fundamental TE mode using the semi-vectorial eigenvector approach described in section 6.1.2. The propagation constant is predicted to be $1.3969 \times 10^5 cm^{-1}$ ($n_{\text{eff}} = 3.446$). Thus we choose a grating period of 224.9 nm to center the filter response at 1550-nm free-space wavelength.

A number of apodization functions will satisfy the filter requirements for dense

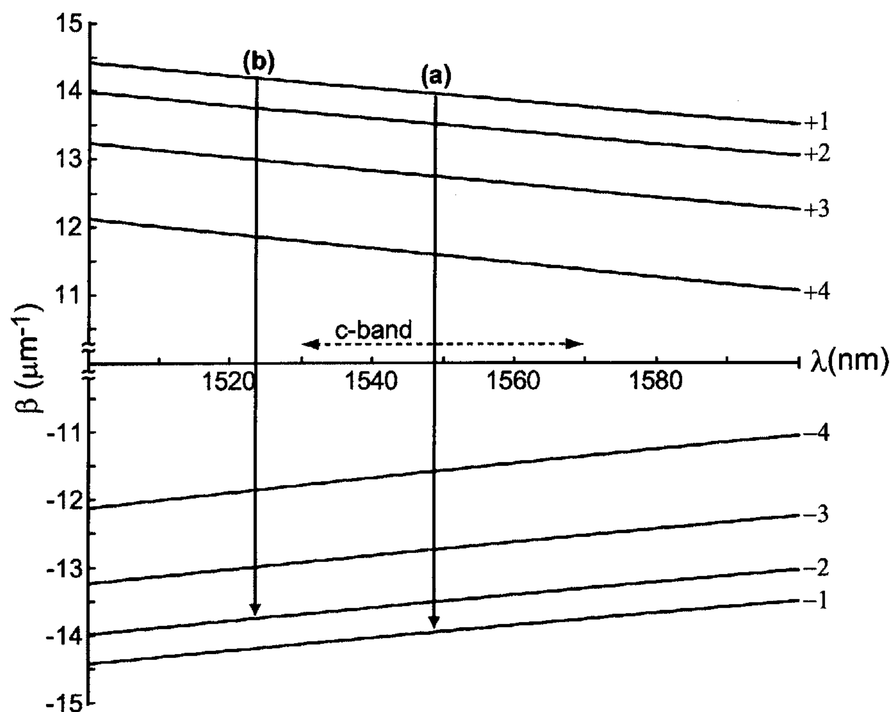

Figure 6.10: Dispersion relation for the first four TE slab modes of a 1.4 μm SiO_2-Si-Air waveguide. A 224.9 nm period grating couples both the first forward mode (+1) to first backward mode (-1), arrow **(a)**, and the first forward mode (+1) to the second backward mode (-2), arrow **(b)**.

WDM. Wiessman et al. even developed an optimized apodization function based on a genetic algorithm.[54] For our initial demonstration of apodized sidewall gratings we chose to use a simple raised cosine apodization profile.

$$\kappa(z) = \kappa_0 \cos^2(\frac{\pi z}{L}) \tag{6.32}$$

Less strongly apodized devices may be able to achieve adequate performance with slightly shorter grating lengths. This apodization profile must be achieved without altering the propagation constant of the waveguide. Otherwise, one would introduce chirp as well as apodization. In order to accomplish this we must adjust the waveguide and grating dimensions simultaneously.

Figure 6.5 shows the refractive index profile of a SOI ridge waveguide with sidewall gratings. The grating regions are represented by the mean refractive index of the core (silicon) and cladding (air). Using the geometry described above, an array of waveguide and grating widths were analyzed using a semi-vectorial mode solver. The grating's duty-cycle was set to be 50%, and only the quasi-TE mode was considered. The resulting map of n_{eff} and κ over these two parameters allowed us to design the waveguide grating structure.

Figure 6.11 shows contours of constant n_{eff} and κ. By selecting waveguide and grating dimensions along one n_{eff} contour we can obtain any required κ without changing n_{eff}. Figure 6.12 shows the waveguide width and the extent of the grating along a 3-mm long waveguide. It is clear from this diagram, as well as figure 6.11, that the grating strength and n_{eff} are non-linear function of grating depth. As a result, designing a structure based on a single mode-profile calculation would introduce large errors. It is important to note that this design differs from the fabricated filter (shown in figure 6.17). Unfortunately, the fabricated filter was designed by incorrectly modeling the grating as a region of mean refractive index, as opposed to mean dielectric constant. As a result, the calculated peak grating strength increases from 28 cm^{-1} to 38 cm^{-1}, and the apodization profile is no longer a simple raised-cosine function.

6.2.4 Grating-Phase Tolerances

After designing the waveguide-grating structure, we wish to assess the effect of phase errors on device performance. This topic has been investigated elsewhere with respect to both fiber[71, 72, 73, 74] and integrated Bragg-gratings.[23, 75] We model such errors numerically by introducing deterministic or stochastic phase shifts, equation 6.29, into the device's concatenated transfer matrix, equation 6.28. If one wished to perform a full yield analysis, specifications could be placed on the center frequency, bandwidth, cross talk in adjacent channels, and spectrum-wide cross talk. Then one could perform simulations with typical error locations and magnitudes to see how

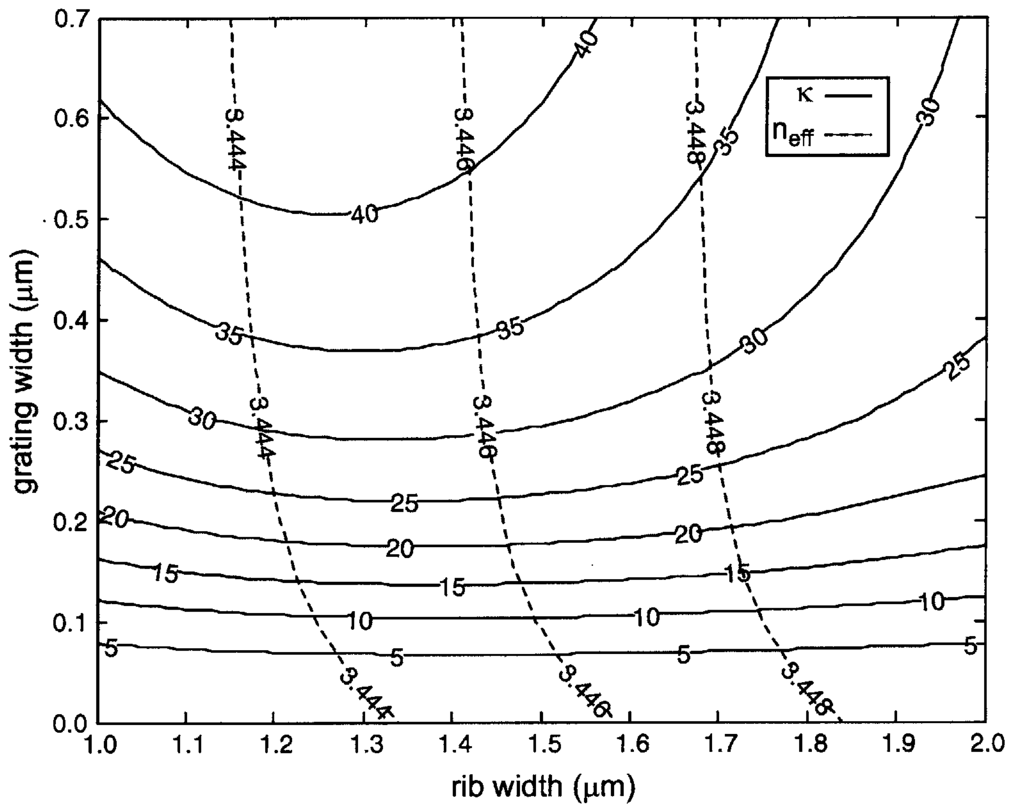

Figure 6.11: Contours of constant κ and n_{eff} for range of waveguide and grating widths. The ridge height is fixed at 0.8μm and the silicon slab thickness is 1.4μm .

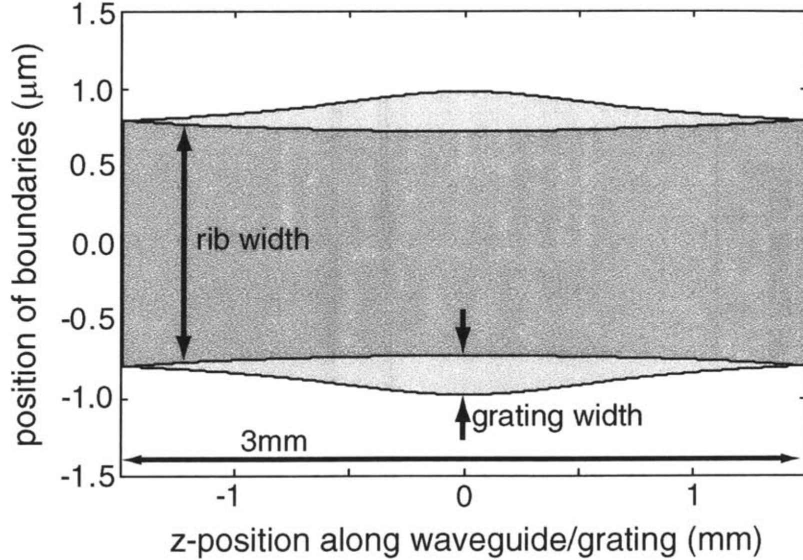

Figure 6.12: Inner and outer edges of the waveguide-grating structure. The dark shaded area represents the waveguide core, while the lighter area represents the grating region. Note that the x- and y-axes are scaled very differently.

many devices met these specification. Here we provide illustrative examples of the negative impact of common phase errors on device performance.

First let us consider deterministic phase errors at regularly spaced intervals. These errors are typical of e-beam written gratings when the deflection field is not well calibrated to the stage movement. When this is the case, we observe sidebands in the reflection spectrum at $\pm\lambda^2/(2n_{\text{eff}}F)$[76] from the central peak, where F is the field size. Figure 6.13(**a**) shows a calculated reflection spectrum based on 5-nm stitching errors every 71.5 μm, the field size used in fabricating the devices. The spurious reflection peaks are clearly visible at $\approx \pm 600GHz$. In addition, the stopband is shifted to lower frequencies.

In practice, placement errors have deterministic and stochastic components. Once again let us consider e-beam-exposed gratings with errors at the field boundaries, but now let the stitching errors have zero mean and standard deviation σ_{st}. This implies that each field is randomly placed with standard deviation $\sigma_{st}/\sqrt{2}$ with respect

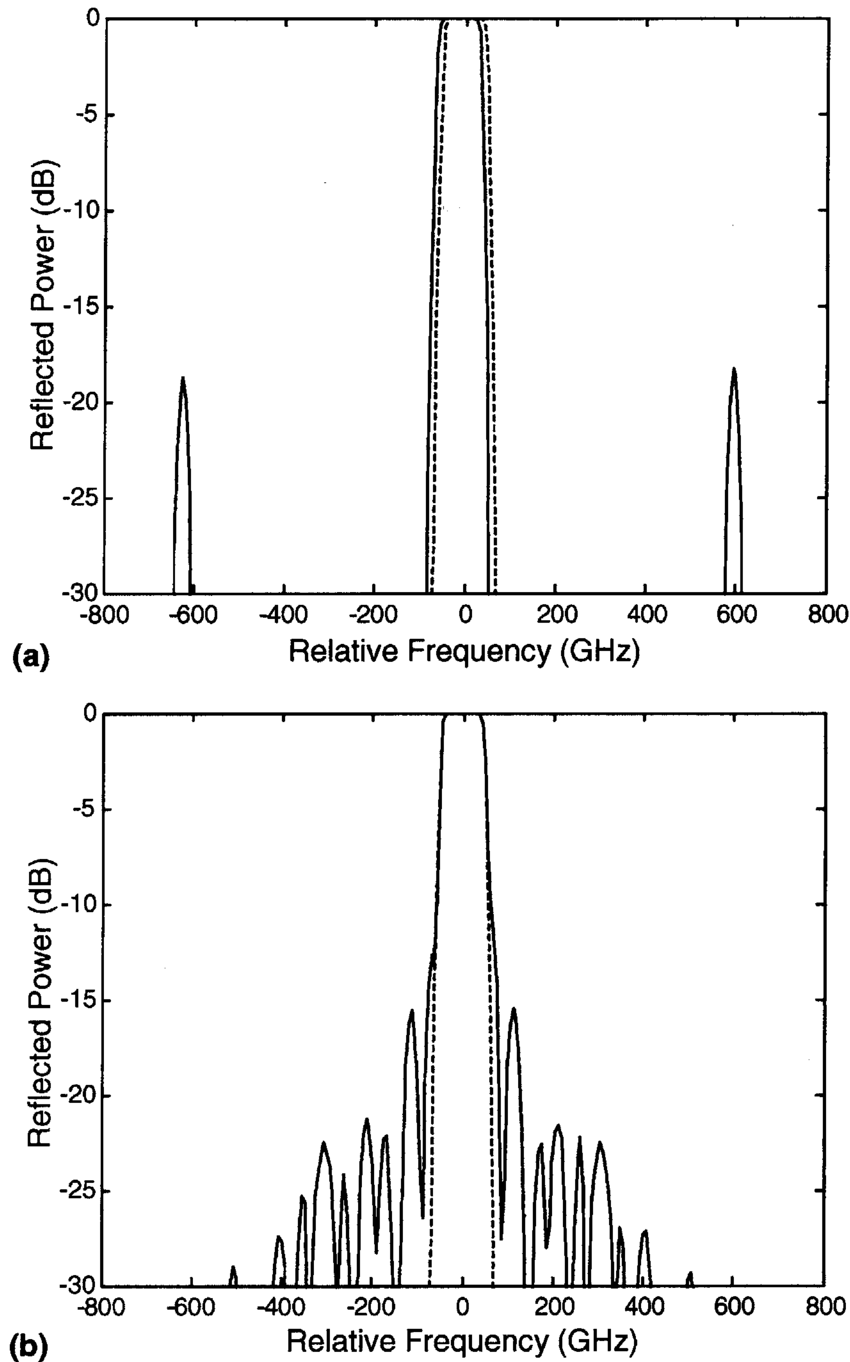

Figure 6.13: Deterministic and stochastic errors in an apodized SOI Bragg-grating filter. (**a**) Simulated reflection spectrum with deterministic 5-nm errors at each field boundary (71.5-μm spacing). (**b**) Sample simulated reflection spectrum with stochastic errors, $\sigma = 5$ nm, at each field boundary, but with no accumulated phase error. Dashed lines indicate ideal spectra in each case.

to its desired position. One could also model random stitching errors, as opposed to field placement errors, but this would introduce a random walk in the grating phase. This is not generally the case with e-beam-exposed gratings. Figure 6.13(**b**) shows a sample reflection spectrum calculated with $\sigma_{\mathrm{st}} = 5$ nm. The random errors introduce undesirable reflections near the central peak, effectively broadening the filter bandwidth. If one seeks to suppress spurious reflections below 30 dB across the entire WDM spectrum, neither deterministic nor random errors of this magnitude are permissable.

6.3 SOI WDM Filter Fabrication

The SOI WDM filter design presented here has two advantages that greatly simplify fabrication. First, the SOI rib waveguide structure requires no upper-cladding. InP channel waveguides require single-crystal upper cladding to be epitaxially grown on an etched surface. The high temperature deposition of doped silica cladding often deforms the grating even if the waveguide survives.[47] Other materials suffer from difficulty in filling the etched gratings with the upper cladding material.[53]

The sidewall grating design also offers several benefits for fabrication. Exposing the waveguide and grating in the same mask level eliminates the need to precisely align the waveguide to the grating. This is particularly important for apodized devices where the grating teeth cannot extend across the entire waveguide. Moreover, the sidewall gratings avoid the need to change the grating duty cycle along the length of the guide. If the duty cycle is used to apodize the grating, the degree of apodization is limited by the smallest feature one can expose. One must pattern 20 nm features to achieve a 10% duty cycle in silicon.

Additionally sidewall gratings allow coupling coefficients at least twice as large as gratings at only one interface. In the case of rib waveguides the increase in grating strength is even greater. The sidewall grating design exhibits one drawback. Sidewall

gratings typically require higher aspect ratio reactive-ion etching. For example, to fabricate a 200nm period, 200nm deep grating in the top of a 1μm waveguide requires an aspect ratio of 2:1. However, if the grating is in the side of the waveguide an aspect ratio of 10:1 is necessary.

Fabrication of the sidewall grating devices required four main processes. The fiducial gratings for SPLEBL were be patterned on the SOI substrate by x-ray lithography. Then the waveguide-grating structure was exposed with e-beam lithography. The waveguide rib and sidewall gratings were formed by reactive ion etching the silicon layer. Finally, the device was diced and polished in preparation for optical testing.

6.3.1 Fiducial Grid Patterning

An x-ray lithography mask with isolated 244.4-nm-period fiducial gratings was previously fabricated by interference lithography specifically for integrated-optical devices.[52] The x-ray mask was formed a 1-μm -thick silicon-rich silicon-nitride membrane with 200 nm of electroplated gold as an absorber. The fiducial gratings were isolated into stripes, so as to occupy only the edges of the e-beam deflection field. This pattern was proximity printed in 200 nm of PMMA on an SOI substrate using a Cu_L line electron-bombardment x-ray source. The exposure required 21 hours with a source to substrate distance of 23.3 cm. The PMMA was developed for 30 seconds in 2:1 IPA:MiBK at 21° C. After development, 30 nm of tungsten was electron-beam evaporated and lifted off by dissolving the PMMA in n-methyl pyrrollidone (NMP) at 80°C.

6.3.2 SPLEBL Exposure

The SOI substrate and tungsten fiducial gratings were spin coated with 125 nm of hydrogen silsesquioxane (HSQ, commercially available as FOx from Dow Corning Corporation, Midland, Mi.). Although intended as a low-dielectric-constant material

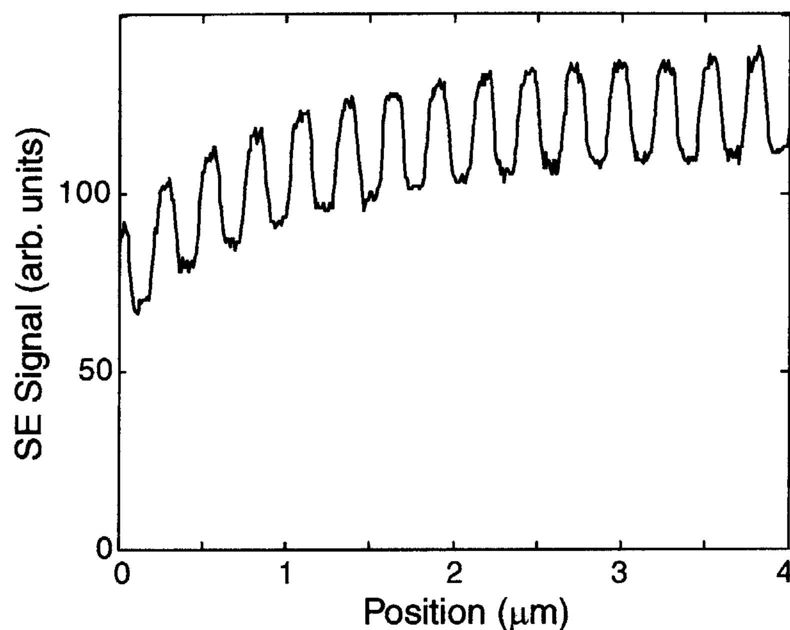

Figure 6.14: Secondary electron signal from W-fiducial grating under 125nm of HSQ resist. The primary electron energy was 30 keV.

for integrated circuits, HSQ can also serve as a high resolution (<10 nm) negative-tone e-beam resist.[77, 78] Appendix A provides more detail on the processing and exposure of HSQ. After spin coating, the HSQ was pre-baked on hot plates for 120 seconds at 150°C and for 120 seconds at 220°C. A standard silicon monitor wafer was processed simultaneously to verify the pattern fidelity and etch quality.

Figure 6.14 shows the secondary-electron signal obtained from the tungsten fiducial grating under 125nm of HSQ with a 30kV electron beam. The range of secondary electrons in most glass-like materials is no more than a few nanometers, so one might expect that imaging the W fiducials under the HSQ layer would be difficult. However, the backscattering efficiency of W is approximately twice that of Si at 30kV [25], and the increased number of backscattered electrons creates additional secondary electrons at the HSQ surface. In this way one can form a secondary-electron image of a buried pattern based on the difference in backscatter efficiency. Figure 6.15 illustrates this process.

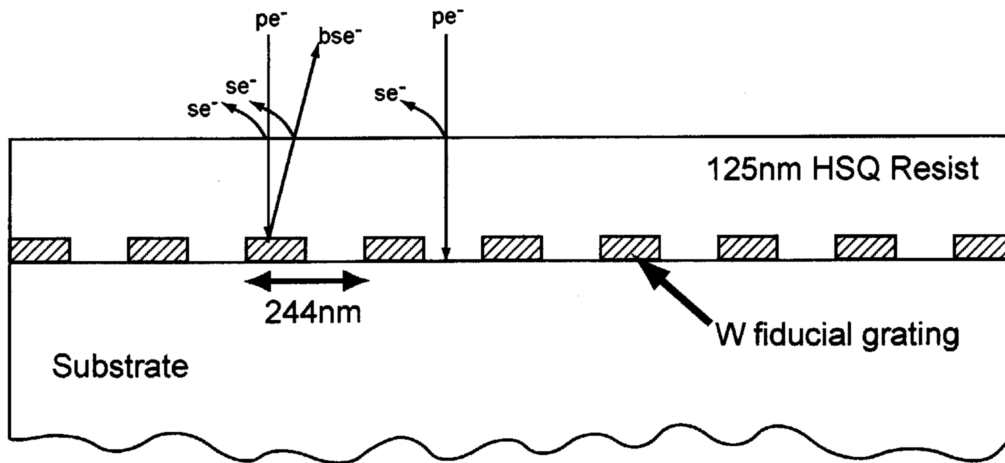

Figure 6.15: Primary electrons (pe-) incident on HSQ with the underlying W fiducials are more likely to backscatter and produce additional low-energy secondary electrons (se-) than primary electrons incident on HSQ with only silicon beneath it. In this way we obtain contrast in a secondary-electron image even with the W buried under the HSQ.

The fine grating period and high signal-to-noise ratio allow precise phase-locking. The pattern was exposed using a 89.9 μm field size (400 device-grating periods), but no patterns were placed in the right-most 18 μm of the field to avoid previously measured intra-field distortion.[45] The beam energy was 30 keV, and the dose was 550 μC/cm^2. As detailed in chapter 3, we observed a deflection-dependent field-scaling error after phase-locking to the fiducial grating. The x-scaling of the field was found to vary linearly with the beam-deflection velocity in the y-direction. This error was highly reproducible, and was compensated by a velocity-dependent scale correction.

After exposure, the HSQ was developed in Shipley CD-26 developer for 8 minutes at 21° C. The field-stitching precision was measured on the monitor wafer by imaging the HSQ grating at the edge of the waveguide. The grating's spatial-phase was compared across each field boundary within four uniform grating devices (80 measurements). Stitching for apodized gratings was not easily measured because of the varying grating depth. The mean stitching error was 0.6 nm and the standard deviation was 2.6 nm. Figure 6.16 shows a sample field boundary along with the stitching

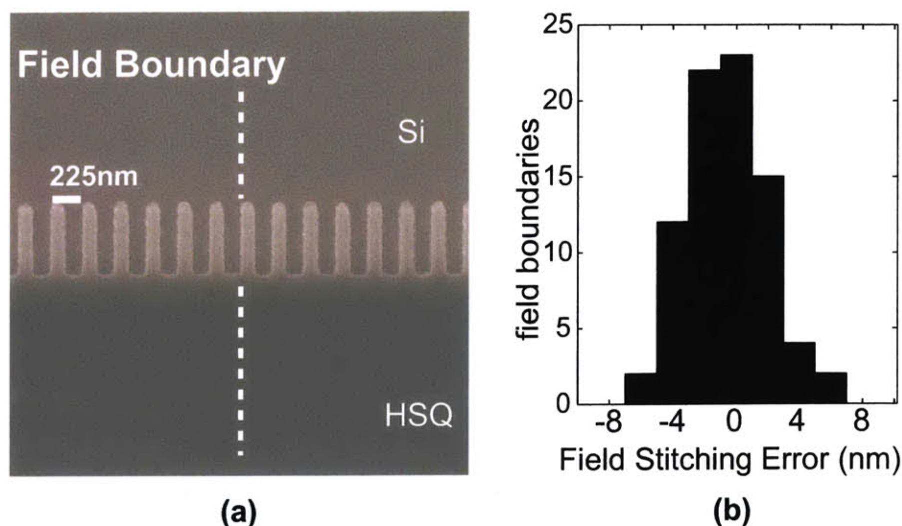

Figure 6.16: Stitching measurements for the sidewall grating pattern. **(a)** Field stitching was measured for uniform gratings at each field boundary. **(b)** Histogram of stitching errors encompassing four uniform-grating devices.

error histogram.

6.3.3 Silicon Etching

The pattern was transferred into the underlying silicon layer using chlorine reactive-ion etching (RIE) in a Perkin/Elmer sputter-etch system modified for RIE. The etch was carried out in four 3:00 minute steps (etch rate $\approx$ 67 nm/min) at a pressure of 10 mTorr, a DC self-bias of 350 V, and a power of 50 W. The sample was removed from the RIE and inspected after each step. This process reduced the slope of the sidewalls compared to samples that were etched continuously. It is hypothesized that exposure of the sample to atmosphere formed a native oxide which was subsequently sputtered off horizontal surfaces while protecting the vertical surfaces.

Figure 6.17 contains scanning-electron micrographs of the apodized sidewall-grating structure after RIE. The pictures were taken at three points along the gratings length.

The grating teeth have an aspect ratio of 7:1 with little sidewall slope. The etch selectivity of Si to e-beam-exposed HSQ was found to be $\approx 9:1$. Unexposed HSQ etches more rapidly under the same conditions. The remaining HSQ etch mask was removed using a 49% hydrofluoric acid solution.

6.3.4 Dicing and Polishing

Before the devices could be tested it was necessary to expose the end faces of the waveguides. This was accomplished by sawing the devices with a Disco DAD-2H/6T die saw. A fine grit (5 μm) blade was used to minimize damage to the end face, but a number of small chips and scratches remained after sawing. To smooth the end surfaces a polishing step was performed. The chip was mounted on a stainless steel block with CrystalBond (Aremco Products Inc., Valley Cottage, NY) and placed in a polishing tripod holder for TEM samples. This holder allows the user to adjust the angle of the chip with respect to the polishing surface in order to polish normal to the surface. Several stages of polishing were conducted with progressively finer grit Al_2O_3 lapping paper on a Buehler ECOMET (Buehler, Ltd. Lake Bluff, Il.) grinding system. The end facets were inspected by SEM to determine the end point. Figure 6.18 shows a typical waveguide facet after polishing.

6.4 SOI Filter Performance

6.4.1 Measurement Apparatus

Transmission measurements of the devices were taken over the range of communications wavelengths near 1550nm. Figure 6.19 contains an overview of the measurement apparatus. Light from a tunable laser (Tunics model, Photonetics Inc.)[5] was coupled into the guide with a lensed glass fiber. The fiber lens has a focal length of approx-

[5]Photonetics has been acquired by NetTest A/S, Brondby, Denmark

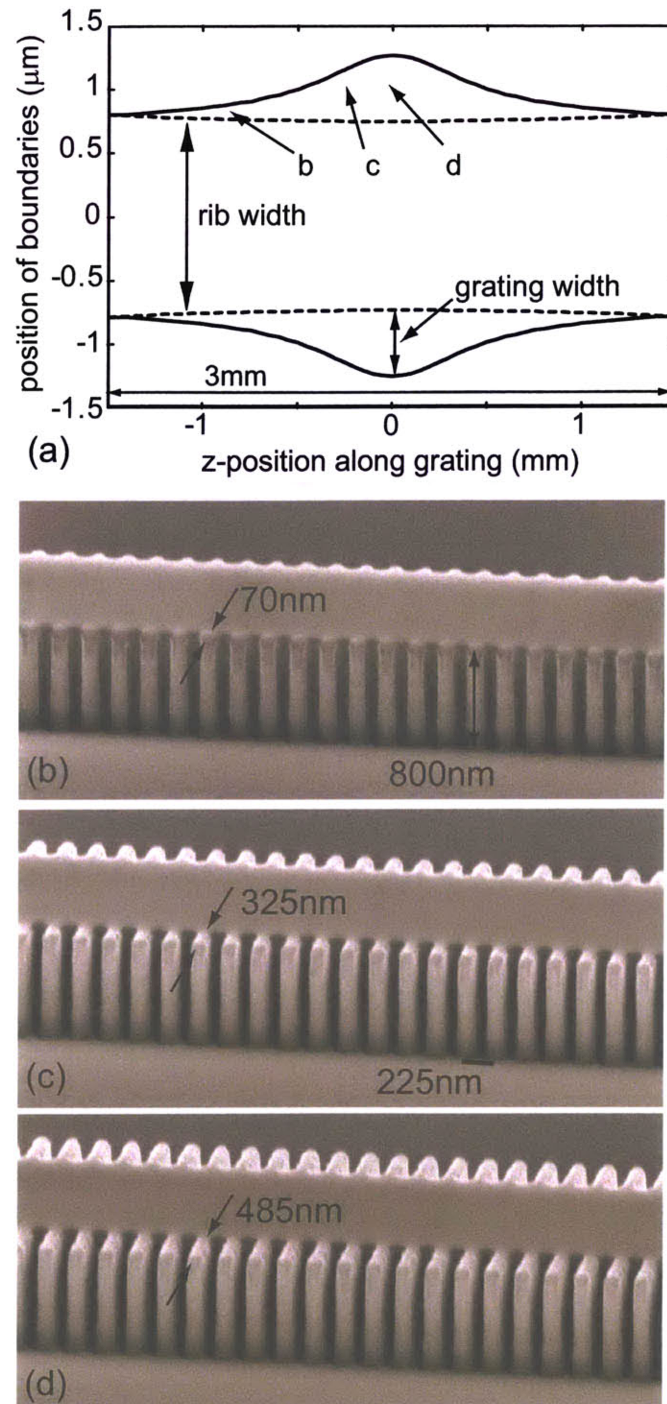

Figure 6.17: Apodized-sidewall gratings: **(a)** plots the waveguide-grating geometry and indicates where the micrographs were acquired, **(b)**, **(c)**, and **(d)** show the sidewall grating structure after reactive-ion etching. The etch aspect ratio was 7:1 and the etch selectivity (Si:HSQ) was 9:1.

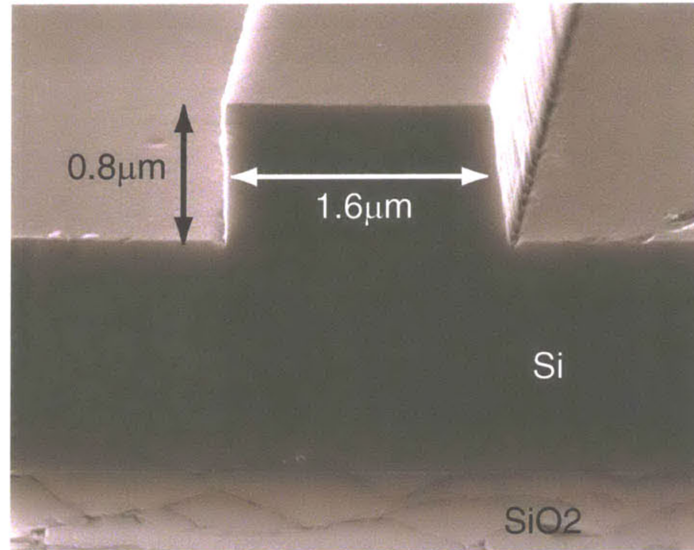

Figure 6.18: SEM of polished SOI waveguide facet.

imately 20μm and a numerical aperture of approximately 0.25. While this provides sufficient coupling to test the device, it far from optimal.

The guides were intentionally angled to intersect the end faces of the device at a 6.7^o. This reduces Fabry-Perot reflections from the facets, while still allowing one to polish the facets normal to the surface. The waveguide angle also dictates that the fiber must be angled 23.6^o with respect to the facet to account for refraction between air and silicon. This relationship is shown in figure 6.19 at the input to the waveguide. The sample was mounted on a stainless steel holder at approximately this angle. The fiber and sample were positioned with separate stages having three and five degrees of freedom respectively. The sample and fiber position were optimized for maximum transmission through the device on the long-wavelength side of the Bragg condition.

After passing through the waveguide-grating structure the light was collected by an objective lens and focused onto a photo-diode detector. A pinhole aperture was placed in front of the detector to minimize detection of stray light. In addition, a variable polarizer facilitated separate measurement of the quasi-TE and TM modes. An infrared-sensitive CCD camera was used to perform the initial alignment of the

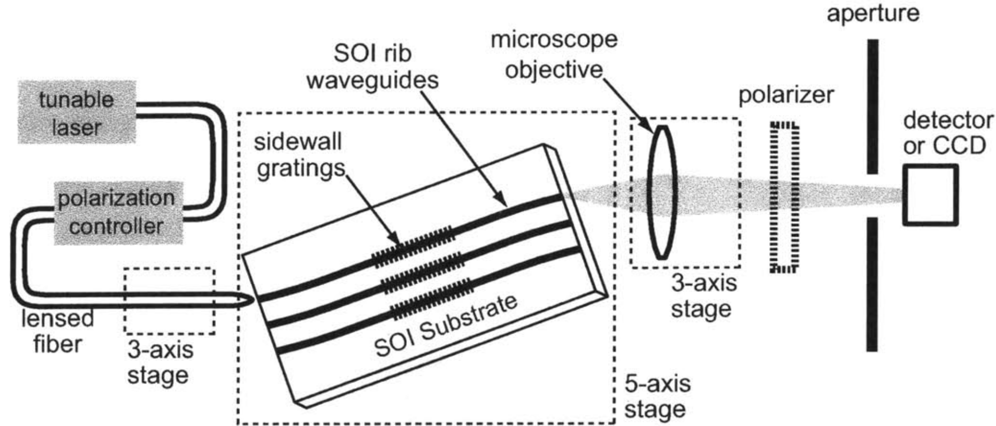

Figure 6.19: Waveguide transmission measurement apparatus.

system and to verify that the objective was aligned to the guide of interest.

6.4.2 Uniform Grating Results

To measure the wavelength dependent transmission of the gratings, the laser source was tuned across the communications c-band from 1530 to 1570nm. To monitor the laser output at each frequency, 10% of the laser power was split off with a fiber coupler. Devices with uniform 1.5-mm long gratings and calculated TE-mode-coupling coefficients of $38cm^{-1}$ were measured first. Figure 6.20 shows the TE- and TM-transmission spectra for such a device.

One will note that the transmission minimum for the TE-device is approximately 1553.5nm, while the design was intended for 1550nm. This discrepancy is almost entirely explained by a calibration error of the e-beam lithography stage in the Raith 150 system. Although the SPLEBL exposure was referenced to the fiducial grating, not the stage, the stage was used to measure the grating initially. Thus the device grating was necessarily specified with respect to the fiducial-grating measurement. There was a relatively large discrepancy between grating period measurements on the two EBL system discussed here, VS2A and the Raith 150. Through consultation with

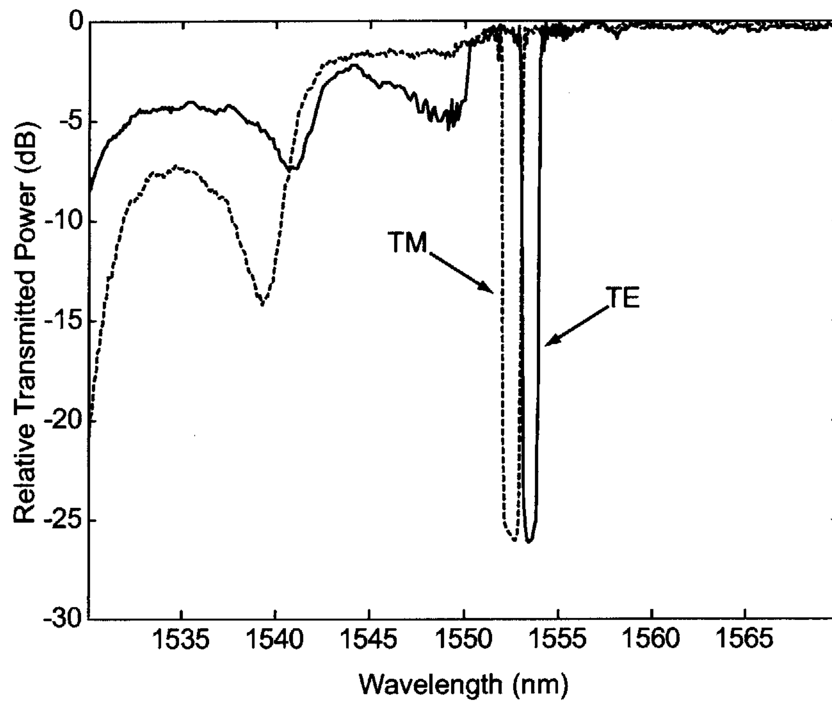

Figure 6.20: Measured c-band TE- and TM-transmission spectra of a waveguide with a 1.5-mm long uniform grating. Although short-wavelength losses are present, there are no discrete transmission minima indicating leaky-mode coupling for the TE transmission spectrum within the c-band.

Raith GMBH it was determined that the stage was miscalibrated by at least factor of 1.00127. Comparison with measurements of masks written on a MEBES system indicate the error is closer to 1.00158.[29] This discrepancy accounts for most of the transmission-minima location error. The residual error can probably be explained by the geometrical differences between the designed structure and the fabricated structure.

Figure 6.21 contains a more detailed plot of the TE- and TM-transmission minima. The difference between the minimum and maximum transmitted power is approximately 25dB. Theoretically, the transmission minimum should be much lower. The -25dB measurement floor does not stem from measurement noise alone. Increasing the input power increases the output power correspondingly, but the transmission minima does not become deeper. Most likely, stray light or coupling between the polarization states after the grating region produces this background. The stray light problem is largely one inherent in the measurement setup, but the coupling between polarization states presents a problem if the two polarizations are to be filtered separately.

Figure 6.21(**a**) indiates that the actual value of κ is 36 cm^{-1} compared to an anticipated value of 38 cm^{-1}. The measured value for the TM-mode, for which the structure was not designed, is 38 cm^{-1} compared to an anticipated value of 43 cm^{-1}. It is clear from SEM micrographs of the structure that the fabricated devices do not exactly match the device design. Three factors contribute to the these errors. The Raith 150 corrects for the slow response of its magnetic deflectors by intentionally lengthening the input scan-voltage sweep by an experimentally determined amount. Unfortunately, this calibration was conducted at a different accelerating voltage than the one used to expose the waveguide patterns. As a result the grating teeth were longer than desired by up to 6%. In addition, proximity effects from electron scattering tend to expose the region between the grating teeth and near the waveguide, making the central waveguide slightly wider than desired by $\approx$ 8%. Taking these variations into account semi-vectorial mode solutions predict κ = 36 cm^{-1} for the

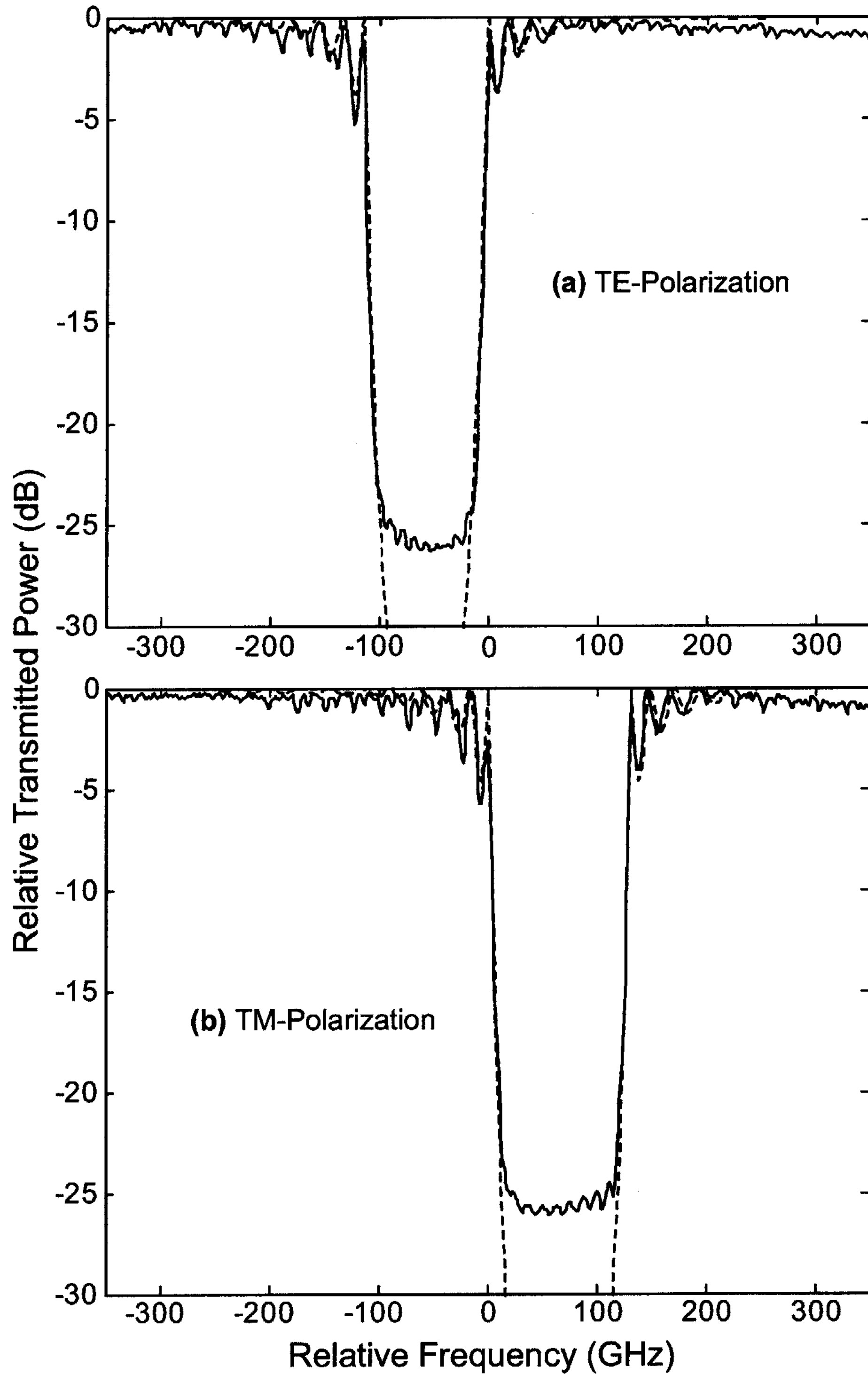

Figure 6.21: Detailed (**a**)TE- and (**b**)TM-transmission spectra of a waveguide with a uniform 1.5-mm long grating. The dashed lines show the calculated transmission for $\kappa = 36\, cm^{-1}$ (TE) and $\kappa = 38\, cm^{-1}$ (TM).

TE-mode which is in very good agreement with the measured spectrum. For the TM-mode the predicted value of κ is 40 cm^{-1}, which is also in better agreement with the measurements.

6.4.3 Apodized Grating Results

Similar measurements were taken of the 3-mm long apodized gratings. Figure 6.22 shows the TE- and TM- transmission minima within the c-band. Figure 6.23 shows a more detailed plot of the TE-response. The uniform gratings shown in figure 6.21(**a**) have sidelobe levels of $\approx$ 5dB; in contrast, the sidelobes in the transmission spectrum of the apodized grating are not discernible. In addition, there are no observable transmission minima at $\pm$607GHz from the central minimum. Such spurious transmission minima would indicate systematic stitching errors at the field boundaries. However, direct measurement of the reflection spectrum would be preferable for determining the grating quality.

For the apodized devices, the transmission spectrum is broadened slightly and does not reach the -25dB measurement floor. This is a direct result of fabrication and design errors described earlier. Because the length of the grating teeth and the central waveguide do not vary in the correct manner, the effective index, n_{eff}, is not constant along the length of the grating. This leads to a symmetric chirp about the center of the grating. That is, the Bragg wavelength increases as one moves toward the center of the grating from either end. Although the device was not designed for TM-operation, the additional structure on the high frequency edge of the TM transmission minimum is also indicative of symmetric chirp. This effect would be apparent in the TM-mode results even in a perfectly fabricated device, because the effective-index can only be uniform along the length of the grating for one polarization state. In addition, rounding of the grating teeth in regions with weak gratings produces a sinusoidal index perturbation rather than a square-wave perturbation. This effect also alters the apodization profile. Despite these shortcoming, this first set of devices

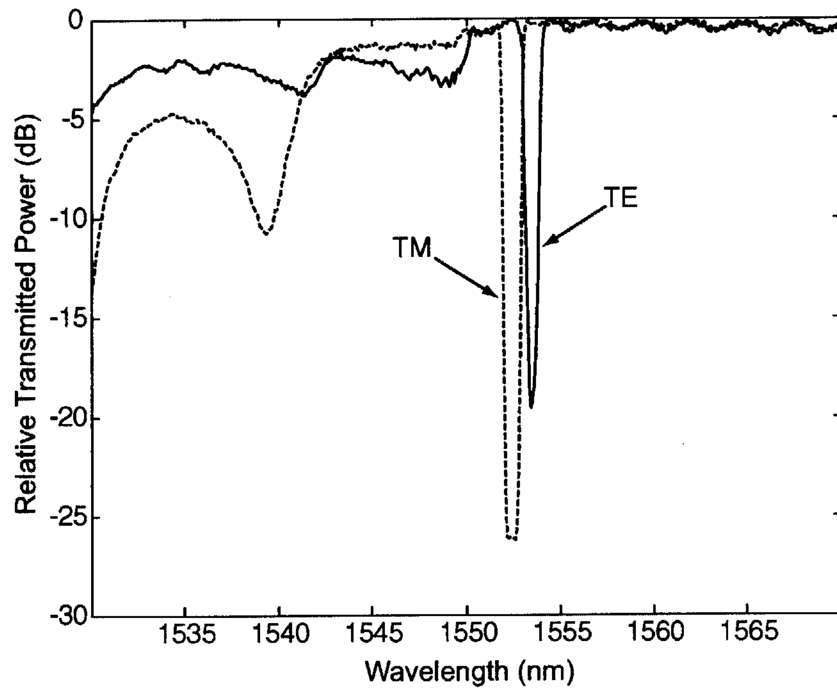

Figure 6.22: Measured c-band TE- and TM- transmission spectra of a waveguide with a 3.0-mm long apodized grating.

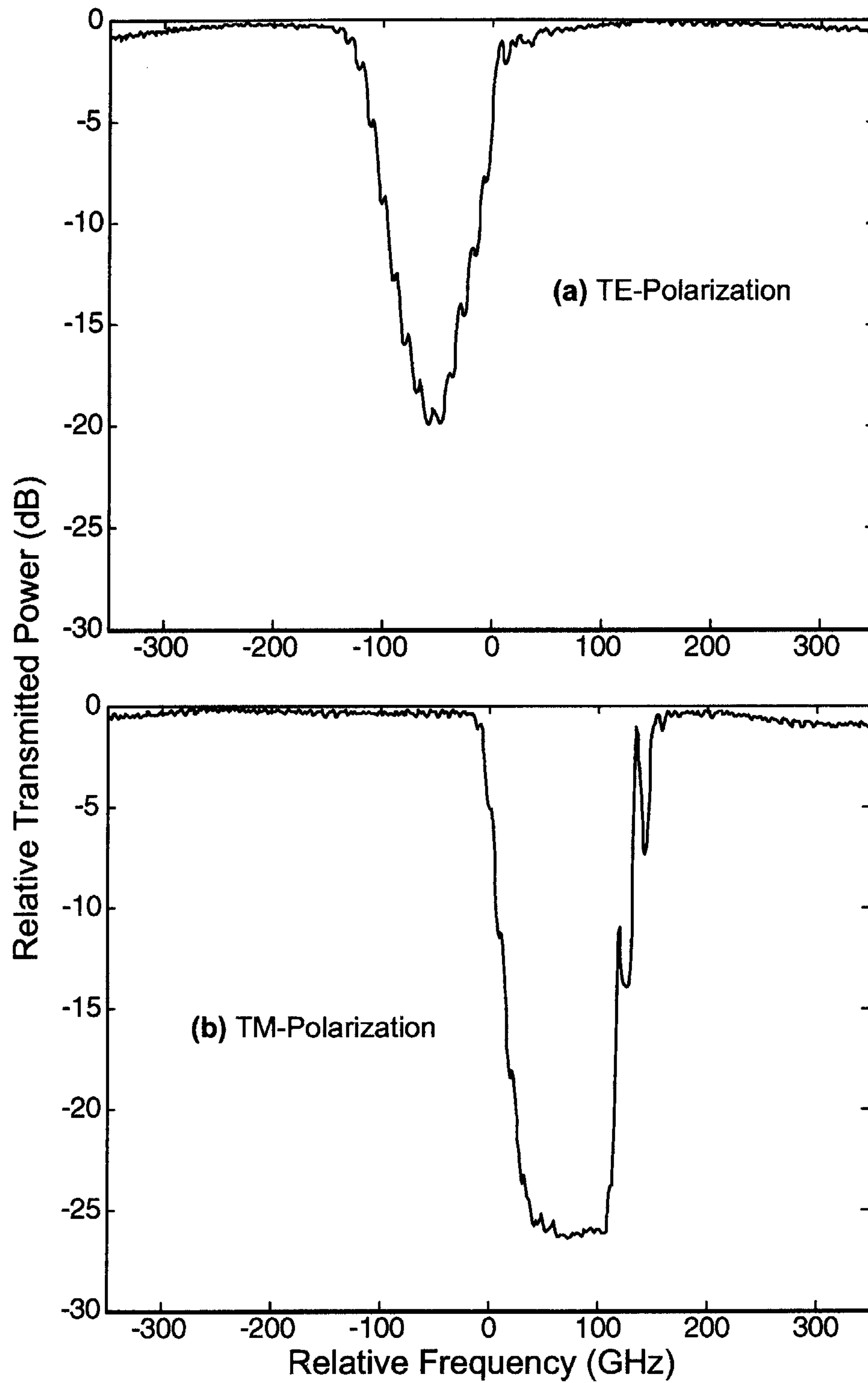

Figure 6.23: Detailed (a)TE- and (b)TM-transmission spectrum of a waveguide with apodized, 3.0-mm long sidewall gratings. The devices were designed for TE-mode operation only. Note the reduction of sidelobe levels compared to uniform devices.

illustrates the effectiveness of sidewall gratings for fabricating apodized filters.

Chapter 7

Conclusion

Spatial-phase locking fundamentally improves the pattern-placement process in e-beam lithography. Closed-loop feedback provides unmatched placement precision while reducing the need for complex and costly measures to stabilize the system. The segmented-grid and sparse-sampling modes provide straightforward solutions when one can sacrifice substrate area and throughput, while continuous feedback yields the best pattern-placement precision and requires no substrate area or overhead time.

Transferring segmented grid SPLEBL to the Raith 150 system improved the placement-precision of this technique, but revealed several pattern-dependent placement issues. Careful compensation for deflection-velocity dependent errors allowed field stitching precision of $\sigma = 2.6nm$. The segmented grid mode also proved useful for integrated optical device fabrication. These devices required the development of a fiducial grid, resist processes, and reactive ion-etching compatible with direct-write SPLEBL.

Sparse-sampling occupies an intermediate domain between the segmented-grid mode and continuous phase-locking. It uses a global grid and sacrifices no substrate area but remains a "look-then-write" approach. Techniques were developed to extract field calibration parameters from grid moiré patterns; thus, the system could sample a fine-period grid with a sparse array of points. The sparse-sampling mode

provided the first pattern exposures using 2D spatial-phase locking and the first implementation of a scintillating fiducial grid. Scintillating grids offer the advantages of UV quenching and reduced electron scattering, but, despite the efforts of several researchers, no fluorescent grid was found that provided adequate signal-to-noise ratio for fine-periods. The e-beam induced scintillator damage also reduced SNR for dense sampling, and made repeated observations of the same grid area impossible.

Real-time spatial-phase locking corrects x- and y-beam shift while raster scanning over a rotated fiducial grid. To implement this continuous feedback approach we developed two-frequency spatial-phase locking, implemented raster-scan pattern generation for the Raith 150 system, and developed hardware and software to perform the feedback corrections. To minimize deterministic deflection errors we devised methods to calculate higher-order distortion corrections by scanning the fiducial grid. Real-time SPLEBL yielded field-stitching errors with $\sigma \leq 1.3$nm and comparable global pattern-placement with respect to the grid.

While the initial performance of real-time SPLEBL is impressive, many opportunities for improvement remain. In the short term, boustrophedonic scanning and more sophisticated distortion correction will expand the useful field size and improve throughput. Optimizing the feedback loop filter may offer additional improvements in placement precision, while enhancements to the spatial-phase locking software will make it accessible to users with less extensive e-beam lithography experience. Longer term, implementing dose-modulation is essential for flexible patterning, and the recent incorporation of dose-modulation in commercial systems is encouraging.

Fiducial grids with higher SNRs and finer periods will further improve pattern-placement and will allow spatial-phase locking with lower doses and more sensitive resists. High secondary-electron yield materials and voltage contrast hold promise in this area. Initial mastering and faithful replication of highly accurate grids remain challenging, but the combination of scanning-beam-interference lithography and phase-mask replication offers a potential solution. Finally, simplified grid pattern-

ing, not involving resist-based lithography, deposition, or etching, would increase SPLEBL's appeal to mask manufacturers. Zhang is currently pursuing several ideas along this line.[28]

While integrated-circuit mask production remains the largest future market for SPLEBL, many integrated-optical components currently require improved placement accuracy. This thesis presents the design, fabrication, and testing of Bragg-grating optical filters based on silicon-on-insulator waveguides. SOI provides an interesting and relatively unexplored material system for communications wavelengths, and serves as an excellent platform on which to demonstrate the sidewall-grating concept.

The sidewall grating process produces gratings and waveguides in a single lithographic step and eliminates the need for precise registration between two layers. Perhaps more importantly, the sidewall approach allows the grating strength to be controlled lithographically. This is particularly important for devices with an apodized filter response such as those described in chapter 6. While the measured transmission response for this first set of devices is not ideal, the effects of apodization and the precise stitching of SPLEBL were demonstrated. In the future, sidewall gratings should provide a powerful design and fabrication technique for filtering and laser feedback applications.

Now that several planar fabrication techniques offer near-nanometer resolution, continuing efforts will be required to ensure nano-accuracy. This is particularly relevant as devices move from the laboratory to manufacturing where product uniformity and yield are essential. Not surprisingly, closed-loop control and high-quality standards, two fundamental engineering concepts, will play a key role in maintaining accuracy at the nano-scale. The author hopes that spatial-phase locked e-beam lithography provides a fabrication solution for future electronic and optical devices, and provides a foundation for high-precision patterning in other fields that harness planar processing.

Appendix A

Hydrogen Silsesquioxane: a Negative EBL Resist

Hydrogen silsesquioxane (HSQ) is a dielectric material with many of the properties of SiO_2. Unlike SiO_2, it can be spin-cast from certain organic solvents, most often Methyl-iso butyl Ketone (MIBK). HSQ consists of $Si_8O_{12}H_8$ "cage" structures as shown in figure A.1. When thermally cured these cage structures break apart and form a longer-range network structure based on Si-O-Si bonding.[79] Some disagreement remains concerning the exact reaction pathway and its by-products.

HSQ also serves as a high-resolution negative resist where network formation is induced by electron exposure.[77] Unexposed HSQ is soluble in basic solutions such as potassium hydroxide and tetra-methyl ammonium hydroxide (TMAH), while the network structure of exposed HSQ is not. Namatsu et al. demonstrated 7-nm isolated lines with 10:1 aspect ratios in 100 keV exposures.[80] Dense 20-nm lines and spaces were realized by vanDelft et al., also using a 100 keV e-beam.[78] HSQ exhibits adequate sensitivity for research applications, acceptable contrast, and etch selectivity to many materials.

To characterize HSQ's performance as a negative e-beam resist we measured its development rate as a function of areal dose. A 520-nm-thick layer of HSQ (FOx-

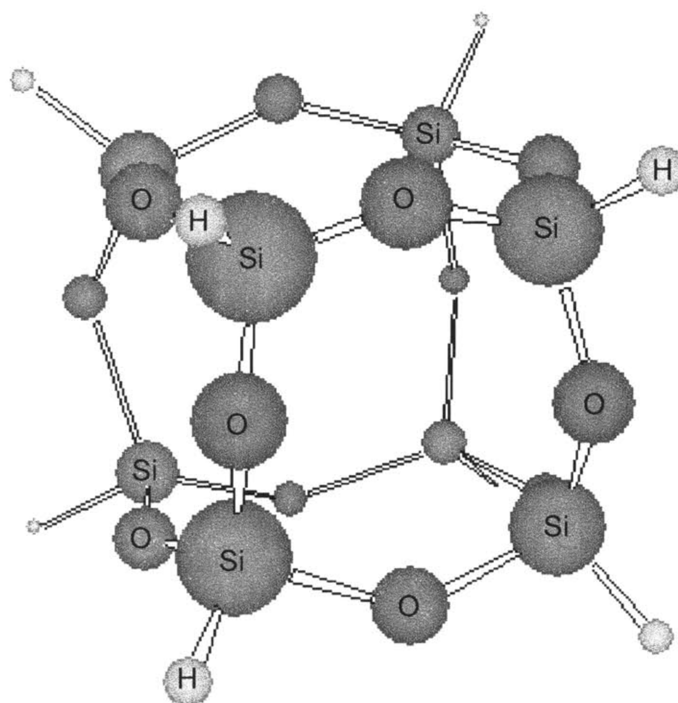

Figure A.1: Molecular structure of HSQ "cage" before e-beam exposure or thermal curing.

16 from Dow-Corning) was spun onto silicon wafers. The HSQ was prebaked for 30 minutes at 150° C and 30 minutes at 220° C in a convection oven. Rectangles, $1\mu m \times 20\mu m$, were exposed using a 30 keV e-beam with doses ranging from 60 μC/cm^2 to 800 μC/cm^2. The rectangles were spaced by 50 μm which is beyond the range of backscattered electrons at 30kV. We developed the samples at 21.0° C in Shipley CD-26[1] for 15 minutes.

To characterize the resist with only one development time it is necessary to assume uniform energy deposition as a function of depth. This assumption is valid for weakly scattering resists exposed at high accelerating voltages. HSQ has somewhat higher Z-density than most organic resists, but the uniform energy deposition assumption

[1]Shipley Company, LLC. Marlborough, MA. CD-26 is a general purpose tetra-methyl ammonium hydroxide (TMAH) based developer with additional surfactants.

seems reliable based on observed development rates.

After development, the remaining resist height for each box was measured using an atomic force microscope. The development rate is given by $(h_0 - h)/\tau$ where h_0 is the initial resist thickness, h is the remaining resist thickness, and τ is the development time. The development rate of most resists is well modeled by the function

$$R = AD^B \tag{A.1}$$

where R is the development rate, D is the dose, and A and B are fitting parameters that depend on the resist and developer. In this case we consider areal dose, as opposed to linear or volumetric dose, in units of $\mu C/cm^2$. Figure A.2 plots the experimental development rate versus dose on a logarithmic scale. All boxes with doses below 150 $\mu C/cm^2$ developed away completely. The solid line plots the least squares fit of equation A.1 to the data. It is also useful to plot the normalized resist thickness versus dose. This sensitivity curve is shown in figure A.3. The required dose to maintain 80% resist thickness is about 240 $\mu C/cm^2$ at 30kV for a 15 minute development time.

To further characterize HSQ as a high-resolution resist we exposed isolated lines and gratings. A dilution of 3 parts MiBK to 2 parts FOx-16 was prepared and spun onto silicon wafers to obtain a 125-nm-thick HSQ layer. For these experiments the samples were baked on vacuum hotplates for 120 seconds at 150° C and 120 seconds at 220° C. After exposure with a 30 keV e-beam, the HSQ was developed for 6:00 minutes in CD-26 at 21.0 ° C. Figure A.4 shows the resulting isolated lines. The 50-nm wide line was coded as a 50-nm wide rectangle and exposed with a 1320 $\mu C/cm^2$ dose. The 22-nm wide line was written with a single pass of the e-beam and a linear dose of 2.25 nC/cm. Figure A.5 shows a 100-nm-period grating that was coded as 50 nm lines and spaces and exposed at 400 $\mu C/cm^2$.

HSQ has proven somewhat unstable with time, both in solution and on the

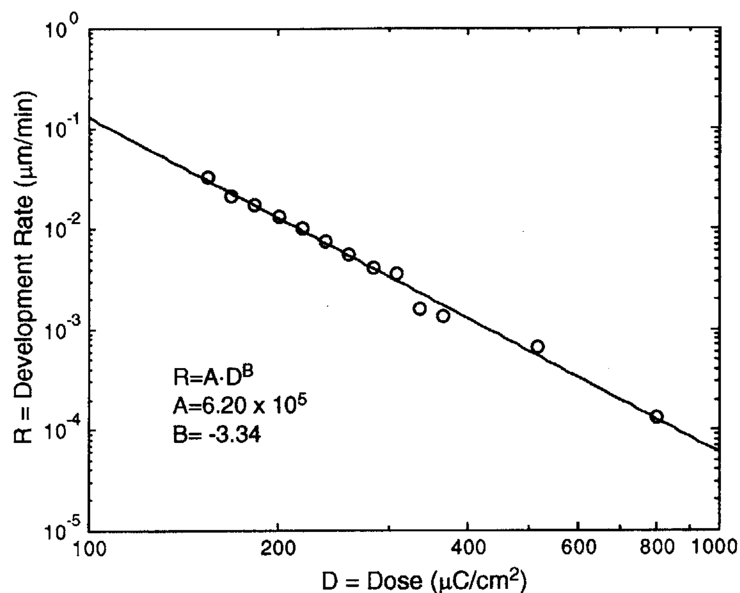

Figure A.2: Development rate versus dose for HSQ exposed at 30kV. Least squares fitting to equation A.1 yields $A = 6.20 \times 10^5$ and $B = -3.34$.

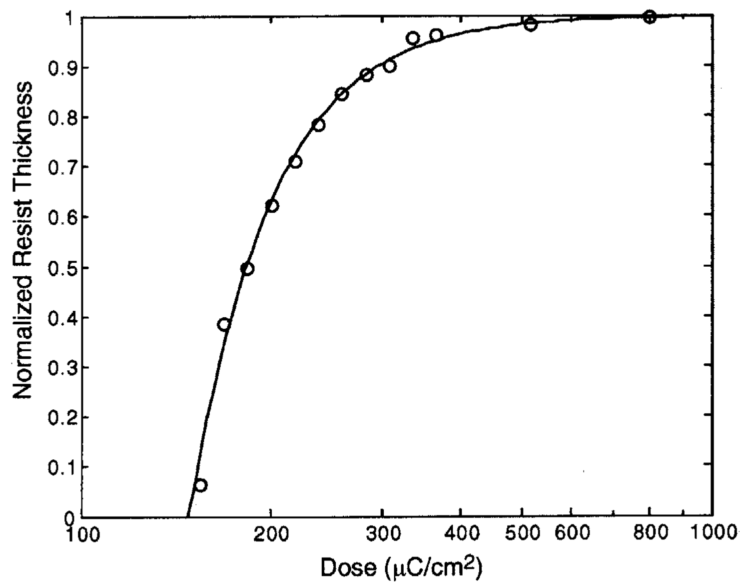

Figure A.3: Normalized thickness versus dose for HSQ exposed at 30kV. The solid line represents the least squares fit from equation A.1.

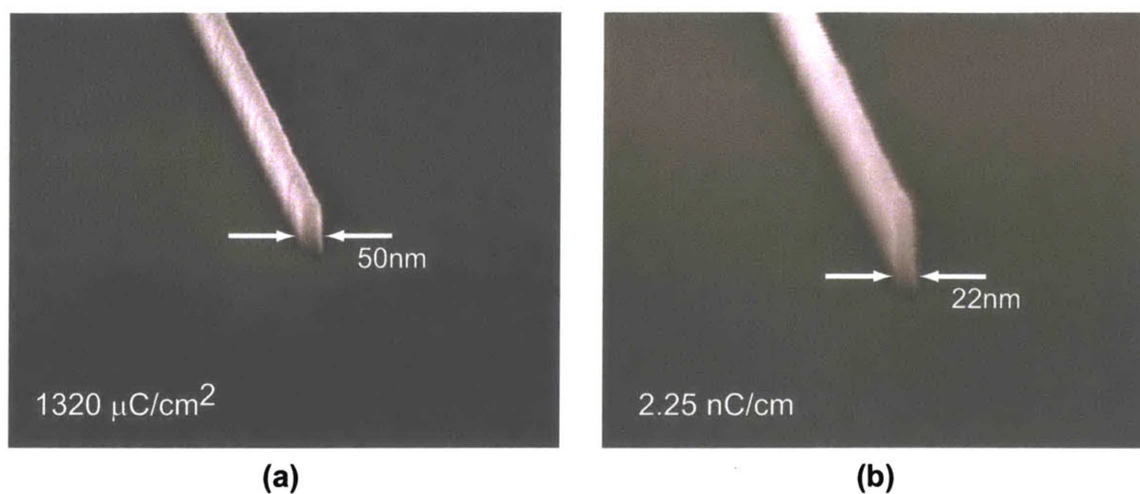

Figure A.4: Isolated lines patterned in HSQ with a 30 keV e-beam. **(a)** 50-nm wide line from a 50-nm wide coded rectangle (dose = 1320 μC/cm^2). **(b)** 22-nm wide line written with a single pass of the electron beam (linear dose = 2.25 nC/cm).

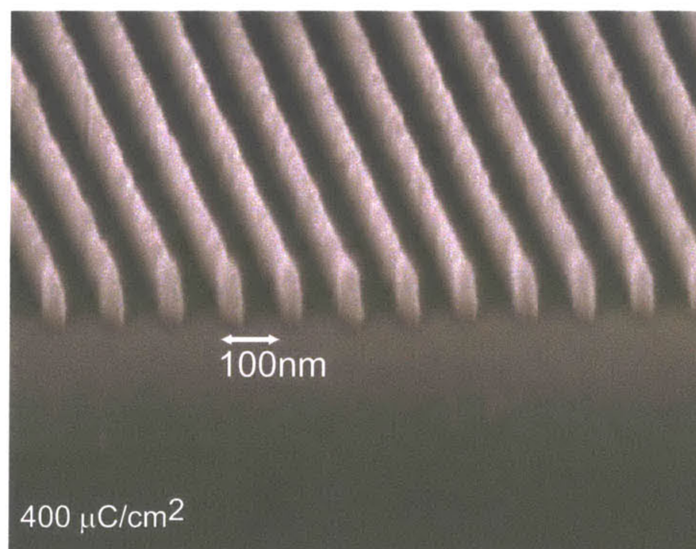

Figure A.5: 100-nm period grating patterned in HSQ. The coded design consisted of 50-nm lines and spaces, and the dose was 400 μC/cm^2.

wafer.[81] As a result, one should avoid delays between spin coating, exposure, and development. It is also important that the HSQ solution not come in contact with glass; otherwise, the solution will convert into a gel-like substance in a matter of minutes. Nevertheless, HSQ provides a high-resolution negative e-beam resist with the ease of processing, if not the stability, of PMMA. Unlike PMMA, HSQ is stable under SEM inspection and can provide a hard-mask layer for reactive-ion etching. As such, it provides a valuable addition to the range of materials available for e-beam patterning.

Bibliography

[1] G. Cartwright, G. Reynolds, C. Baylis, A. Pearce, C. Dix, and N. Ogilvie, "Electron beam recording of optical disc," *Journal of Magnetism and Magnetic Materials*, vol. 249, no. 3, pp. 442–446, 2002.

[2] M. Isaacson and A. Murray, "Insitu vaporization of very low-molecular weight resists using 1-2 nm diameter electron-beams," *J. Vac. Sci. Technol.*, vol. 19, no. 4, pp. 1117–1120, 1981.

[3] J. Stroscio and D. Eigler, "Atomic and molecular manipulation with the scanning tunneling microscope," *Science*, vol. 254, no. 5036, pp. 1319–1326, 1991.

[4] "International technology roadmap for semiconductors," 2002. http://public.itrs.net.

[5] S. A. Rishton, B. Pezeshki, S. Zou, G. Yoffe, and W. Henschel, "Tunable distributed-feedback laser gratings for telecom applications, manufactured by electron-beam lithography," *J. Vac. Sci. Technol. B*, vol. 20, no. 6, pp. 2749–2752, 2002.

[6] J. G. Hartley, T. R. Groves, H. I. Smith, M. K. Mondol, J. G. Goodberlet, M. L. Schattenburg, J. Ferrera, and A. Bernshteyn, "Spatial-phase locking with shaped-beam lithography," *Review of Scientific Instruments*, vol. 74, no. 3, pp. 1377–1379, 2003.

[7] P. Sen, D. S. Pickard, J. E. Schneider, M. A. McCord, R. F. Pease, A. W. Baum, and K. A. Costello, "Lifetime and reliability results for a negative electron affinity photocathode in a demountable vacuum system," *J. Vac. Sci. Technol. B*, vol. 16, pp. 3380–3384, 1998.

[8] F. Abboud, K. Baik, V. Chakarian, D. Cole, J. Daniel, R. Dean, M. Gesley, M. Lu, R. Naber, T. Newman, F. Raymond, D. Trost, M. Wiltse, and W. DeVore, "100nm opc mask patterning using raster-scan, 50kv pattern generation technology," *21st Annual BACUS Symposium on Photomask Technology*, vol. 4562, 2001.

[9] "Agilent high performance laser interferometer positioning for VMEbus systems: Product overview," 2001. http://cp.literature.agilent.com/litweb/pdf/5965-1569E.pdf.

[10] A. Muray, M. Isaacson, and I. Adesida, "AlF3 - a new very high-resolution electron-beam resist," *Appl. Phys. Lett.*, vol. 45, pp. 589–591, 1984.

[11] "boustrophedon, adv. and a. (n.)" Oxford English Dictionary. Ed. J. A. Simpson and E. S. C. Weiner. 2nd ed. Oxford: Clarendon Press, 1989. OED Online. Oxford University Press. 4 Mar. 2003. http://dictionary.oed.com/cgi/entry/00026003.

[12] D. R. Herriott, R. J. Collier, D. S. Alles, and J. W. Stafford, "EBES - practical electron lithographic system," *IEEE Trans. Electron Devices*, vol. ED22, pp. 385–392, 1975.

[13] "International technology roadmap for semiconductors," 2000. http://public.itrs.net.

[14] "MEBES eXara," 2003. http://www.appliedmaterials.com/products/assets/mask products/about mask pattern generation technology.pdf.

[15] "MEBES 5500," 2003. http://www.etec.com/products/assets/mask products/mebes 5500 printable datasheet.pdf.

[16] "JBX-9000MV Electron Beam Lithography System," 2003. http://www.jeol.com/semi/eb/jbx9000.html.

[17] "Vector-scan e-beam tool: EBM-4000," 2002. http://www.nuflare.co.jp/english/01 ebm4000/index.html.

[18] S. Tsuboi, Y. Tanaka, T. Iwamoto, H. Sumitani, and Y. Nakayama, "Recent progress in 1x x-ray mask technology: Feasibility study using ASET-NIST format TaXN x-ray masks with 100 nm rule 4 Gbit dynamic random access memory test patterns," *J. Vac. Sci. Technol. B*, vol. 19, no. 6, pp. 2416–2422, 2001.

[19] J. C. Maxwell, "Does the progress of physical science tend to give any advantage to the opinion of necessity (or determinism) over that of the contingency of events and the freedom of the will?," *Contribution to Eranus Society - Cambridge*, 1873.

[20] P. Konkola, *Scanning Beam Interference Lithography*. PhD thesis, Massachusetts Institute of Technology, 2003.

[21] T. A. Savas, M. L. Schattenburg, J. M. Carter, and H. I. Smith, "Large-area achromatic interferometric lithography for 100 nm period gratings and grids," *J. Vac. Sci. Technol. B*, vol. 14, pp. 4167–4170, 1996.

[22] M. Durkin, M. Ibsen, M. Cole, and R. Laming, "1m long continuously-written fibre bragg gratings for combined second- and third-order dispersion compensation," *Electronics Letters*, vol. 33, no. 22, pp. 1891–1893, 1997.

[23] J. Ferrera, *Nanometer-Scale Placement in Electron-Beam Lithography.* PhD thesis, Massachusetts Institute of Technology, June 2000.

[24] J. Ferrera, M. L. Schattenburg, and H. I. Smith, "Analysis of distortion in interferometric lithography," *J. Vac. Sci. Technol. B*, vol. 14, pp. 4009–4013, 1996.

[25] D. C. Joy, "A database of electron-solid interactions," 2001. http://web.utk.edu/srcutk/htm/interact.htm.

[26] J. Ferrera, V. Boegli, E. H. Anderson, D. P. Kern, and H. I. Smith, "Spatial-phase-locked electron-beam lithography: Initial test results," *J. Vac. Sci. Technol. B*, vol. 11, no. 6, pp. 2342–2345, 1993.

[27] O. C. Wells, *Scanning electron microscopy.* New York: McGraw-Hill, 1974.

[28] F. Zhang. PhD thesis, Massachusetts Institute of Technology, 2004. in preparation.

[29] J. G. Goodberlet, 2002. Private Communication.

[30] J. Goodberlet, J. Carter, and H. I. Smith, "Scintillating global-fiducial grid for electron-beam lithography," *J. Vac. Sci. Technol. B*, vol. 16, no. 6, pp. 3672–3675, 1998.

[31] M. A. Finlayson, "Scintillator for spatial-phase-locked e-beam lithography," Master's thesis, Massachusetts Institute of Technology, June 2001.

[32] R. J. Hawryluk, "Exposure and development models used in electron beam lithography," *J. Vac. Sci. Technol.*, vol. 19, no. 1, pp. 1–17, 1981.

[33] S. A. Rishton and D. P. Kern, "Point exposure distribution measurements for proximity correction in electron beam lithography on a sub-100 nm scale," *J. Vac. Sci. Technol. B*, vol. 5, no. 1, pp. 135–141, 1981.

[34] E. Anderson, D. Olynick, W. Chao, B. Harteneck, and E. Veklerov, "Influence of sub-100 nm scattering on high-energy electron beam lithography," *J. Vac. Sci. Technol. B*, vol. 19, no. 6, pp. 2504–2507, 2001.

[35] S. M. Kay, *Modern spectral estimation: theory and application.* Englewood Cliffs, N.J.: Prentice Hall, 1988.

[36] A. S. Willsky, G. W. Wornell, and J. H. Shapiro, *Stochastic Processes Detection and Estimation.* Cambridge, Ma.: Massachusetts Institute of Technology, 1998.

[37] H. I. Smith, S. D. Hector, M. K. Schattenburg, and E. H. Anderson, "A new approach to high fidelity e-beam and ion-beam lithography based on an *in situ* global-fiducial grid," *J. Vac. Sci. Technol. B*, vol. 9, no. 6, pp. 2992–2995, 1991.

[38] E. H. Anderson, V. Boegli, M. L. Schattenburg, D. Kern, and H. I. Smith, "Metrology of electron-beam lithography systems using holographically produced reference samples," *J. Vac. Sci. Technol. B*, vol. 9, pp. 3606–3611, 1991.

[39] H. I. Smith, S. R. Chinn, and P. D. Degraff, "Application of moire techniques in scanning electron-beam lithography and microscopy," *J. Vac. Sci. Technol.*, vol. 12, pp. 1262–1265, 1975.

[40] M. Mondol, 2002. Private communication.

[41] J. Goodberlet, J. Ferrera, and H. I. Smith, "Spatial-phase-locked electron-beam lithography with a delay-locked loop," *J. Vac. Sci. Technol. B*, vol. 15, no. 6, pp. 2293–2297, 1997.

[42] M. Gesley, D. Colby, F. Raymond, D. McClure, and F. Abboud, "Electrodynamic of fast beam blankers," *J. Vac. Sci. Technol. B*, vol. 11, no. 6, pp. 2378–2385, 1993.

[43] F. Abboud, K.-h. Baik, V. Chakarian, D. Cole, J. Daniel, R. Dean, M. Gesley, M. Lu, R. Naber, T. Newman, F. Raymond, D. Trost, M. Wiltse, and W. DeVore, "100nm opc mask patterning using raster-scan, 50kV pattern generation technology," *Proceedings-of-the-SPIE-The-International-Society-for-Optical-Engineering*, vol. 4562, pp. 1–8, 2002.

[44] J. Goodberlet, S. Silverman, J. Ferrera, M. Mondol, M. Schattenburg, and H. I. Smith, "A one-dimensional demonstration of spatial-phase-locked electron-beam lithography," *Microelectronic Engineering*, vol. 35, pp. 473–476, 1997.

[45] J. G. Goodberlet, J. T. Hastings, and H. I. Smith, "Performance of the raith 150 e-beam lithography system," *J. Vac. Sci. Technol. B*, vol. 19, no. 6, pp. 2499–2503, 2001.

[46] M. S. Stern, P. C. Kendall, and P. W. A. McIlroy, "Analysis of the spectral index method for vector modes of rib wave-guides," *IEE Proc-J Optoelectronics*, vol. 137, pp. 21–26, 1990.

[47] T. E. Murphy, *Design, Fabrication and Measurement of Integrate Bragg Grating Optical Filters*. PhD thesis, Massachusetts Institute of Technology, 2001.

[48] "MATLAB function reference: eigs," 2003. http://www.mathworks.com/access/helpdesk_r12p1/help/techdoc/ref/eigs.shtml.

[49] L. A. Coldren and S. W. Corzine, *Diode lasers and photonic integrated circuits.* New York: Wiley, 1995.

[50] D. G. Hall, "A comment on the coupled-mode equations used in guided-wave optics," *Optics Communications*, vol. 82, pp. 453–455, 1991.

[51] T. Erdogan, "Fiber grating spectra," *Journal of Lightwave Technology*, vol. 15, pp. 1277–1294, Aug 1997.

[52] M. H. Lim, T. E. Murphy, J. Ferrera, J. N. Damask, and H. I. Smith, "Fabrication techniques for grating-based optical devices," *J. Vac. Sci. Technol. B*, vol. 17, no. 6, pp. 3208–3211, 1999.

[53] J. C. Huang, "Fabrication of a planar optical add/drop channel filter in silicon oxynitride," Master's thesis, Massachusetts Institute of Technology, May 2002.

[54] D. Wiesmann, C. David, R. Germann, D. Erni, and G. L. Bona, "Apodized surface-corrugated gratings with varying duty cycles," *IEEE Photon. Technol. Lett.*, vol. 12, no. 6, pp. 639 – 641, 2000.

[55] V. V. Wong, J. Ferrera, J. N. Damask, T. E. Murphy, H. I. Smith, and H. A. Haus, "Distributed bragg grating integrated-optical filters: Synthesis and fabrication," *J. Vac. Sci. Technol. B*, vol. 13, pp. 2859 – 2864, 1995.

[56] A. Cutolo, M. Iodice, P. Spirito, and L. Zeni, "Silicon electro-optic modulator based on a three terminal device integrated in a low-loss single-mode SOI waveguide," *Journal of Lightwave Technology*, vol. 15, pp. 505–518, 1997.

[57] U. Fischer, T. Zinke, B. Schuppert, and K. Petermann, "Singlemode optical switches based on SOI wave-guides with large cross-section," *Electron. Lett.*, vol. 30, pp. 406–408, 1994.

[58] T. E. Murphy, J. T. Hastings, and H. I. Smith, "Fabrication and characterization of narrow-band Bragg reflection filters in silicon-on-insulator ridge waveguides," *Journal of Lightwave Technology*, vol. 19, pp. 1938–1942, 2001.

[59] P. Heimala, T. Aalto, S. Yliniemi, J. Simonen, M. Kuittinen, J. Turunen, and M. Leppihalme, "Fabrication of bragg grating structures in silicon," *Phys. Scr.*, vol. T101, pp. 92–95, 2002.

[60] B. E. Little, J. S. Foresi, G. Steinmeyer, E. R. Thoen, S. T. Chu, H. A. Haus, E. P. Ippen, L. C. Kimerling, and W. Greene, "Ultra-compact Si-SiO_2 microring resonator optical channel dropping filters," *IEEE Photonics Technol. Lett.*, vol. 10, pp. 549–551, 1998.